Politecnico di Torino

Laurea Magistrale in Ingegneria Biomedica
A.a. 2022/2023

Neuro-biomechanics of Chiari malformation:

Modelling CSF flow and soft tissues of the central nervous system in the normal setting and Chiari 1 malformation

Promoter:
Prof. dr. ir. Patrick Segers (Ugent)
Prof. dr. ir. Nele Famay (Ku Leuven)
Prof. dr. ir. Umberto Morbiducci

Supervisors:
Ir. Sarah Vandenbulcke (Ugent)

Candidate:
Samuele Baracchi

A project in collaboration with Ghent University

Declaration of Authorship

I, Baracchi Samuele, that the thesis title ''Neuro biomechanics of Chiari malformation: Modelling CSF flow and soft tissues of the central nervous system in the normal setting and the Chiari 1 malformation'' and the work presented in it are my own. I confirm that:

- This work was done wholly or mainly while in candidature for a Master of Science degree at this University.
- Where any part of this thesis has previously been submitted for a degree or any other qualification at this University or any other institution, this has been clearly stated.
- Where I have consulted the published work of others, this is always clearly attributed.
- Where I have quoted from the work of others, the source is always given. With the exception of such quotations, this thesis is entirely my own work.
- I have acknowledged all main sources of help.
- Where the thesis is based on work done by myself jointly with others, I have made clear exactly what was done by others and what I have contributed myself.

Signed: _____

Date: 27/08/2023

Acknowledgements:

I wish to express my sincere gratitude to my supervisor Prof. Dr. Ir. Umberto Morbiducci and Prof. Dr. Ir. Patrick Segers, whose guidance, support, and generosity in sharing their expertise have been invaluable throughout my journey.

Additionally, I am deeply grateful to my counsellor, Ir. Sarah Vandenbulcke, whose insightful counsel has illuminated my path and provided me with essential guidance.

The privilege of collaborating with these them has not only enhanced my professional acumen but has also fostered my personal growth.

I extend my sincere thanks to my parents for granted me to study and experience this ERASMUS period. A big thanks girlfriend, Marta, whose support has been a constant source of strength, even across distances, especially during challenging times.

Lastly, I extend my gratitude to all my friend of PoliTo, VUB, and Ugent.

Baracchi Samuele.

Abstract

The cerebrospinal fluid (CSF) surrounds and protects the brain and spinal cord offering a cushion against shock and aiding in maintaining physiological balance. Understanding CSF dynamics is crucial for insights into neurological disorders like Chiari 1 Malformation (CM1) and hydrocephalus. CM1 involves the downward displacement of brain tissue through the skull opening, which obstructs the CSF flow. Theories suggest that this altered CSF distribution due to CM1 might contribute to related disorders like syringomyelia, where fluid accumulates within the spinal cord and which has been associated with severe motor and sensory symptoms. However, the source of syringomyelia remains debated. This thesis aims to investigate the effect of an obstruction as present in CMI using both a Computational Fluid Dynamics (CFD) and a poroelastic Fluid Structure Interaction (FSI) approach. The artificial 3D herniation has the advantage to be the same in the different simulation leading to not impact of the difference in person specific geometry between healthy and with obstruction which can lead to a bigger impact that the obstruction itself.

First, the 3D circulation of CSF is investigated in a CFD model of the cranial and upper spinal CSF. Following this, the effects of a 3D idealized volume that mimics CM1-related obstruction within a section of the SAS are investigated at varying levels of obstruction: 40%, 60% and 100%. First, in CFD simulations, the CSF space is considered rigid without interaction with the spinal cord. Subsequently, the spinal cord is modelled as a poroelastic material which can mechanically interacts and allow fluid exchange with the CSF in the spinal SAS.

The simulation outcomes indicate that obstructed CSF flow within the cervical spinal canal leads to increased pressure gradients and velocities. The heightened velocities are predominantly observed within the obstruction region. Particularly the substantial obstruction appears to alter the spinal cord's deformation behaviours and seems to enhance fluid exchange between the spinal SAS and the spinal cord. However, the precise mechanisms driving this relationship remain unclear, warranting further investigation. The study's results reveal that implementing the FSI approach did not significantly improve the understanding of CSF flow in the spinal SAS. However, it did offer extra insights into fluid exchange and stresses in the spinal cord.

In conclusion, this study has provided enhanced insights into the implications of an artificial three-dimensional obstruction using the CFD and the FSI. The findings might facilitate the selection of the most suitable approach for subsequent simulations.

Keywords: Chiari 1 Malformation, CFD, Poroelasticity, Spinal Cord

Neuro-biomechanics of Chiari malformation:

Modelling CSF flow and soft tissues of the central nervous system in the normal setting and Chiari malformation

Baracchi Samuele

Promotors: Patrick Segers, Nele Famaey, Umberto Morbiducci

Supervisor: Sarah Vandenbulcke

Abstract: The role of the Chiari 1 malformation (CM1) in the development of syringomyelia is unclear. To the best of our knowledge no studies that introduce an artificial 3D herniating on a patient specific geometry are found in the scientific literature. This study aims to give insight into the effects of an 3D artificial herniation creating a blockage in the CSF circulation, thereby highlighting the difference between a CFD and an FSI poroelastic approach. First, a model of the full circulation of the CSF has been developed. Then, using a cropped geometry, the effects of different levels of obstruction created with an artificial ellipsoid are evaluated considering first only a CFD domain surrounded by rigid walls (CFD approach) and subsequently the interaction of the CSF with a poroelastic spinal cord (FSI approach). The simulations assessed the difference between the two approaches and the effect of the obstruction in the CSF circulation.

Keywords: Chiari 1 Malformation, CFD, Poroelasticity, Spinal cord

1. Background: Chiari Malformation type 1 (CM1) is a congenital and structural defect characterized by the descent of the cerebral tonsil (lower part of the cerebellum) through the foramen magnum (opening located at the base of the skull where the it connects with the spinal cord) at least of 5 mm. The herniation caused by the CM1 disrupted the physiological circulation of the cerebral spinal fluid (CSF). More the 60% [1] of the people with CM1 developed a syrinx (fluid filled cavity) inside the spinal cord. The syrinx also known as 'syringomyelia', stress the spinal cord and leads to a severe neurological deficit. Several hypotheses have been postulated regarding the cause of the development of the syrinx but the exactly pathophysiology remain unclear. Due to the difficult to obtain in vivo data both in vitro experiment and numerical model are present in literature. Numerical model pertinent to the influence of herniation on cerebrospinal fluid (CSF) dynamics encompass computational fluid dynamics (CFD) studies, which confine their analyses to a CFD domain of the spinal SAS with rigid boundaries (Gupta et al [2]). Furthermore, FSI analysis, delve into the interplay between CSF and the poroelastic domain of the spinal cord in order to elucidate the development of syringomyelia in a simplified geometry (Bertram et al [3]). Nevertheless, to the best of our knowledge not computational study which are focusing on the effect of an artificial 3D obstruction in a patient specific geometry and located under the foramen magnum.

2-Aim of the thesis: The objective of this thesis is to obtain more insight into the effects of an obstruction, which is artificially created beneath the foramen magnum, on CSF and spinal cord biomechanics in a patient-specific geometry by using the numerical software COMSOL Multiphysics (COMSOL Inc.). To do so a first study of the full CSF circulation has been carried out to investigate if it is feasible to simulate CSF flow in the complex cranial and upper spinal CSF compartments using the numerical software COMSOL Multiphysics (COMSOL Inc). Then, to reduce computational demands, the original geometry was cropped and 3 different artificial obstructions have been introduced. Models of the different levels of obstruction have been developed using both a CFD and a FSI poroelastic approach. The latter approach grated to obtain information on the mechanical behaviour of the spinal cord and the CFS within it.

3-CFD model of the CSF circulation.

3.1 Material and Methos: A 3D in silico model has been developed in COMSOL Multiphysics (COMSOL Inc.) based on Vandenbulcke et al [4]. The geometry

used in the study is the same as the one employed by Vandenbulcke et al [4], which was derived from a T2 MRI image of a patient with CM1, with the original blockage of CSF flow associated with Chiari type 1 malformations resolved. Inlet boundary condition (depicted in figure 1) are: (1) a constant CSF production with a rate of 6.67E-03 $\frac{ml}{s}$, (2) a sinusoidal velocity waveform with a frequency of 1Hz and an amplitude of 0.11 $\frac{ml}{s}$, at the lateral ventricles to account the pulsation of the brain tissue, (3) a sinusoidal waveform with a frequency of 1Hz and an amplitude of 5.05 $\frac{ml}{s}$, in the region of the basilar artery to account the volume change in the large arteries, (4) a pulsation source term with a frequency of 0.2Hz and an amplitude of 1.01 $\frac{ml}{s}$, at the region of the cerebral occipital veins to account the respiratory pulsation.

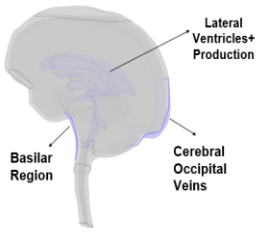

AREA	Type	Average (ml/s)	Amplitude (ml/s)
Lateral Ventricles	Constant	6.67E-03	/
Lateral Ventricles	Sine wave 1Hz	/	0.11
Basilar Region	Sine wave 1Hz	/	5.05
Occipital Veins	Sine wave 0.2Hz	/	1.01

Figure 1: Overview of the inlet boundary conditions

As the outlet boundary condition (Figure 2), a zero-pressure condition is set for the outlet corresponding with the arachnoid villi. For the other outlets, a volumetric flow is imposed, which is calculated by summing all the inlet boundary conditions and then multiplying these with the net outflow percentage specific to each outlet. The outlet percentages for the spinal drainage pathway, lymphatic system, and interstitial space are set at 20%, 30%, and 20%respectively.

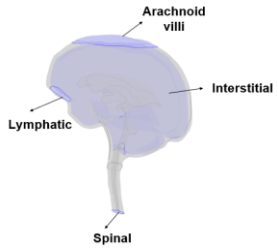

	Spinal	Lymphatic	Internal
% of total inflow	20	30	20

AREA	Type	Average (Pa)	Amplitude
Arachnoid villi	Const	0	/

Figure 2: Overview of the outlet boundary conditions

Based on mesh sensitive mesh analysis, the mesh with 107.868 elements had been selected. The CSF has been modelled as incompressible and with the same proprieties as water (density = 998.2 $^{Kg}/_{m^3}$; dynamic viscosity = 0.001003 $^{Kg}/_{ms}$). CFS flow is driven by the Navier- Stokes equation. The model simulates 5 cardiac cycles, automatic time stepping built in COMSOL Multiphysics (COMSOL Inc.).

3.2 Result: In Figure 3 the flow through a cross section of the spinal SAS for the 5 cardiac cycles has been calculated. The amplitude of the pulsation ranges from 1.5 to -2 m³/s.

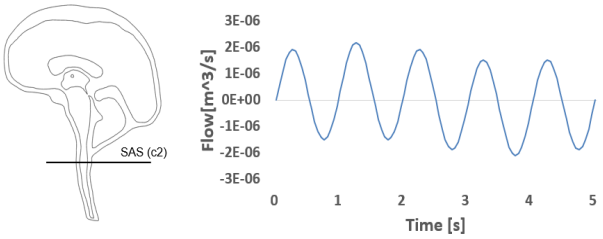

Figure 3: CSF through a cross section in the spinal SAS

The maximal velocity at the cerebral aqueduct is 3.027 $\frac{cm}{s}$ The pressure difference between a point in the lateral ventricles and the mean pressure in the plane of the spinal SAS are presented in figure 4, where the maximal value of the pressure difference has an amplitude of 0.0093 mmHg.

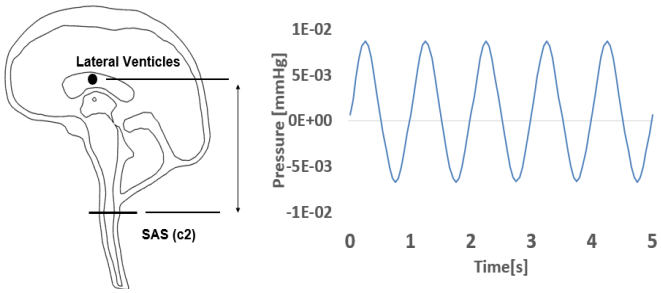

Figure 4: Pressure between a point at the lateral ventricles and a plane in the spinal SAS

3.3 Discussion: The flow evaluated in spinal SAS and the maximal velocities at the cerebral aqueduct are in a good agreement with the study of Vandenbulcke et al. [3]. On the other hand, the amplitude of the pressure drops between the lateral ventricles and the spinal SAS seems to be underestimated in this model compared to the study by Vandebulcke et al [3] and Filligham et al [5] that obtain values in the range of 0.015 mmHg while this study a value of 0.0093 mmHg. This model does not account for the brain tissue compliance, whether by using a windkessel model (as done in (3)) or employing a FSI approach. Due to these limitations, it is only possible to obtain relative pressure values in this study.

4- CFD study on the effect of the obstruction

The objective of this chapter is to examine the impact of a 3D obstruction at the foramen magnum due to

CM1.

4.1 Material and Methods: To reduce the computational demand of the simulation the geometry of the full SAS has been reduced by cropping 6 cm above and 14.8 cm below the plane with z zero coordinate. In order to create and simulate different level of obstruction, an idealized 3D model of the obstruction has been created using an ellipsoid. To have a quantification of the level of the obstruction, the geometry has been intersected with a plane 25mm below the top of the geometry. The equation below has been used to quantify the % of the obstruction:

$$\%Obstruction = \frac{AreaFM - AreaHerniation}{AreaFM}$$

4 levels of obstruction have been created respectively: the healthy condition, the 40%, the 60% and 100% of obstruction.
The inlet boundary conditions are determine based on the in vivo PC-MRI flow data. Flow was specifically measured in vivo in the spinal SAS at the C2 level and in the cerebral aqueduct. The flow extract from the cerebral aqueduct is directly applied to the corresponding area at the end of the cerebral aqueduct (Inlet 1) while, the difference between the flow rate from the SAS at the C2 level and the cerebral aqueduct is applied to the designated region called inlet 2.A pressure of 10mmHg has been imposed at bottom part of the spinal SAS

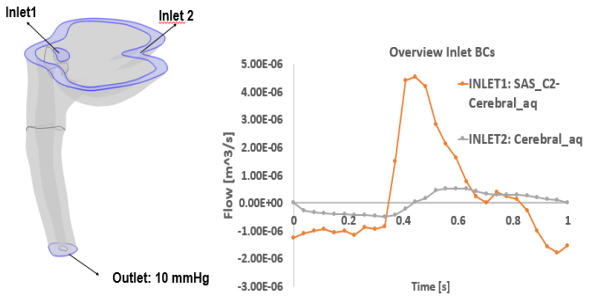

Figure 5: Overview of boundary condition on the cropped geometry

The mesh has been created using a boundary layer composed of prismatic elements surrounding the spinal cord surface. The rest of the geometry is composed free tetrahedral element. Based on a mesh sensitive analysis, the mesh with 86.456 elements has been chosen. Four simulations, each with a different degree of the obstruction, were conducted by solving the Navier-Stokes equation, assuming the CSF to be incompressible and possessing the same properties as water (viscosity = 0.001003 $^{Kg}/_{ms}$, density = 998.2 $^{Kg}/_{m^3}$). The model simulates 1 cardiac cycle, using a time step of 0.01s.

4.2. Result: In order to study the effect of the obstruction, two cross-sectional planes were generated—one aligned with the herniation level and another below it. These planes were employed to analyse the localized effects both at the obstruction site and in the region immediately below it.

The figure 6 represents the maximal velocities in the plane below the obstruction for the different levels of obstruction. The graph shows a clear difference between when the obstruction is present and the healthy condition, while the effect of the degree on the obstruction seems to not influence the maximal velocities

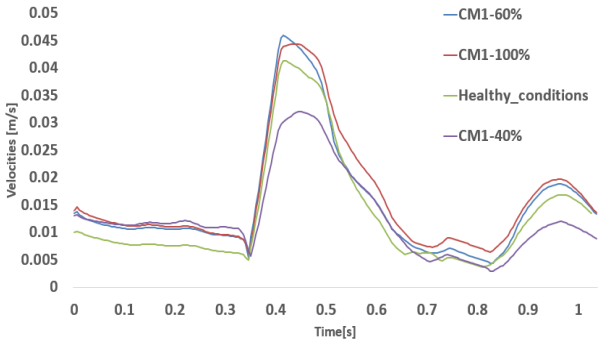

Figure 6: Maximal velocities along the cardiac cycle with the different level of obstruction below the obstruction

Figure 7 represents the maximal velocities at the level of the herniation and shows that the maximal velocity increases with an increasing percentage of obstruction.

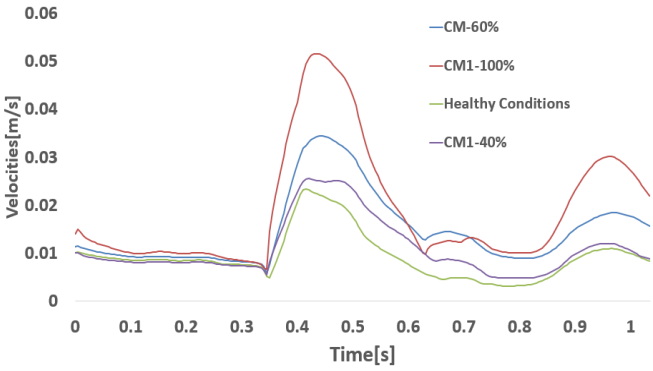

Figure 7: Maximal velocities along the cardiac cycle with the different level of obstruction at the level of the herniation

The pressure drops between the cerebral aqueduct and the spinal SAS (using the plane below the obstruction) has been evaluated in Figure 8 showing that increasing the level of the obstruction the pressure drops increase passing from a peak of 4.6 Pa in the healthy condition to 19.9 Pa in the 100% obstruction.

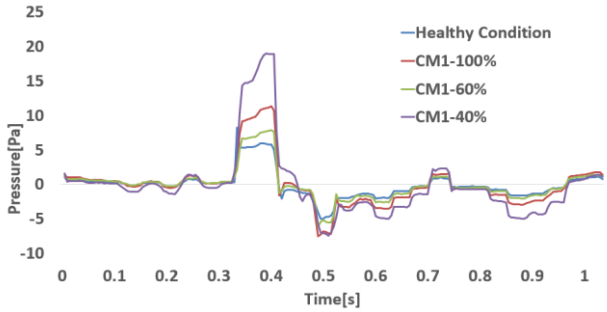

Figure 8: Pressure drops between the cerebral aqueduct and the plane below the obstruction along the cardiac cycle

Discussion: In this section the effect of an artificial 3D obstruction has been evaluated at the level of the obstruction and below it. From figure 6, it appears that an increase in degree of the obstruction doesn't necessary lead to an increase in velocities below the obstruction and that these velocities only indicate the presence of the obstruction. On the other hand, a non-linear relation between the level of the obstruction and the maximal velocities at the level of the herniation was observed. Finally, an increase in pressure drop between the cerebral aqueduct and the plane below the obstruction with a higher percentage of obstruction is noticed. These findings are in agreement with the study of Gupta et al [2] which stated that that solely looking at velocities field below the obstruction can indicate the presence of herniation, but evaluating pressure provides insight into the degree of obstruction.

5- FSI poroelastic study of the effect of the obstruction

5.1-Material and Methods: The poroelastic approach granted to both consider the mechanical proprieties of the spinal cord and the CSF between the SAS and the spinal cord. The computational model has been built in COMSOL Multiphysics (COMSOL Inc.) using the approach by Silvera [6]. The flow in the SAS was modeled according to the Navier Stokes's equations while the CSF flow inside the spinal cord was modelling with the Brickman's equation. Two setups have been considered in this section: (1) the FSI poroelastic study without the obstruction to study the effect of the PIA mater and (2) the FSI poroelastic study with different levels of obstruction.

Study 1: The geometry is the same of the one that has been used for the CFD setup with the introduction of the spinal cord domain. To provide insight into the influence of the PIA mater one simulation has been run without the Pia mater and the other with. The Pia mater has been modelled has a 'Thin elastic layer' around the domain of the spinal cord with a thickness of 11.5 µm. The material proprieties are based on the studies carried out by Bertram et al [2] which consider the matrix of the poroelastic material as linearly elastic with isotropic mechanical proprieties. Figure 9 summarizes the material proprieties.

MATERIAL	Density [kg/m^3]	Dynamic Viscosity [Pa*s]	Porosity	Permeability [m^2]	Poisson Ratio [-]	Elastic Modulus [Pa]
Cord	1000	7e-4	0.3	1E-13	0.35	5000
Water	1000	1e-3	/	/	/	/
PIA mater	1000	/	/	/	0.49	1250000

Figure 9: Material proprieties based on the study of Bertram (2)

Boundary conditions are the same as those of the CFD study (section 4). The spinal cord has been fixed both at the top and the bottom end. The computational mesh is composed of tetrahedral elements and to improve the convergence [7] a boundary layer of prismatic elements around the spinal cord at the interface between the fluid and the poroelastic material has been added. After a mesh sensitive analysis, a mesh having 58.204 elements has been chosen.

Study2: The geometry and the materials in this setup are the same of those used for the study1 in which 3 levels of obstruction has been added. The geometry of the herniation is the same as those used for the CFD study with 40%, 60% and 100% obstruction. The herniation has been modelled as a porous domain with the same permeability and porosity as the spinal cord. Boundary conditions are the same as those in study1, with the only difference that in the simulation with the 100% obstruction, the area between the spinal cord and the porous domain has been considered fixed. Due to the high computational demands, for the 40% and 60% obstruction the same mesh has been used as for study1, while due to the limitation of the fixation between the spinal cord and herniation a less fine mesh has been used for the 100% obstructing with a total number of elements of 25.204. The model simulates 1 cardiac cycle, using a time step of 0.01s

5.2-Results: Study1: The aim of this setup was to evaluate if the pia mater has an influence on the results. For the pressure drop between the cerebral aqueduct and the plane below the obstruction and volume exchange between the SAS and spinal cord no difference has been found. On the other hand, the maximal velocity waveforms demonstrate a short delay of the one with the pia mater compared to the one without the pia as reported in figure 10.

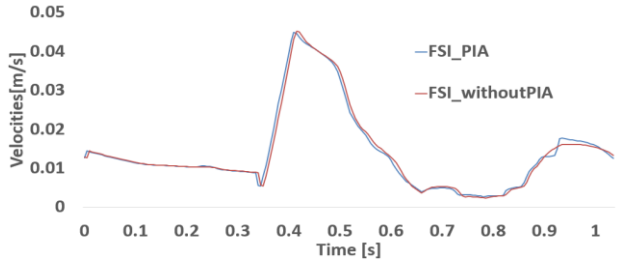

Figure 10: Maximal velocities evaluated in the plane below considering the effect of the PIA mater

Setup2: The poroelasticity FSI granted to consider the tissue of the spinal cord and study the CSF inside the spinal cord. To underline the mechanical behaviour the spinal cord the Von Mises stress with the relative deformation has been represented figure 11 at time 0.85s. Due to the lower quality of the mesh and the strong limitation of the fixed boundary between the spinal cord and the herniation which led in a strong stress and pressure concentration located in that region, the 100% percent of herniation has been omitted from the discussion.

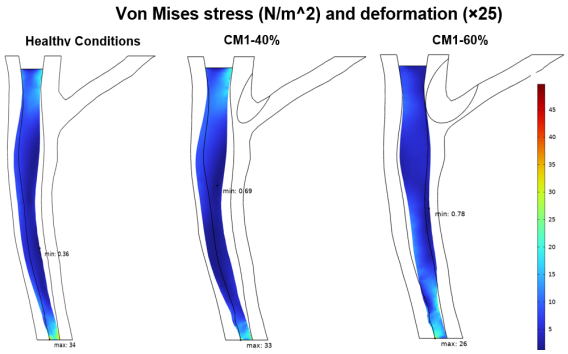

Figure 11: Von Mises Stress and relative deformation at t=0.85

Figure 12 represents the velocity contour inside the spinal cord at time 0.85s, to underline how the different mechanical behaviour may have an impact of the flow inside the spinal cord.

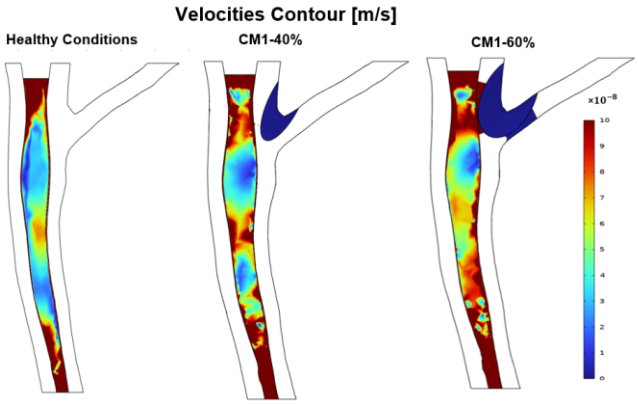

Figure 12: Velocities contour inside the spinal cord

Figure 13 represents the comparison between the FSI and CFD approach for the maximal velocities at the plane below the obstruction

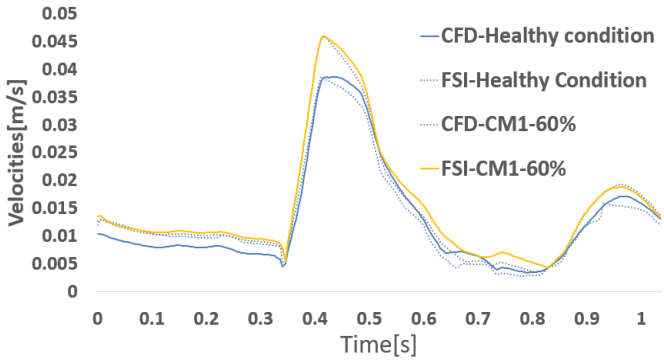

Figure 13: Comparison between FSI and CFD approach, max velocities in the SAS (c2)

Knowing that looking solely at the velocities not always suffices to obtain insight regarding the added value of the FSI simulation the pressure drop between the cerebral aqueduct and the plane below the obstruction is also depicted in Figure 14.

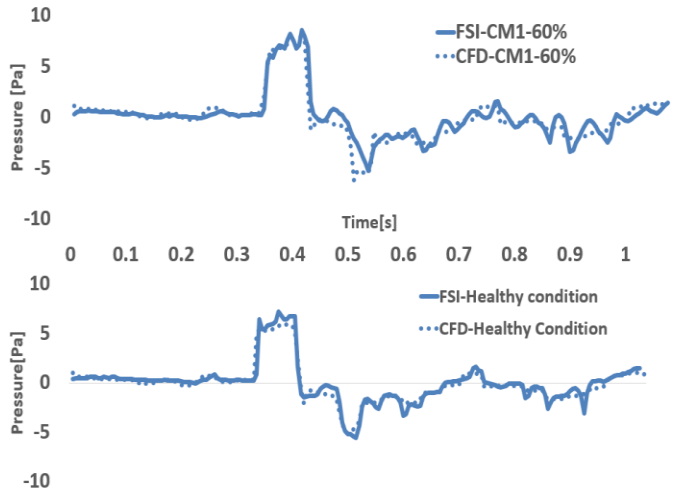

Figure 14: Comparison between FSI and CFD, pressure drop between cerebral aqueduct and spinal SAS c2. First row depicted the healthy condition while the second and the CM1 with the 60%

5.3-Discussion: The aim of this section was to give an insight into the effect 3D artificial obstruction using the poroelastic FSI approach. From the Figure 11, it appears that the presence of CM1 with the 60% obstruction alters the deformation behaviour of the spinal cord throughout the cardiac cycle (spinal cord moves posterior instead of anterior). This possibly influences the overall fluid exchange pattern due to the different stress distribution and might increasing the amount of fluid forced through the pia into the spinal cord. Moreover, the figure 12 highlights the change in the distribution of the velocities inside showing that with increasing degree of obstruction larger areas with high velocities are noticed. Nevertheless, the low velocities inside the spinal cord do not suggest a proper fluid exchange between the spinal cord and the SAS. Moreover, the time scale of the simulation is much

shorter than the of syrinx formation. Further studies introducing the syrinx in the spinal cord could highlight a flow volume difference in the spinal cord.

In figure 13 and 14 the difference in velocities and pressure between the CFD and FSI approach appear to be limited suggesting that an FSI approach might not provide additional information on these parameters. Thus, the same conclusion of the CFD simulation can be drawn stated that the effect of degree obstruction it's evident only focusing local in the area of the obstruction.

The model incorporates a number of simplifications, including the assumption of isotropy for all material properties and the consideration of an elastic material matrix devoid of any initial prestress. Furthermore, the inclusion of anatomical structures within the spinal SAS, such as trabeculae, ligaments, and nerve roots, has been entirely omitted. Additionally, it is important to note that the geometry utilized in this study only represents a partial segment of the entire SAS

6-CONCLUSION

In summary, this investigation has provided enhanced insights into the implications of an artificial three-dimensional obstruction by employing two distinct FEA techniques: CFD and the poroelastic FSI. The findings of this study reveal that the introduction of the FSI approach did not notably contribute to enhancing the comprehension CSF flow within the spinal SAS but does provides additional information concerning fluid exchange and stresses within the spinal cord. Hence, depending on the area of interest, these findings might facilitate, selection of the most suitable approach for subsequent simulations. Future endeavours could involve incorporating material property anisotropy and accounting for anatomical structures within the SAS. Furthermore, refining the modeling approach for the 100% obstruction of the back portion of the spinal SAS remains an avenue for improvement. Finally, a full 3D model of the SAS can help to underline phenomena difficult to observe in the cropped geometry.

References

(1) Ken Sakushima, Satoshi Tsuboi, Ichiro Yabe, Kazutoshi Hida, Satoshi Terae, Ritei Uehara, Imaharu Nakano, Hidenao Sasaki, Nationwide survey on the epidemiology of syringomyelia in Japan, Journal of the Neurological Sciences, Volume 313, Issues 1–2, 2012, Pages147-152, https://doi.org/10.1016/j.jns.2011.08.045.].

(2) Gupta, S., Soellinger, M., Boesiger, P., Poulikakos, D., and Kurtcuoglu, V. (December 10, 2008). "Three-Dimensional Computational Modeling of Subject-Specific Cerebrospinal Fluid Flow in the Subarachnoid Space." ASME. J Biomech Eng. February2009;131(2): 021010.https://doi.org/10.1115/1.3005171

(3) C. D. Bertram and M. Heil, "A Poroelastic Fluid/Structure-Interaction Model of Cerebrospinal Fluid Dynamics in the Cord with Syringomyelia and Adjacent Subarachnoid-Space Stenosis," Journal of Biomechanical Engineering, vol. 139, no. 1, 2017, doi: 10.1115/1.4034657

(4) Vandenbulcke, Sarah et al. "Computational fluid dynamics model to predict the dynamical behavior of the cerebrospinal fluid through implementation of physiological boundary conditions." Frontiers in bioengineering and biotechnology vol. 10 1040517. 22 Nov. 2022, doi:10.3389/fbioe.2022.1040517

(5) Patrick Fillingham, Swati Rane Levendovszky, Jalal Andre, Carolyn Parsey, Michael Bindschadler, Seth Friedman, Mehmet Kurt, Alberto Aliseda, Michael R. Levitt,Patient-specific computational fluid dynamic simulation of cerebrospinal fluid flow in the intracranial space, Brain Research, Volume,https://doi.org/10.1016/j.brainres.2022.14796

(6) C. A. Silvera Delgado, "Modelling the lymphatic system: Computational model of lymphatic capillaries-interstitium interaction in normal physiological and pathological conditions.," Torino, 2017.

(7) Pietro Matchovich, '' Study of spinal cord poroelastic behaviours under Chiari Malformation conditions: A computational dynamics study," Ghent, 2021

Summary

List of Figures

List of tables

List of Abbreviation

CFD ..... Computational Fluid Dynamics

CM ..... Chiari Malformation

CM1 ..... Chiari Malformation type 1

CNS ..... Central Nervous System

PNS ..... Peripherical Nervous System

CSF ..... Cerebrospinal fluid

FSI ..... Fluid Structure Interaction

MRI ..... Magnetic Resonance Imaging

PC-MRI ..... Phase contrast Magnetic Resonance Imaging

PFD ..... Posterior Fossa Decompression

PFDD ..... Posterior Fossa Decompression with Duraplasty

SAS ..... Subarachnoid space

SAS(c2) ..... Subarachnoid space 2nd vertebrae level

List of symbols

ρ	Density	$\frac{Kg}{m^3}$
$\vec{v}$	Velocity	$\frac{m}{s}$
$\vec{P}$	Pressure	Pa
μ	Viscosity	Pa s
$\vec{F}$	Volume forces	N
$\overrightarrow{v_d}$	Fluid velocity inside porous medium	$\frac{m}{s}$
k	Permeability	m^2
Q_m	Mass source	$\frac{Kg}{m^3 s}$
ϵ_p	Porosity	
e_i	Normal component of strain field	
τ_{ij}	Tangential component of strain field	
σ_i	Component of normal stress field	Pa
γ_{ij}	Component of shear stress field	Pa
H	Biot's constant. Measure the compressibility of the porous medium for a change in fluid pressure	Pa
Q	Biot's second constant (amount of water entering a porous block while the volume of the block is constant).	Pa
E	Young's modulus	Pa
G	Shear modulus	Pa
v	Poisson's ratio	
$\vec{\varepsilon}$	Strain Field	
υ	x component of the displacement	m
ν	y component of the displacement	m
ω	z component of the displacement	m
α	Biot's coeficient	
Θ	Increment of water content	

Chapter 1

1 INTRODUCTION

1.1 Background

This first chapter aims to give a general overview of neuroanatomy to give the basic notion to navigate through the exposed work.

1.1.1 Central Nervous System Anatomy

Anatomically, the nervous system can be classified into two primary divisions: the central nervous system (CNS) and the peripheral nervous system (PNS), as depicted in Figure 1: Main part of the nervous systemThe CNS comprises the brain and spinal cord, while the PNS encompasses the remaining components of the nervous system that connect the CNS to the rest of the body. However, it's important to note that this division is oversimplified, as some elements of the peripheral nervous system are found within the cranial or vertebral cavities, challenging the universality of this classification (1).

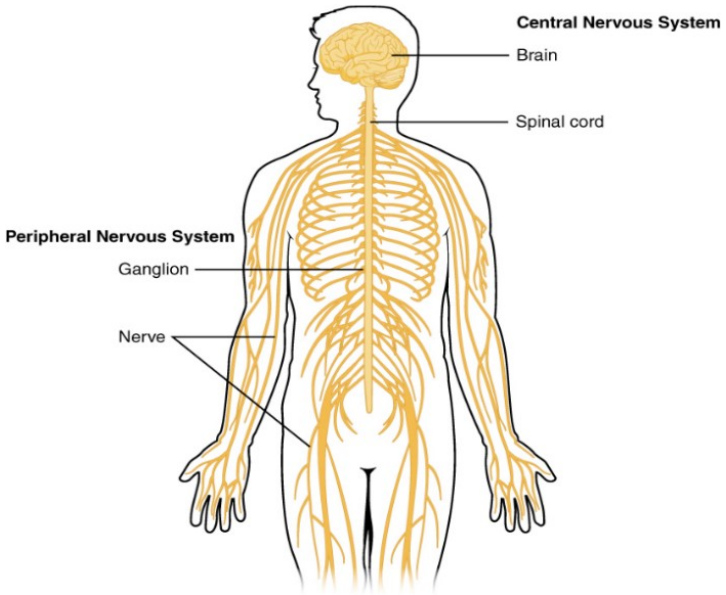

Figure 1: Main part of the nervous system (1)

The CNS can be further subdivided into distinct components: the spinal cord, which is situated within the vertebral canal, and the brain, which is housed within the skull.

1.1.2 Nervous tissue: gray matter and white matter

The CNS is composed of two types of tissue on a macroscopic level: gray matter and white matter. These tissues differ in their cellular composition, resulting in distinct colors and mechanical properties. White matter primarily consists of myelinated axons and contains only a small number of neuronal cell bodies, forming the connection between different neurons within the CNS. Its light color is attributed to the presence of myelin sheaths surrounding the axons. On the other hand, grey matter lacks myelin and consists of nerve cell bodies, dendrites, and the terminal parts of axons. (2)

1.1.3 Main Part of the brain

The main parts of the brain are the cerebrum, cerebellum, and brainstem, which are illustrated in Figure 2. The cerebrum, the largest part of the brain, is divided into two hemispheres - the right and left hemispheres - separated by the longitudinal fissure. Within this deep fissure lies the corpus callosum, a bundle of 200 million nerve cells that connect the two hemispheres. The outer surface of the cerebrum is called the cerebral cortex, which exhibits extensive folding in the human brain. The folds are referred to as convolutions or gyri, while the grooves between them are called fissures or sulci. (2)

These hemispheres are further subdivided into distinct lobes, each with specific functions. For instance, the frontal lobe is responsible for voluntary movement, reasoning, planning, and short-term memory. The temporal lobe, on the other hand, is involved in hearing, language recognition, and long-term memory. The parietal lobes integrate sensory information, while the occipital lobe governs vision. (3)

The cerebellum, positioned beneath the cerebrum, coordinates muscle movements, posture, and balance. Its surface area is extensively folded, increasing its capacity to process information. The cerebellar tonsils, located at the lowest part of the cerebellum, contribute to the coordination of movement, balance, and posture. Lastly, the brainstem connects the cerebrum and cerebellum to the spinal cord. The brainstem regulates various automatic functions, including breathing, heart rate, body temperature, sleep-wake cycles, digestion, coughing, sneezing, vomiting, and swallowing (3) .It is anatomically divided into three parts: (1) the medulla, extending from the spinal cord to the pons and positioned anteriorly to the cerebellum; (2) the pons, protruding forward from the upper section of the medulla and housing two respiratory centers that collaborate with those in the medulla to regulate breathing patterns; (3) the midbrain, extending from the pons to the hypothalamus the cerebral aqueduct, a tunnel connecting the third and fourth ventricles. Different kinds of reflexes are coordinate by the midbrain, including visual and auditory reflexes.

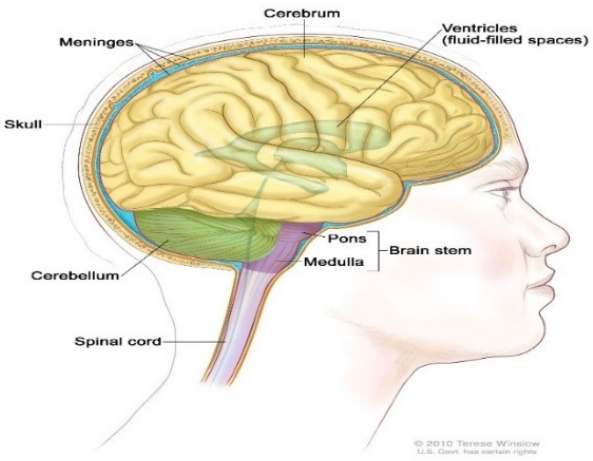

Figure 2: Main part of the brain

1.1.4 Spinal Cord

The spinal cord is a long, thin, tubular bundle of nerve tissue and support cells that in length extends from the foramen magnum, which is a hole in the bae of the skull, to the disc between the first and second lumbar vertebrae. The spinal cord is divided into segments, which correspond to the level of the vertebrae It is enclosed and protected by the vertebrae of the spine. There are 31 segments of the spinal cord, with each segment giving rise to a pair of spinal nerves that innervate specific regions of the body, as depicted in Figure 3. The spinal nerves carry information from receptors around the body to the spinal cord. From here the information passes to the brain for processing. Spinal nerves also transmit motor information from the brain to the body's muscles and glands. (2)

The interior of the spinal cord is composed of grey matter, which has a letter H-like shape and consists of nerve cell bodies, dendrites, and unmyelinated axons. The grey matter is organized into horns, which are named for their location in the spinal cord. The dorsal horns contain sensory neurons that receive input from the peripheral nerves and send it up to the brain, while the ventral horns contain motor neurons that send signals to the muscles and glands. (3)

The white matter of the spinal cord surrounds the grey matter and consists of myelinated axons that form tracts. These tracts are arranged in columns or funiculi, which are also named according to their location in the spinal cord. The white matter carries information up and down the spinal cord between the brain and the peripheral nerves.

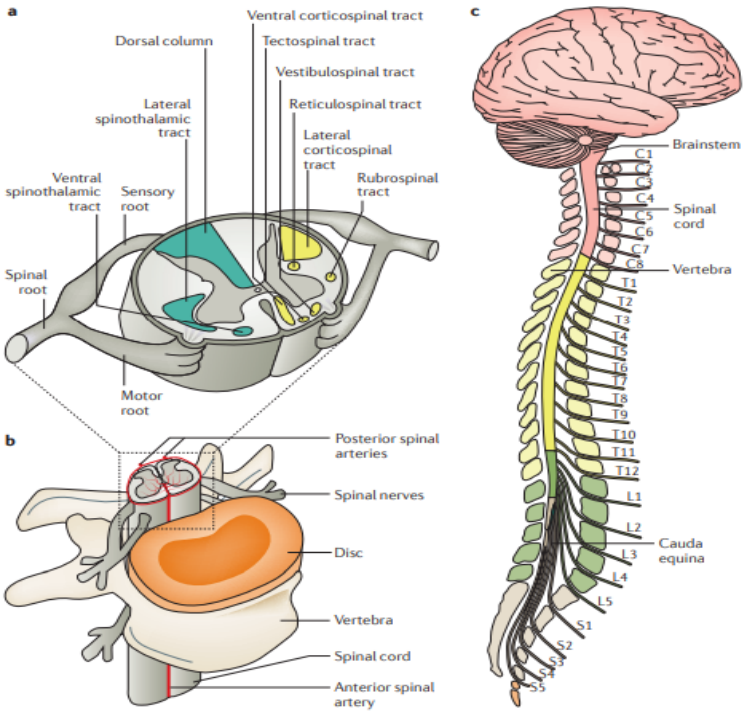

Figure 3: Spinal cord anatomy

1.1.5 Meningeal layers and subarachnoid space

In vertebrates, the brain is protected by the bony skull, while the spinal cord is situated within the vertebral column. The peripheral nerves of the SNP enter and exit the spinal cord through small openings in the vertebrae. Between the skull and the CNS, there are three layers of tissue membranes known as meninges, which primarily serve to protect the brain. These meninges are illustrated in Figure 4.

The outermost layer is called the dura mater, which gets its name from Latin, meaning "tough mother." It is a robust and thick layer composed of fibrous connective tissue. The dura mater acts as a protective covering for the brain, enclosing both the central nervous system and the major blood vessels that enter the skull and vertebral canal *(3)*.

The arachnoid mater, the middle layer of the meninges, surrounds the central nervous system and forms a sac-like enclosure around it. The subarachnoid space (SAS), located between the arachnoid and the innermost layer called the pia mater, is filled with cerebrospinal fluid (CSF). The circulating CSF provides a liquid cushion for the brain and spinal cord. The SAS contains connective tissue, called trabeculae, which extend through its depth and function to keep the brain suspended in place. The SAS is also crossed by veins and blood vessels.

The pia mater, which gets its name from Latin, signifying "gentle mother," is the innermost layer. It is an extremely thin membrane that envelops the surface of the spinal cord and brain. Composed of a thin layer of connective tissue containing abundant elastic fibres, the pia mater is made up of flattened cells that closely surrounded the brain and spinal cord (2).

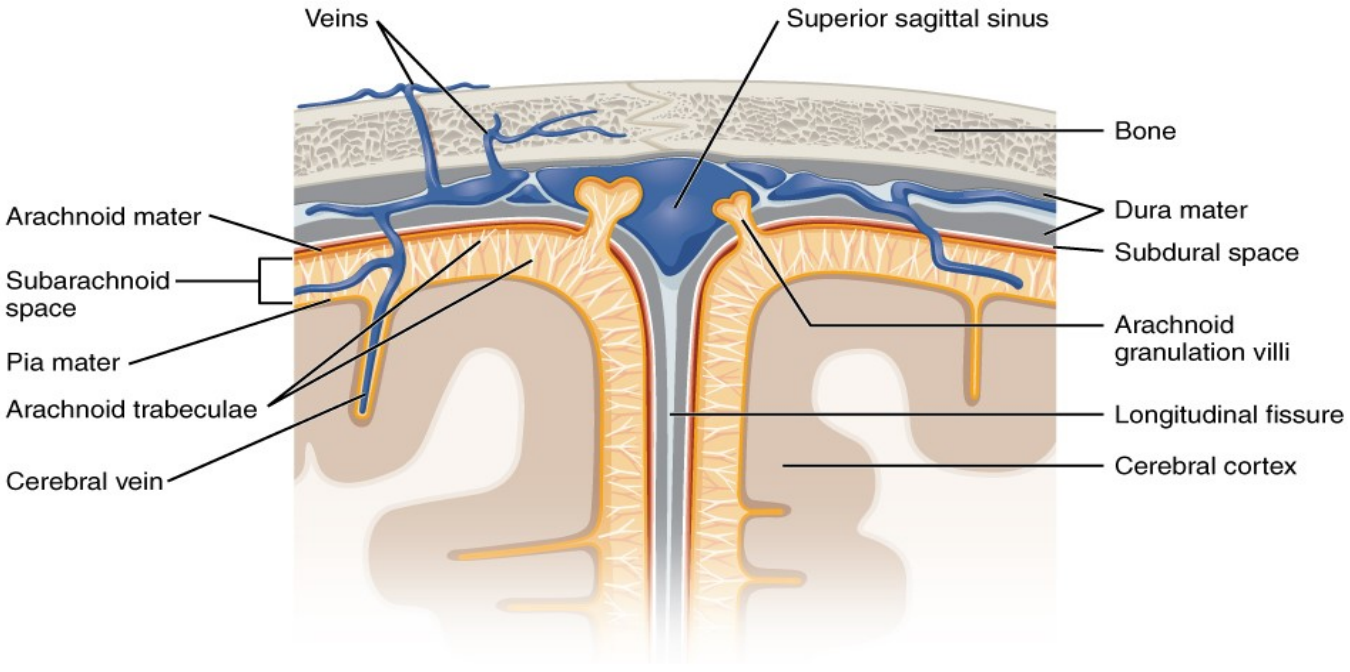

Figure 4: Meningeal layers of superior sagittal sinus

1.1.6 Cerebrospinal fluid System and Circulation

CSF is a clear and colorless liquid that circulates within the brain's ventricles and the SAS surrounding the brain and spinal cord. Composed of water, electrolytes, glucose, and proteins, CSF serves various essential functions in the CNS (4). CSF plays a vital role in protecting the CNS. It acts as a cushioning fluid, surrounding the brain and spinal cord, providing a protective barrier against physical trauma. Additionally, it transports nutrients to CNS neurons and removes waste products, contributing to their proper functioning. CSF also helps maintain immunological and biochemical homeostasis in the CNS. Finally, by buoying the brain, CSF reduces its overall weight and prevents compression due to its weight, relieving pressure within the skull (5).

CSF is mainly produced in the brain's lateral ventricles, primarily by specialized cells called choroid plexuses located in the ventricles. The choroid plexus secretes around 80-90% of CSF and is a highly vascularized structure composed of epithelial cells. These cells form a blood-CSF barrier surrounds capillaries and controls the movement of solutes and water to regulate CSF composition. Under normal conditions, the total volume of CSF in humans ranges between 150 and 160 mL (6).

The flow of CSF occurs in a closed system within the CNS. CSF is produced by the choroid plexus in the lateral ventricles of the brain. From the lateral ventricles, the CSF flows through the interventricular foramina to enter the third ventricle. Here a second choroid plexus produces more CSF. Next, the CSF passed through the mesencephalic aqueduct of the midbrain, and into the fourth ventricles, where further CSF is added by a third choroid plexus. From here it passed through the median aperture and lateral aperture into the subarachnoid space. Finally, the CSF circulates down and around the brain and the spinal cord in the SAS (7)

According to the traditional view, CSF is reabsorbed from the cranial SAS through arachnoid villi, as depicted in Figure 5, into the blood within the cranial venous sinuses (large veins within the double-layered cranial dura mater). This reabsorption process converts CSF back into the blood plasma, with the rate of reabsorption typically matching the rate of production. Ongoing research has challenged the classical understanding of CSF drainage, which dates back to the eighteenth century and is based on anatomical observations. Besides the absorption of the arachnoid villi, recent findings suggest the involvement of the lymphatic system as an alternative drainage pathway. A recent study has shown the transportation of CSF to cervical and spinal lymphatics, indicating that lymphatic vessels serve as the main pathway for CSF outflow (5). CSF movement is believed to be driven by: convective flow and pulsatile flow (8). Convective flow refers to the movement in a single direction, guided by pressure differences between the high-pressure choroid plexus and the low-pressure arachnoid granulations, as originally believed. However, recent studies have raised doubts about the assumption of unidirectional CSF displacement and proposed the existence of pulsatile flow. Pulsatile flow suggests that CSF moves bidirectionally, both upward (cranial) and downward (caudal) along the spinal cord without net unidirectional CSF displacement. (7) (8)

The driving force of the pulsatile flow of CSF are driven by the cardiovascular and respiratory cycles. The cardiovascular pulsation, as demonstrated in the study conducted by Mestre et all (52) by particle tracking in live mice, seems to be the principal driving force of the CSF pulsation. When intracranial arteries expand during systole and restrict during systole, CSF undergoes movement within and out of the cranial compartment causing the pulsation (10). Respiration also impacts CSF motion, as changes in venous blood volume occur with the respiratory cycle. Exhalation increases intrathoracic pressure and in turn reduces venous blood returning from the brain. This causes CSF to flow downwards to compensate for increased intracranial venous blood volume. Meanwhile, deep inhalation leads to cranial (upward) CSF flow due to decreased intrathoracic pressure. Respiratory events like coughing, sneezing, or the Valsalva manoeuvre can disrupt pressure environments and affect the magnitude, frequency, and direction of CSF flow (10), (11), (12).

The regulation of CSF secretion and turnover is crucial, and disruptions can occur in certain neurological disorders. Hydrocephalus, characterized by an imbalance in CSF production, circulation, or absorption, leads to an excessive volume of CSF or increased pressure inside the skull, causing brain compression and functional impairments in adults. Chiari malformation and syringomyelia, associated with Chiari malformation, are another CSF-related condition. Further information regarding these conditions will be provided in subsequent chapters.

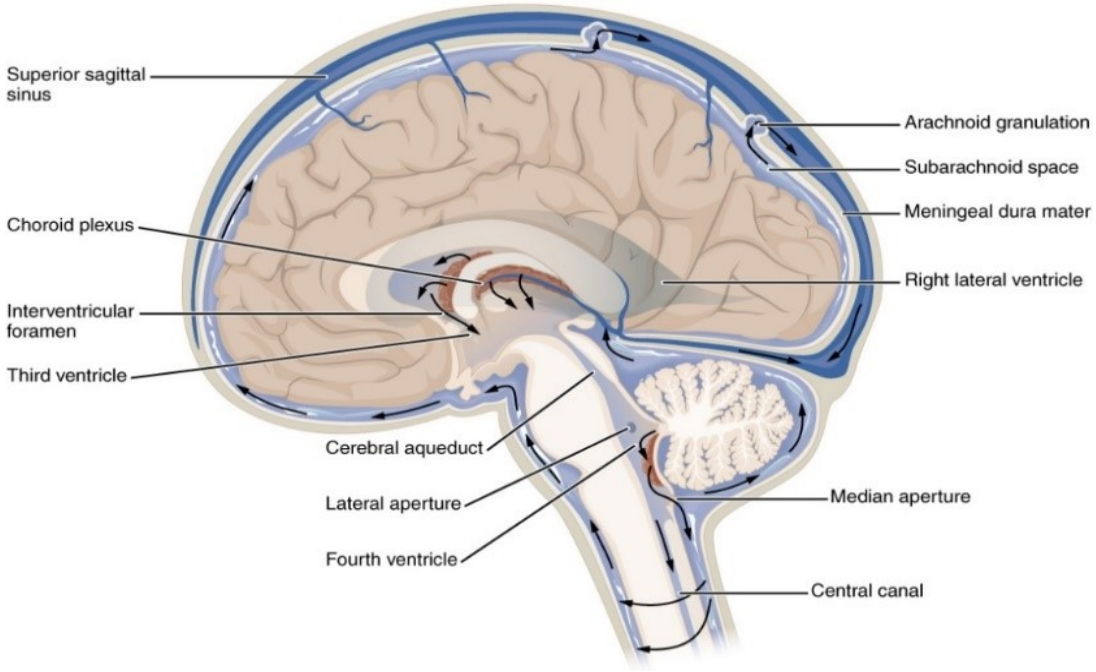

Figure 5: Image of CSF circulation in the cervical spinal SAS and cranial SAS

Chapter 2

2 CHIARI I MALFORMATION

2.1 Pathophysiology

Chiari malformations have in common the presence of anatomical deformities of the brainstem and cerebellum. They are named after Hans Chiari, the Austrian pathologist who described in 1891 a malformation involving the brainstem, cerebellum, upper spinal cord, and surrounding bone. Chiari malformation (CM) is considered a congenital condition, although acquired forms of the condition have been diagnosed. In the 1890s, a German pathologist, Professor Hans Chiari, first described abnormalities of the brain at the junction of the skull with the spine. He categorized these in order of severity; types I, II, III, and IV. (13) . CMs refer to abnormalities in the structure of the brain where the lower portion of the brain protrudes through the opening in the skull base, foramen magnum, into the spinal canal.

A CM may develop when a part of the skull is smaller or malformed, causing pressure on the brain and pushing the cerebellum downward into the spinal canal. This can create compression on the brain stem and spinal cord, leading to blockages in the flow of CSF. (13)

CMs are categorized based on the severity of the condition and the parts of the brain that it involves.

• Type I:

The most prevalent form of CM is Type I, characterized by the descent of cerebellar tonsils through the foramen magnum as depicted in Figure 6. It is typically observed during adolescence or adulthood and may be incidentally discovered during examinations for unrelated conditions. Although individuals with Type I Chiari malformation may initially be asymptomatic, they can develop symptoms later in life (12).

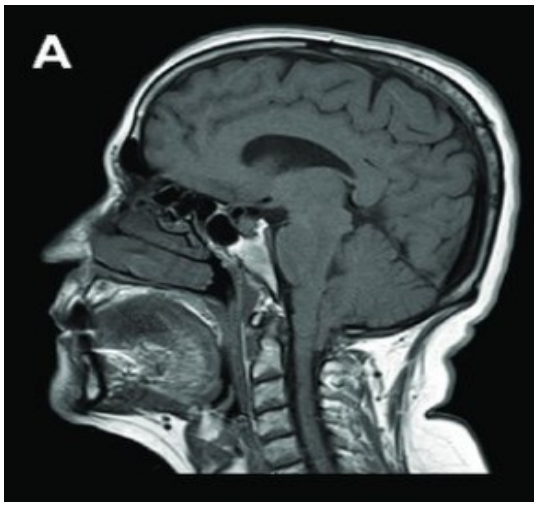

Figure 6: Sagittal x-rays of a patient with CM1

• Type II:

Type II Chiari malformation, represented in is characterized by the protrusion of both cerebellar and brain stem tissue into the foramen magnum, the opening at the base of the skull. It frequently occurs alongside

myelomeningocele, a condition in which the spine and spinal cord fail to develop properly, resulting in an open spinal canal across multiple vertebrae that may lead to paralysis below the affected region. Symptoms of Type II CM typically appear during childhood and are more severe when compared to Type I. Surgical intervention, known as Arnold-Chiari malformation, is necessary for the management of this conditions (14).

Figure 7: Sagittal x-rays of a patient with Chiari Malformation type II (13)

• Type III:

Type III represents the most severe variant of CM, characterized by the protrusion of parts of the cerebellum and brain stem through an abnormal skull opening coupled with an occipital or upper encephalocele, a sac like protrusion of the brain (62), as depicted in Figure 8. The condition may also involve the membranes surrounding the brain or spinal cord. Symptoms typically emerge in infancy and can lead to profound and life-threatening complications, including seizures and cognitive and physical development delays (14).

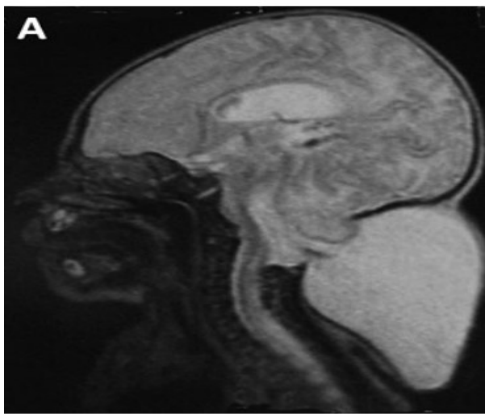

Figure 8: Sagittal x-rays of a patient with Chiari Malformation type III

• Type IV:

Type IV is a rare form of CM, in which there isn't a protrusion of the cerebral tonsils but the cerebellum is not completely developed. This condition is known as hypoplasia. (14)

2.2 Chiari I Malformation

Chiari I malformation (CM1), also known as hindbrain herniation, is a structural abnormality in which a portion of the cerebellum (a part of the brain responsible for movement coordination) extends into the spinal canal through the opening at the base of the skull (Figure 9). CM1 is characterized by caudal migration of the cerebellar tonsils below the foramen magnum by more than 5 mm (16). A descent of less than 3 mm is considered a no-pathological variant, while a herniation between 3–5 mm is borderline and needs radiological follow-up in symptomatic cases. (17)

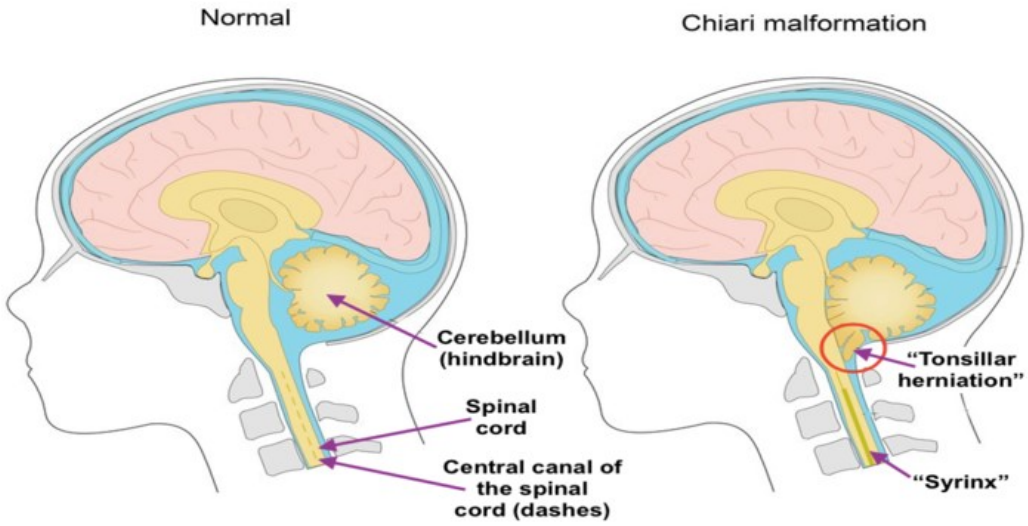

Figure 9: Anatomy of healthy condition and pathologic condition CM1

CM-1 is the most common Chiari malformation. It is estimated to occur in approximately every 1 in 1000 births, with a slight female predominance of 1.3 to 1 (18).

Probably, the epidemiological data is underestimated, since many forms producing only a few mild symptoms- and manifest themselves clinically only in adulthood. Indeed, neuroimaging data suggest that the clinical condition may be more frequent, with an estimated prevalence of 1% in the pediatric population.

2.2.1 Symptom

Headaches (usually at the back of the head but can be anywhere) are the most common complaint and neck pain is also common. The study by Pascual et al. (19) evaluated 50 patients with CMI and found that 52% of them suffered from headaches, which were classified using IHS criteria (international head each society). Other symptoms are dizziness and balance problem, muscle weakness, swallowing problem, hearing loss and difficult in sleeping. (51) Coughing, sneezing, straining, or neck extension can all make the symptoms worse. (21)

2.2.2 Diagnosis

The diagnosis of CM1 usually involves a combination of physical examination, a review of medical history, and imaging tests. The physical examination may include tests for neurological problems such as muscle weakness, numbness, or tingling, as well as evaluating gait and coordination. A medical history review will ask about symptoms such as headaches, neck pain, dizziness, and balance problems, as well as any past medical conditions or surgeries. Imaging tests, such as MRI or CT scans, are used to confirm the diagnosis and determine the severity of the malformation. The diagnosis of Chiari type I malformation can be made on routine brain or cervical spine MRI by evaluation the position of the cerebellar tonsils below the foramen magnum (22)

The diagnosis is usually made when one or both tonsils are 5 mm or more below the foramen magnum, while a tonsil position of less than 3 mm below the foramen magnum is considered normal. Tonsil position between 3 to 5 mm is debatable and may be considered normal or diagnostic of CM1, depending on the criteria used. Although standard MRI sequences can easily diagnose CM1, they are not very effective in predicting symptoms, disease severity, or postoperative success. Advanced MRI techniques broadened the role of MRI in the diagnosis and evaluation of CM1, allowing for more comprehensive disease assessment (23). One of these techniques is the CSF flow studies witch in case of CM1 presents an several abnormalities:

(1) An increase diastolic and systolic velocity due to the obstruction in the foramen magnum which probably impede the CSF fluid and turn in compensatory increased velocity (24).
(2) A non-uniform flow caused by the obstruction. (23)

Other advance techniques are, cine cerebellar tonsillar motion, diffusion tensor imaging and quantitative volumetrics of the posterior fossa. (23)

2.2.3 Treatment

The severity of CM1 and the symptoms experienced by the patient determine the appropriate treatment. Regular monitoring may be recommended if no treatment is necessary in some cases. According to Ramón et al. (20), surgery is not typically required for asymptomatic patients, but it may be recommended for those with progressive posterior fossa or spinal cord signs, hydrocephalus, or syringomyelia. If the symptoms are severe enough to affect the patient's quality of life, surgery may be recommended. However, there is no consensus on the exact criteria for surgery. Chavez et al. (26) listed common indications for surgery, including cough-associated headaches that impact the quality of life, large or enlarging syrinx, and abnormal neurologic findings or myelopathy. The main goal of surgery is to alleviate pressure on the brain and spinal cord by creating more space in the back of the skull.

In order to treat the CM1 for severe symptomatic patient the treatment consist in a decompression surgery named 'Posterior fossa decompression' (PFD). This procedure consists of the remotion of a portion of the occipital bones to create more space in the SAS and restore the CSF circulation and relieve the pressure, as depicted in Figure 10. This procedure may also involve the remotion of the first vertebra of the spine (C1). (27)

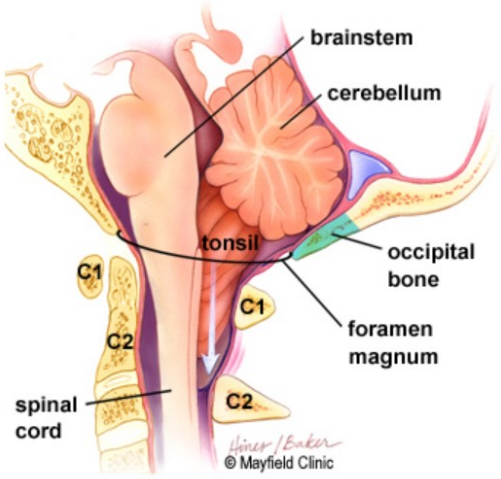

Figure 10: Posterior fossa Decompression surgery

The PFD can be carried out in combination of other type of surgery such as Duraplasty and partial tonsillar resection. The Duraplasty surgery, as represent in Figure 11, is a type of decompression surgery that involves opening the covering of the brain and spinal cord (dura mater) and inserting a patch to enlarge the space for the cerebellum.

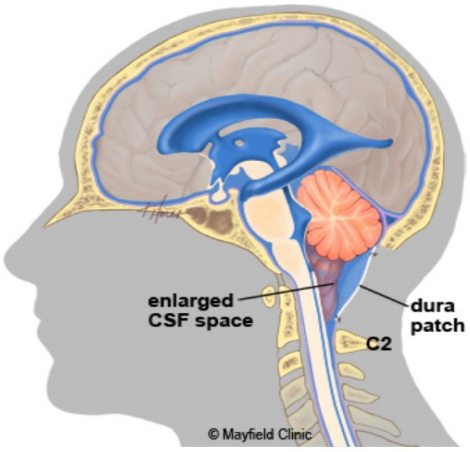

Figure 11: PDF in combination with Duraplasty surgery

Aghakhan et al. (28) examined the medical charts of 157 patients who had undergone surgical duraplasty in order to ascertain the long-term results of the procedure. According to research, there is a 90% likelihood that CM1 surgery will result in long-term stabilization or improvement. As stated by Aghakhan et al. (28), surgery should be suggested as soon as possible for patients with clearly advancing clinical symptoms

2.3 Syringomyelia

Syringomyelia is a rare neurological disorder characterized by the development of large, fluid-filled cavities called syrinxes in the spinal cord as shown in Figure 12. The estimated prevalence of this condition in Western countries is between 8.2 and 8.4 cases per 100,000 people (29). The syrinx cavity consists of a clear, colourless fluid which might originate from CSF or extracellular fluid. Typically, the syrinx develops at the cervical level of the spinal cord, but it can also extend upwards to the brain stem or downwards to the thoracic part of the spinal cord.

The presence of a syrinx puts stress on the spinal neurons, which can lead to severe motor and sensory symptoms and eventually cause irreversible neural damage. The specific clinical symptoms can vary significantly depending on the size and location of the syrinx (30).

Patients with syringomyelia often experience headaches, pain, and disruptions in motor and sensory functions. These symptoms are accompanied by pain and abnormalities in the autonomic nervous system.

Importantly, approximately two-thirds of patients with CM1 also develop syringomyelia, where fluid-filled cysts (syrinx) form in the spinal cord. The exact pathophysiology responsible for syrinx formation in patients with CM1 is still not fully understood.

Nevertheless, CM1 related syringomyelia is usually treated not acting on the syringomyelia itself, but on the original cause, CM1. The surgical procedure used is the Posterior fossa decompression with (PFDD) or without (PFD) Duraplasty. Despite this surgery usually helps to reduce syrinx volume or even completely solve it, the outcomes may be variable, and many dangerous complications may occur. Hence, there is a need for more new treatments. (30)

Better management and treatment of CM1 related syringomyelia requires a better understanding of the link between the two disorders. Several theories have been proposed to explain the formation of a syrinx in patients with CM1. All theories agree that the disruption of cerebrospinal fluid flow at the junction between the skull and the upper cervical spine plays a central role, but each theory proposes a different mechanism for syrinx formation. (31) More studies are necessary to gain a deeper understanding of cerebrospinal fluid dynamics and the mechanical behaviour of neural soft tissues since it is believed that biomechanical factors contribute the syrinx formation. By using both experimental and computational biomechanical models, we can investigate these aspects in detail.

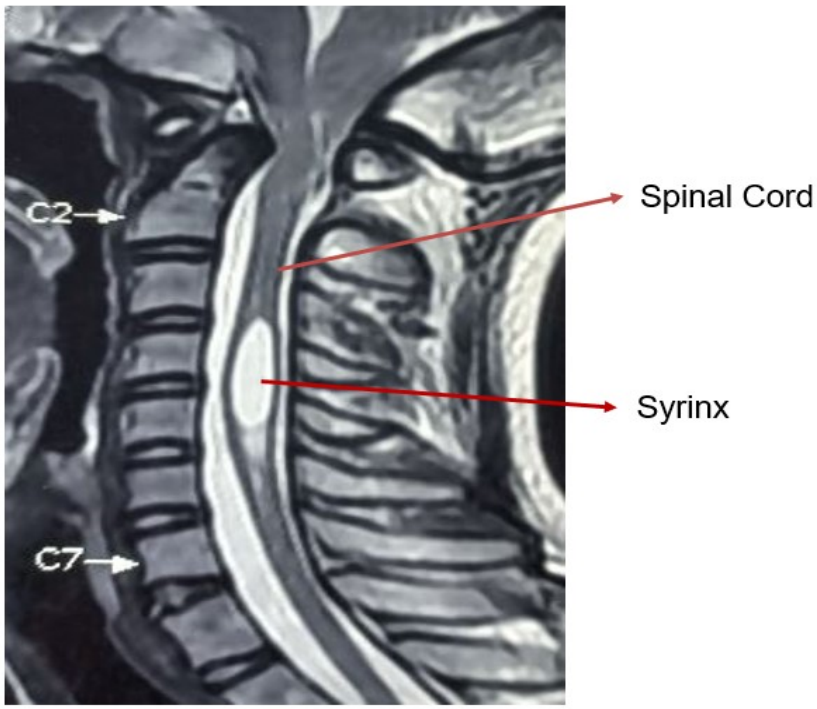

Figure 12: MRI of a patient with CMI related syringomyelia

Chapter 3

3 STATE OF THE ART

3.1 Introduction

Modeling the CM1 has always posed a challenge for researchers due to several issues. Firstly, the low occurrence of the pathology has made it difficult to gain insights through clinical observation. (32)

Moreover, collecting in vivo data is invasive and the required measurement sites are not easily accessible.

To overcame these difficulties in vitro model granted to have a better insight to the CSF pressure and velocities. Nevertheless, this model has the strong limitation to accurately reproduce both the geometry and the boundary conditions.

Recently, advances have been made to measure in vivo flow and velocities with the use of the PCMRI

PCMRI has enabled the simultaneous in vivo measurement of velocities in through-plane and in-plane directions and allows for higher spatial-temporal resolution compared with conventional 2D PCMRI methods within a clinically feasible time-frame. Researchers have applied 4D Flow to investigate in vivo CSF velocity magnitudes and distribution in the spinal SAS (33). However, MRI measurements are limited by the spatial and temporal resolution of the scanning sequence. Also, the monitoring of the pressure is still invasive and difficult to carry out.

Consequently, numerical tools have played a crucial role in overcoming the lack of patient measurement Specifically, computational models have enabled researchers to gain an understanding of complex geometric pressure and velocity distributions. Two main simulation approaches for investigating CSF are: Computational Fluid Dynamics (CFD) and Fluid-Structure Interaction (FSI). CFD modeling is based on the principles of mass, momentum, and energy conservation. The Navier-Stokes equations are employed to describe momentum conservation in Newtonian fluids, while the continuity equation is used to depict mass conservation. The FSI approach allows the modeling of a multi-physics problem, in this specific case coupling Structural Mechanics and Fluid Mechanics. The coupling of physical laws of Fluid Mechanics and Solid Mechanics describes the interactions between one or more deformable/moving structures and a fluid flowing around or inside the structure by Continuum Mechanics. This computational technique allows for the consideration of interactions between the fluid and deformable walls, surpassing the limitation of CFD, which assumes rigid walls. These two methodologies will be further elaborated on in the subsequent sections, with a focus on CM1 modeling. (34)

3.2 Modelling of Cerebral Spinal Fluid (CSF)

It is well-established that disturbances in CSF flow and alterations in brain tissue mechanics play a crucial role in various pathologies, including CM1, Hydrocephalus, and Alzheimer's disease (35). Consequently, CFD and

FSI models have gained widespread usage in investigating the pressure and velocity fields, as well as the interaction between brain tissue under both pathological and physiological conditions.

3.2.1 Computational model

Three-dimensional CFD models are useful for subject-specific computations of CSF dynamics based on medical image data because they may give spatial and temporally resolved information on flow, pressure, and mass transfer. The emergence of commercial magnetic resonance imaging (MRI) systems contributed to advances in understanding CSF space anatomy and cerebrospinal fluid dynamics physiology, which made it possible to obtain anatomically accurate descriptions of the CSF spaces and use noninvasive measurements of fluid flow and velocities as boundary conditions (32).

Because of the invasive nature of intracranial pressure measurements, only velocity, flow rate, or similar BC may be given in a subject-specific manner, but pressure or impedance BCs that are necessary to achieve mass conservation in non-compliant domains are generic based on generalized lower-order models. (34) (36)

One of the stronger limitations of the CFD model is the assumption of a rigid wall. With this assumption is not possible to take into account the compliance effects arising from the deformability of the tissue surrounding the space of simulation. To tackle this problem the FSI approach is necessary, but requires a deep understanding of model brain tissue and high computational costs.

PCMRI has enabled the simultaneous measurement of velocities in through-plane and in-plane directions and allows for higher spatial-temporal resolution compared with conventional 2D PCMRI methods within a clinically feasible time-frame. Researchers have applied 4D Flow to investigate in vivo CSF velocity magnitudes and distribution in the spinal SAS (33). Unfortunately, the monitoring of the pressure is still invasive and difficult to carry out.

Initially, due to the computational resources required, most studies have focused on analyzing small portions of the geometry. Gupta et al. (37) focused only in the inferior cranial space, the superior SAS and the fourth ventricles and Clarke et al. (38) focused solely on the spinal SAS from the second vertebral (C2) to the fifth vertebral (C5). These models provided insight into the local effects without providing a system wide response.

Gupta et al (39) introduced a transient 3D model of CSF circulation in cranial SAS using a finite element approach with CFD. To account for the effect of the trabecular morphology they treated the cranial SAS as a porous medium. In terms of the inlet boundary conditions, the study utilized patient-specific MRI measurements of velocities in the pontine and cerebello medullary cisterns over one cardiac cycle. The only outflow pathway considered was absorption through the arachnoid granulation with a constant outlet pressure of 3.15 mmHg. Importantly, this study neglected the cerebral ventricles of the CSF production and focused solely on the arachnoid granulation drainage pathway, which prevents a comprehensive evaluation

of the necessary pressure gradients for understanding diseases. Additionally, the study only focused on brain circulation and neglected the spinal cord.

The first patient-specific simulation throughout all the CNS has been carried out by Sweetman et al. (40). This model accounted for CSF production, reabsorption, and the influence of pulsatile motion. CSF production was assumed to be constant and originating from the lateral ventricles at a rate of 0.4 mL/min, while reabsorption was considered to occur only through the arachnoid villi with a constant pressure of 500 Pa. To incorporate pulsatile flow, the model included moving boundaries based on in vivo measurements near the lateral ventricles. The study also incorporated spinal compliance by implementing a patient-specific finite element model of the dura mater. The deformable membrane was modeled as a neo-Hookean material, specifically a hyperplastic model with a Poisson ratio of 0.5 and Young's modulus of 12kPa. The modelled CSF velocities corresponded well with CSF velocities measured in vivo
, despite assuming constant CSF production and considering only one drainage pathway. Furthermore, there was no experimental evidence provided for the material properties utilized in the model. Fillingham al (25) developed a whole-brain, patient-specific CFD simulation of CSF flow in the cranial cavity introducing more physiological flow boundary conditions. The study considers a patient-specific, 3D rigid wall CFD simulation of the CSF-filled spaces in the brain, using phase contrast magnetic resonance imaging to measure all the flow rates in and the out of the cranial cavity. The boundary of the computational domain was split into six regions Figure 13:The ventricle walls; choroid plexus; foramen magnum; the surface of the cerebrum; the arachnoid granulations; and the walls of the brainstem, cerebellum, and dura mater.

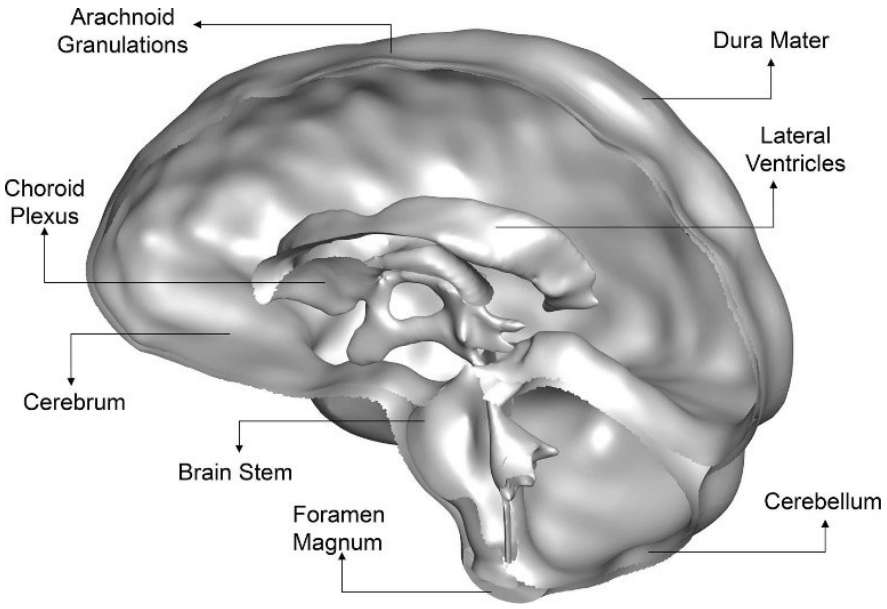

Figure 13: Cross-sectional view of computational domain with labelled boundaries. (41)

The boundary conditions are based on the PC-MRI. The researchers avoid the assumption of the previous studies regarding the constant production of the choroid plexus by reconstructing a specific waveform for CSF generation based on MRI-based measurements of CSF flux across the cerebral aqueduct and blood flow

at the Internal Carotid Artery. Regarding the outlet boundary condition, the model considers only the arachnoid granulation, which are implemented as a time-dependent flow outlet using the principle of mass conservation.

The time-averaged flow at the arachnoid granulations is equal to the combined time-averaged flow entering the cranial cavity at the foramen magnum and the time-averaged flow across the cerebral. Then, they shift and scale the waveform of the blood flow measured at the internal jugular vein.

Since is a CFD study with rigid walls the pulsatile flow is taken into account both in the cerebral cortex and the ventricles wall by using an artificial volume flux term. An overview of the boundary condition that has been used is depicted in Figure 14.

The work presents a quantitatively validated whole-brain simulation of CSF flow for a single healthy subject. Nevertheless, the model only allows calculation of the relative pressure field and the simulation cannot calculate absolute cranial pressure, due to the lack of a reference value that requires an invasive procedure. Furthermore, only one drainage path has been highlighted and two artificial terms were added to represent the brain tissue deformation with a zero net flow over one cardiac cycle.

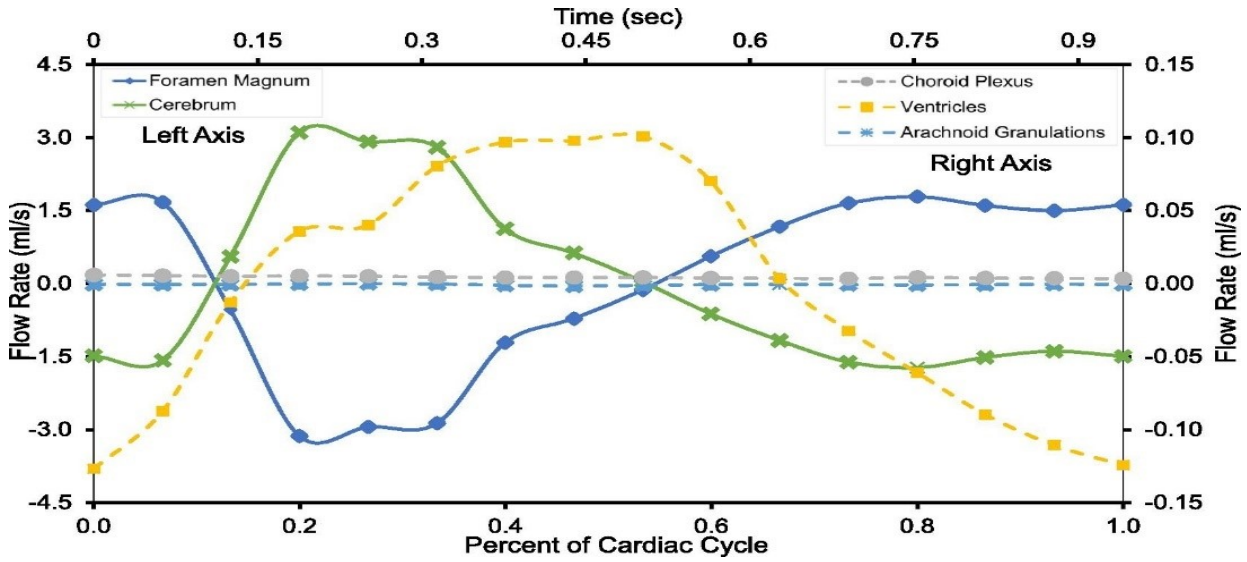

Figure 14: Boundary conditions prescribed in the computational model calculated from PCMRI measurement (41)

The previous CFD models did not consider the effect of CSF compliance and don't take into account the distribution of compliance across the cranial and spinal compartments. Vandenbulcke et al (23) developed a computational model that can predict CSF pressures and velocities under various physiological conditions. To accomplish this goal, a three-dimensional CFD model was constructed that allows for the simulation of absolute pressures and velocities throughout the CSF space. This study included in the model not only the adsorption pathway of the arachnoid villi but also the secretion into the lymphatic, interstitium and spinal venous systems resulting in 4 different outlets. To consider the effects of both absorption resistance and CSF

compliance, windkessel boundary conditions are applied at each outlet. Specifically, a 2-element windkessel model is used, which is an electrical analogy consisting of resistance and compliance in parallel.

The study also takes into account the changes in arterial and venous volumes and intracranial and spinal compliance. At lateral ventricles the CSF production is taken into account as a constant production. To consider the cardiac pulsation two sinusoidal waveforms with both 1Hz frequency and zero net flow have been added in the region depicted in figure 11. Finally, a sinusoidal waveform with frequency 0.2 Hz is used to model the respiratory effect. The inlet boundary conditions that have been used by Vandenbulcke et al. (35) are summarized in Figure 15

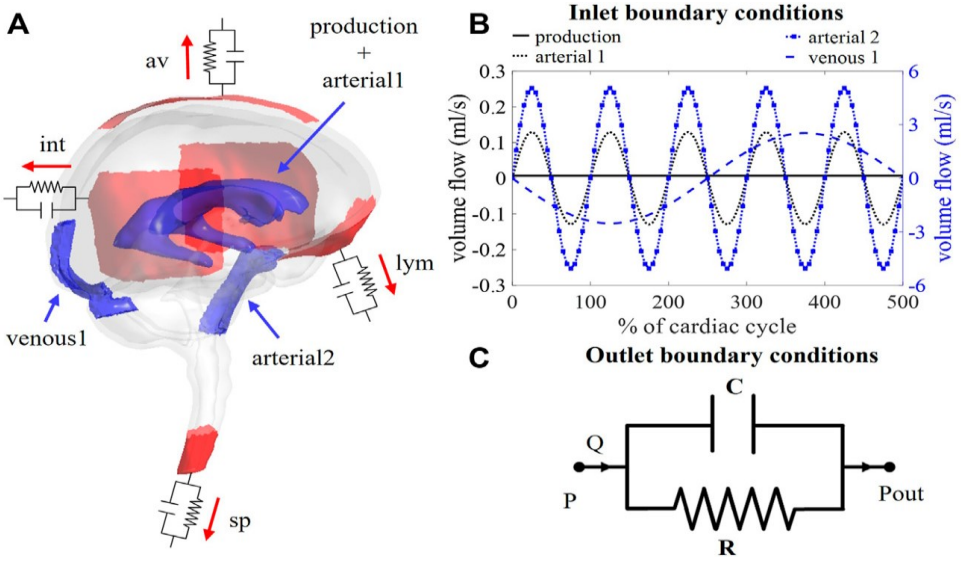

Figure 15: (A) Visualization of boundary conditions in the 3D model. (B) Graph containing the waveforms of the four different inlet boundary conditions depicted in (A). (C) Electrical circuit representing the 2-element windkessel model

The researchers simulate 25 cardiac cycles considering the CSF as an incompressible Newtonian fluid with the same proprieties of water. The motion of the fluid is governed by the continuity and Navier-Stokes equations.

This study, as mentioned before, allows to obtain absolute CSF pressures and velocities simultaneously through implementation of absorption resistance and compliance while previous CFD models do not provide absolute intracranial pressures. One of the limitations of the model is that model is validated by comparing it to literature data although the literature data does not account for respiratory effects or normal physiological pressures. Moreover, the model includes simplifications such as simplified 3D geometry and simplified inlet boundary conditions. Nevertheless, the model is a proof of concept that proper boundary conditions can yield pressures and velocities within the physiological range.

Although windkessel boundary conditions allow modelling intracranial compliance, using an FSI modelling approach is more accurate to account for compliance effects arising from the deformability of the tissues surrounding the simulated 3D fluid spaces.

3.2.4 Validation -In vitro modelling

In vitro measurements can be useful to get some data that may be hard to get in vivo models. The ability to measure the flow and pressure of CSF in living organisms is limited. However, computer modeling can be used to study parameters, while in vitro modeling is necessary to test and evaluate therapeutic interventions related to fluid disorders. Benninghaus et al. (42) developed an enhanced in vitro model of the CSF dynamics, which includes a ventricular system connected to the cranial and spinal subarachnoid spaces, compliance chambers, and sensors to monitor CSF dynamics. The model has two compliance chambers that absorb the blood flow from a cam plate unit, allowing for the creation of personalized flow dynamics for each patient (Figure 16). To monitor the CSF dynamics, the model uses three pressure sensors in the cranial region and an ultrasound flow meter in the spinal region. The researchers compared the in vitro measurements of spinal flow to the PC-MRI cervical flow data from nine healthy young people and compared the pressure measurements to reported values of intracranial pressure (ICP) to validate the new in vitro model. The model was found to accurately simulate CSF flow and pressure dynamics in the supine position, but adjustments would be needed for upright positions due to changes in compliance values and divisions.

The limitation of the model is the static compliance that has been considered while human tissue proprieties. Moreover, the spinal cord wasn't included in the model.

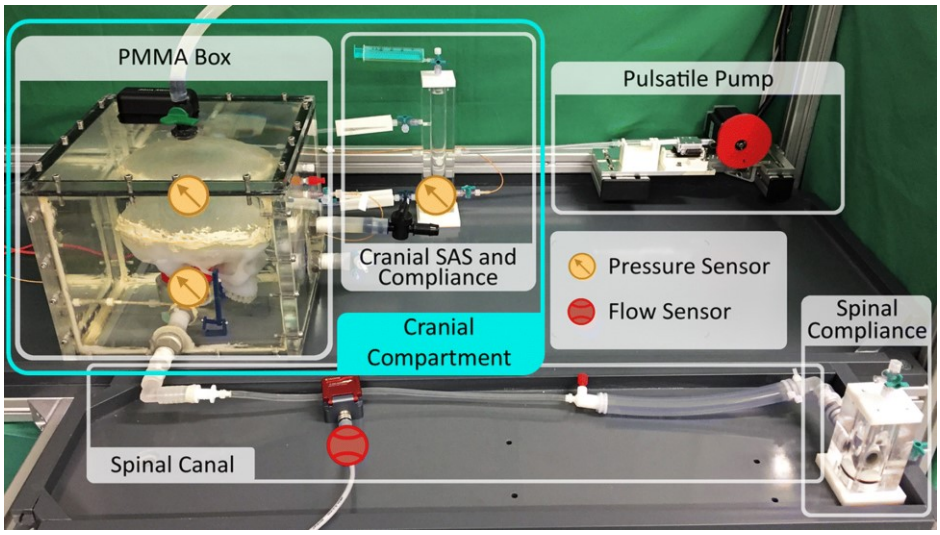

Figure 16: Set up experiment used by Benninghouse et al. (42)

In vitro models, are also utilized to validate the accuracy of CFD simulations. In this case, the in vitro model involves creating a 3D-printed replica of the patient's specific anatomy and reproducing the physiological CSF flow using a hydraulic pump or a drainage system.

Khani et al. (43)(44) conducted a study to compare the blood removal efficiency of a catheter-based CSF filtration system with a lumbar drain. To accomplish this, they developed a comprehensive CFD model of the CSF system. The researchers implemented a constant CSF production rate in the lateral ventricles and applied zero pressure at the cranial opening. They incorporated a drainage rate corresponding to the filtration

system. To account for pulsatility resulting from heartbeats and respiration, an oscillatory velocity inlet boundary condition was defined at the lower end of the model. This condition was derived from a PCMRI measurement taken at the vertebral level of C2 and C3.

To validate the obtained results, an in vitro model was constructed using a 3D printer to replicate the same geometry as the CFD model mentioned earlier. The same boundary conditions were applied using an oscillatory pump, inducing the desired oscillatory movement in the system.

However, while these in vitro models are valuable for gaining insights into the problem and can serve as a tool to validate the model, they have significant limitations in accurately representing both the geometry and the boundary conditions.

3.3 Modelling Chiari 1 Malformation

It is widely accepted that disrupted fluid movement plays a significant role in the development of CM1 and syringomyelia. However, the exact mechanism underlying syringomyelia and its potential correlation with CM1 remains unknown. Due to the difficulties to obtain in vivo measure, both in vitro model and numerical methods are essential for gaining a better understanding of CSF flow in the SAS.

In the literature, various numerical models, including 2D, and CFD models, have been employed to investigate how CM1 affects CSF flow in terms of pressure and velocity with patient-specific and simplified geometry. Furthermore, to model the CSF flow compliance due to tissue displacement, it is necessary to consider the interaction between CNS tissue and brain tissue, requiring FSI models. These models can be elastic or viscoelastic FSI simulations that account for the behavior of solid structures. They are useful for studying the propagation of pressure waves, but the boundary between the two domains is typically treated as impermeable, limiting our understanding of syrinx formation.

To address the issue of fluid accumulation in the spinal cord, a poroelasticity formulation is necessary. Currently, only 2D FSI models with a poroelasticity formulation have been found in the literature.

In the following sections, I will discuss the different numerical models in more detail.

3.3.1 In vitro model

As before mentioned for the full CSF model, acquiring data in vivo is quite invasive. In order to overcome these difficulties in vitro model can be used to obtain data that in vivo are difficult to gather.

Martin et al. (45) create a mechanical in vitro model to investigate pressure simulating the different situations of stenosis and syringomyelia. The researchers simulated four conditions: the stenosis and the syrinx, the stenosis without the syrinx, the stenosis located cranially and the syrinx (to mimic CM1,) and the only syrinx. The experimental setup is represented in the Figure 17, the total length of the model is 48cm with a pressure

sensor every 4cm. Regarding the boundary conditions, an MRI waveform at the C2 level was measured in a patient and replicated with a computer-controlled pump at the cranial level. To account for the compliance due to the deformation of the spinal cord a material with 500Kpa has been chosen.

The researchers found that the stenosis in general act to increase the CSF pressure in the SAS and the majority of pressure change happen near the obstruction with a greater influence if the syrinx is present.

In the experimental simulation of Chiari malformation with stenosis, the pressure difference observed between the syrinx and the spinal SAS cannot be attributed to the presence of an obstruction, but rather to a valve mechanism. During the systolic phase, the syrinx is compressed, resulting in reduced resistance CSF flow. On the other hand, during the onset of the diastolic phase, the spinal cord is pulled outward, creating significant resistance to the CSF flow returning to the cranium. As a result, there is a decrease in pressure between the caudal and cranial regions of the stenosis.

As mentioned earlier in the previous chapter 2, in vitro models are designed to conduct experiments that closely resemble in vivo conditions, but they often require simplifications in terms of geometry and boundary conditions. In order to overcome these limitations, numerical simulations are necessary.

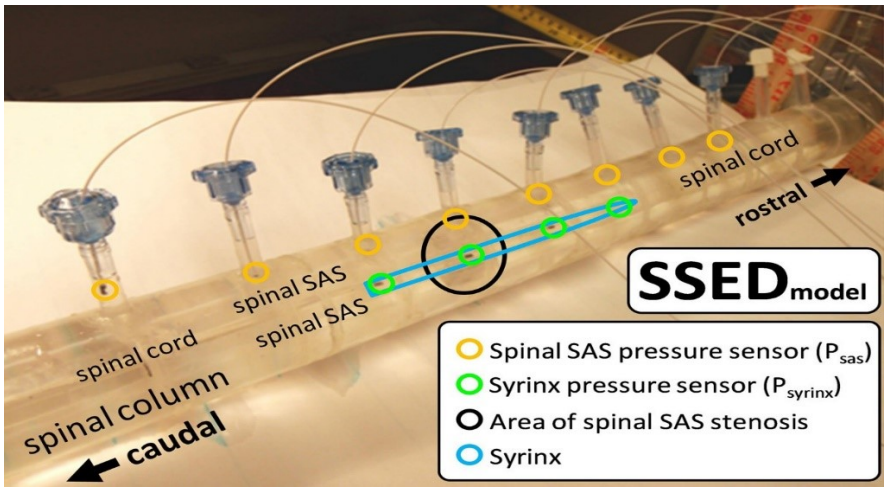

Figure 17: Picture of the model used by Martin et al (45)

3.3.2 CFD model

There is a consensus that disrupted fluid movement is a major factor in the development of CM1 and syrinx. This is why CFD models are the most commonly utilized method for investigating this condition. CFD models have been employed to examine how CMI affects the flow of cerebrospinal fluid in pressure and velocity.

Støverud et al (46) developed a simplified 3d model with the same geometry as the SAS to evaluate if the Bernoulli principle can accurately predict the pressure drop in the subarachnoid space. They studied the behaviours of an oscillatory flow with different degrees in the obstruction respectively 60% 75% and 85%. Pressure and velocities have been calculated using the Navier-Stokes equation in a constant and oscillatory

flow. Increasing the obstruction of CSF flow in the cervical spinal canal increases the pressure gradients and velocities, as shows in Figure 18. The pressure gradient with the increase in the amount of obstruction presents a steeper variation pressure gradient.

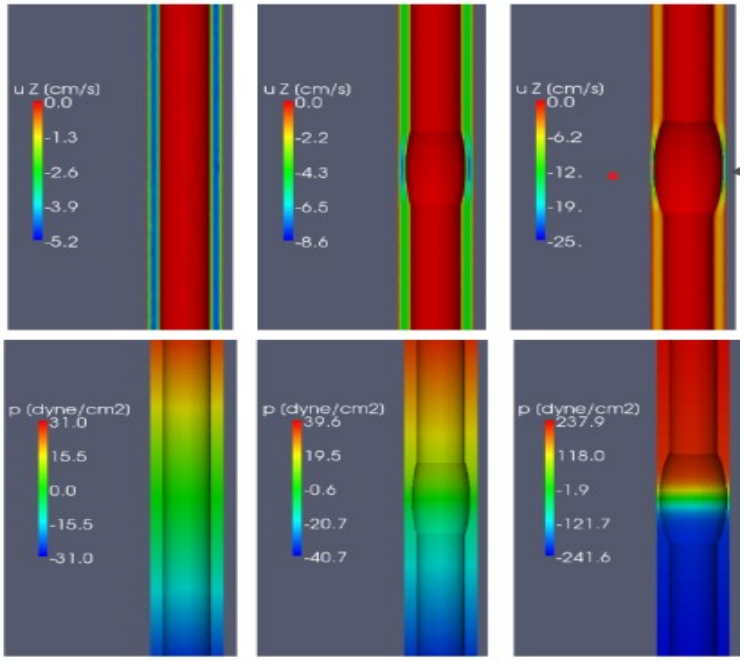

Figure 18: Velocities and pressure profile with the different level of obstruction determine by Støverud et al. (46)

Moreover, the researchers find that the Bernoulli principle does not explain correctly the pressure drop in the SAS and underestimate at least by a factor of 2 the pressure drops.

The model mentioned presents a simplified geometry. This is a limitation of the study since the geometry does not represent accurately the patient-specific geometry.

Clarke et al. (47) used a patient-specific geometry in CFD model to study the origin of syringomyelia and performed a comparison between CSF flux. The study compared three patient-specific geometry of the spinal SAS: one derived from a healthy patient, one from a patient with CM1 and one with CM1 and syringomyelia. MRI scans of three individuals were used to gather model geometries and the data on CSF flow rates were calculated by fitting a Fourier function to the data from PC-MRI scans of a larger group of patients. Both upper and lower boundary conditions were computed in this manner. The result shows an increase in the gradient of both pressure and velocities and a slight increase in peak pressure in the patient with syringomyelia. The CFD velocities demonstrated a strong agreement with MRI-measured velocities, with no noteworthy variance in peak values for any of the three scenarios. Moreover, these simulations indicated that the magnitude of pressure was significantly affected by the anatomy at the point where the cranium meets the cervical spine and that it's difficult to predict the pressure gradient in vivo due to the difficult to place pressure sensor. One of the most significant limitations of this study is the fact that the three patient

specific geometries were used but the boundary conditions have been obtained from a group of patients and this profile does not fit in a patient- specific manner.

Most of the patient-specific 3d studies are focusing only on the spinal circulation of CSF due to the high computational cost. Støverud et al. (48) led a study to extend the previous modelling by including the cerebellum medullary cistern, pontine cistern, and 4th ventricle in addition to the cervical SAS as show in Figure 19. The simulation considers three cardiac cycles. The study included one healthy control, Con1, and two patients with Chiari I malformation, P1 and P2. Patient-specific flow conditions in the aqueduct and the cervical SAS were used. Two patients with the Chiari malformation and one control were modelled.

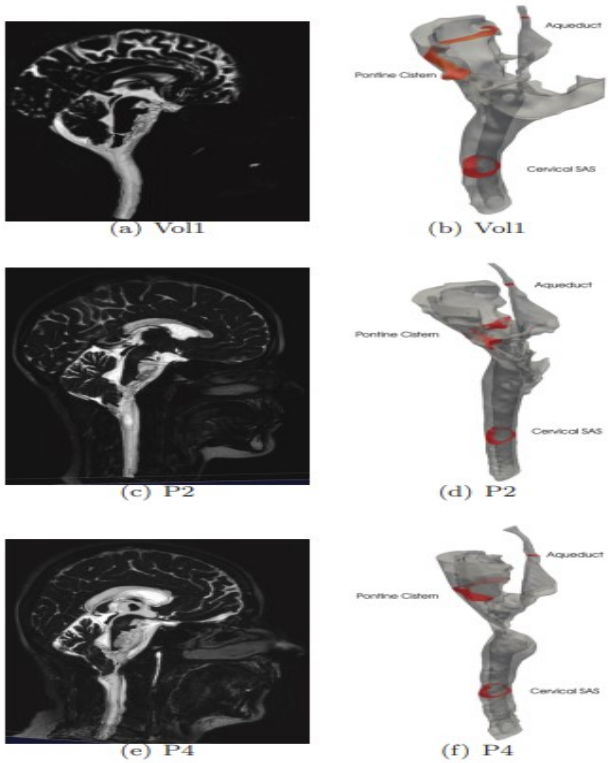

Figure 19: Sagittal MRIs and corresponding level set surfaces. (48)

Patient-specific flow conditions in the aqueduct and the cervical SAS were used. The flow in the pontine or cerebello medullary cisterns was not directly measured, so the principle of mass conservation was used to create velocity profiles. In the control case, the cerebellomedullary cistern was the only one present. To create the velocity profiles, the flux through the aqueduct was subtracted from the flux at the foramen magnum, and the remaining flux was divided into two areas and scaled by the areas. The assumption of a no-slip boundary condition was made at the SAS boundaries. The results indicated a significant increase in maximal flow velocities in Chiari patients, with the values ranging from 5 times greater in P1 to 14.8 times greater in P2 when compared to Con1 at the Foramen Magnum level. The maximal velocities in the Sas varied by a factor of 2.3, while the maximal flow in the aqueduct varied by a factor of 3.5. The pressure drop from the pontine cistern to the cervical SAS was comparable in Con1 and P1, but as twice as high in P2. The

pressure drops between the aqueduct and the cervical SAS ranged by a factor of 9.4, with P1 exhibiting the smallest pressure jump, while P2 and Con1 differed by only a factor of 1.6. (Figure 20)

One conclusion drawn from the study is that resistance and peak velocities serve as valuable indicators for detecting obstructions caused by cerebellar tonsil herniation. Additionally, increased pressure drops across the foramen magnum are indicative of the severity of the obstruction.

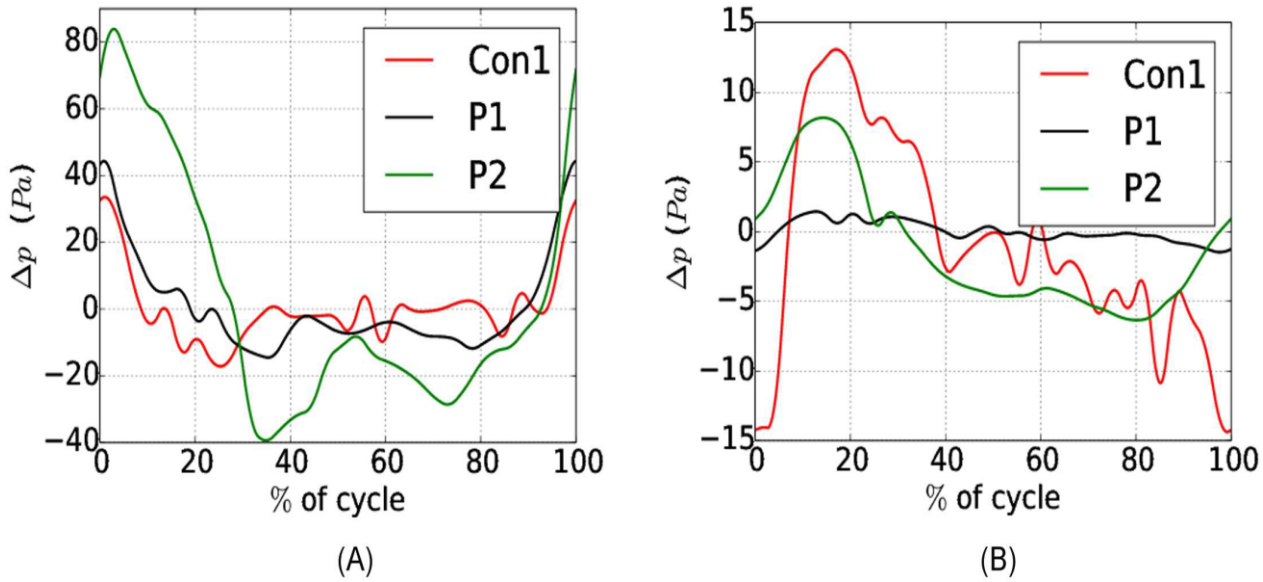

Figure 20: Pressure drops between (A) the cervical SAS (CS) and the pontine cistern (PC) and (B) between the Aqueduct (Aq) and the pontine cistern (PC) during the hearth cycle (28)

3.3.3 FSI model of CM1

FSI has been used to take into account the tissue around the SAS. The FSI modeling is challenging because the solid deformed boundaries change the fluid flow and the fluid deforms the solid boundaries simultaneously. Due to the high computational cost of partitioned FSI, the central nervous system needs to be simplified.

Bertram et al. (49)(50) developed the FSI model to investigate the interaction between CSF flow, pressure distribution in the SAS, and stress and deformation in the dura and spinal cord. The CSF was modelled as a viscous incompressible fluid using the Navier-Stokes equation, while the dura and spinal cord were modelled as isotropic linear elastic materials. They specifically focused on studying the propagation of pressure waves along the spinal cord. The model was later extended to incorporate viscoelasticity and to examine the impact of a syrinx and SAS obstruction due various loading such as coughing.

As mentioned in the introduction to address the issue of fluid accumulation in the spinal cord, a poroelastic formulation is required. Currently, only 2D FSI models with a Poroelastic formulation have been reported in the literature. In the subsequent sections, I will provide a more detailed discussion of the different numerical poroelastic models.

3.3.4 Poro-elastic Modelling

As mentioned earlier, impermeable FSI models can take into account the impact of solid materials on fluid, but they do not account for the permeability of solids. However, we now know that a significant portion of the volume of the brain and spinal cord consists of interstitial fluid, which is crucial to consider when assessing fluid accumulation in the spinal cord. Poroelastic models address this by modeling a solid porous matrix and the incompressible flow of fluid through the matrix's pores. In this approach, the solid phase is made up of neurons, glial cells, and vasculature, which are all saturated with interstitial fluid. The interstitial space is highly complex, with nanoscale pore sizes, and accounts for 20% of the total volume of the spinal cord, whereas the vasculature occupies only 3% (51). Using poroelasticity models allows us to simultaneously consider the mechanical interaction between fluid and solid, fluid flow, and fluid accumulation inside the porous material.

To investigate the development of syringomyelia, Støverud et al. (52) carried out a simulation considering the spinal cord as a cylindrical poroelastic structure. The simulation aimed to quantify the deformation and fluid movement in the spinal cord by applying a prescribed pressure under different conditions: healthy conditions and the CM1, which involved an increased and steeper pressure profile as found by the same author in the CFD study mentioned (46). The spinal cord presents the same mechanical linear elastic proprieties in the cylinder. To mimic the central canal a higher permeability was assigned to the central canal of the spinal cord model. The researcher discovered that the pressure gradients in the SAS move fluid in the spinal cord abnormal CSF gradients lead to the accumulation of fluid within and adjacent to the spinal cord central canal.

Bertram et al. (53) developed a more complex poroelastic model of the spinal cord that included both the syrinx and CM1 with the geometry shown in Figure 21. Their focus was on syringomyelia with adjacent stenosis in the subarachnoid space, and their model incorporated a syrinx and stenosis aligned with it. The spinal cord and dura were constrained at their ends. Using a pressure wave with a 500Pa amplitude applied to the cranial end of the subarachnoid space, consistent with their previous non-porous model, Bertram et al. (53) theorized that the syrinx grows due to CSF exchange with the spinal subarachnoid space.

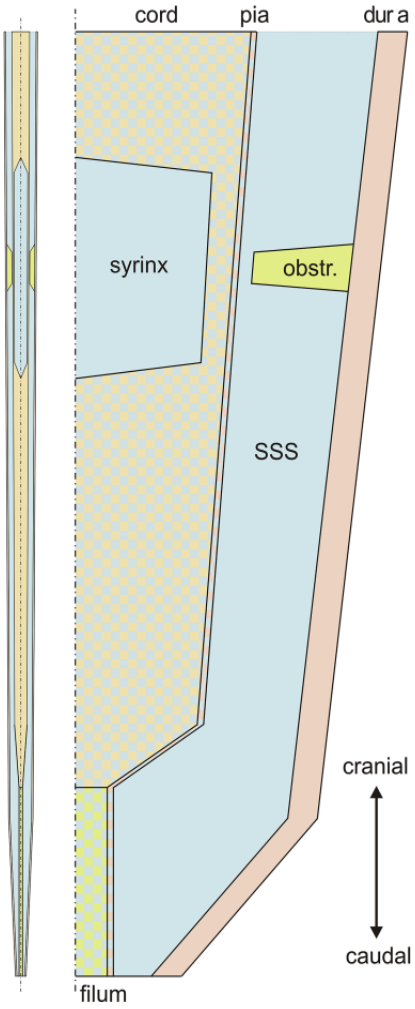

Figure 21: Sketch of the geometry of the model where L/D=30 and D=20mm (30)

When comparing the results of the model include poroelasticity with the one of the non-porous model (61), they found negligible differences in the cord displacement and that the pressure peaks in the SAS caudally to the stenosis were slightly increased. Moreover, they observed a certain fluid exchange between the porous tissues and the SAS, which led to a general mechanism of fluid movement between the syrinx and the SAS. The porous tissue surrounding the syrinx presented a slight swelling due to the incoming fluid. All these changes in syrinx volume, fluid movement, and tissue swelling were evaluated in a time scale very short compared to the syrinx growth in patients.

3.3.5 Proprieties of Spinal Cord tissue

The precision of the output of any biological system's computational model is reliant on the accuracy of the input parameters. As mathematical models of the spinal cord are becoming more prevalent, more efforts are being made to define the mechanical characteristics of spinal cord tissue.

The equations of linear poroelasticity describe a two-compartment material, defined by the solid compartment and the pore fluid. A summary of the material parameters required to fully describe a linear poroelastic material can be seen in Table 1.

Symbol	Parameters	Unit	Literature Values
k	Permeability	m^2	1 × 10−13 Shahim et al. (55)
ρ	Density	$\frac{Kg}{m^3}$	1000 kg/m^3
E	Young modulus	MPa	40.12 ± 6.90 Karimi et al. (56)
v	Poisson Ratio	Pa s	0.5 Bertram et al (53)
ϵ	Porosity	/	0.3 Bertram et al (53)

Table 1: Proprieties of spinal tissue and literature reported values

As already mentioned in Chapter 1, the spinal cord runs from the brainstem to the lumbar spine, connecting the brain to the rest of the body. Its structure is not uniform, consisting of white matter axons surrounding a grey matter core containing nerve cell bodies arranged in a butterfly shape. Due to this non-uniform structure, it is expected that the spinal cord would exhibit anisotropic behaviour, but this has not been experimentally confirmed. Similar to the brain, the spinal cord is covered by meningeal layers and surrounded by CSF with a network of blood vessels. Additionally, nerve roots emerge from the spinal cord and connect to other parts of the body, anchoring the spinal cord in place.

Reported spinal cord Young Modulus values span several orders of magnitude and are influenced by the technique used to measure it (57). Spinal cord Young Modulus values are often obtained using either tensile testing, compression testing or indentation. Tensile testing largely yields higher Young Modulus values than compression and indentation, as the sample length for compression and indentation is usually much smaller than for tensile testing. The values range from 70 to 1400000 Pa, demonstrating the extent of the spinal cord's strain stiffening behaviour, as well as the influence of different testing techniques, variations in tissue types such as grey matter, white matter, and pia mater, and the potential effects of age or species on the elastic properties of the spinal cord.

The study carried out the study by Karimi (56) wants experimentally measure the mechanical properties of the human cervical spinal cord of 24 isolated fresh samples under unconfined compressive loading at a relatively low strain rate. The stress-strain data revealed the elastic modulus and maximum/failure stress of

40.12 ± 6.90 and 62.26± 5.02 kPa, respectively. These values reported consider also the effect of the Pia Mater.

The pia mater firmly covers the spinal cord and has a 460 higher elastic modulus (58); it, therefore, provides a constraint on the spinal cord surface. It prevents elongation of the circumference and produces a large strain energy that is responsible for shape restoration following decompression.

Moreover, another problem is that most of the Young Modulus testing on the spinal cord has been conducted on ex vivo samples, which may impact the mechanical response of the tissue. When the spinal cord is removed from the spinal canal, it loses support from the surrounding CSF, and the low density and YM of spinal cord tissue cause it to lose its shape. As a result, tests carried out on the spinal cord may produce different effective elasticity results when it is removed from the CSF.

For the poroelastic model present in the literature the elastic modulus has to take into account the solid compartment only. The poroelastic cord model by of Bertram et al. (53) and Støverud et al. (59) use a value of 5000 Pa.

Regarding the Poisson Ration, the main compartment of the spinal cord tissue is nearly incompressible due to the high content of water. Consequently, Støverud (59) al used a Poisson ratio of 0.5. Bertram et al. (53) used a lower value of 0.4, this value is validated for large tissue samples with a great number of cells.

Chapter 4

4 OBJECTIVES

4.1 Aim of the Thesis

As mentioned earlier, to the best of my knowledge there is no existing literature on artificial 3D obstructions that model CM1 specifically located in the region of the foramen magnum. The primary objective of this thesis is to provide an understanding of the effects of a 3D obstruction in the vicinity of the obstruction. The artificial 3D herniation has the advantage to be the same in the different simulation leading to not impact of the difference in person specific geometry between healthy and with obstruction which can lead to a bigger impact that the obstruction itself. The analysis was conducted using both the CFD approach and the FSI approach, with the spinal cord modelled as a poroelastic material.

To begin, a comprehensive CSF CFD model was developed to investigate the overall circulation, including different drainage pathways such as arachnoid granulation and lymphatic drainage. However, the compliance resulting from cerebral brain tissue was not taken into account in this initial model.

Following that, a section of the full geometry is used to perform both a CFD and an FSI study incorporating an artificial 3D obstruction that models the CM1. The purpose was to compare the two different approaches, the CFD and the FSI evaluating the relative impact of the obstruction on pressure and velocities and also in the FSI approach highlight the mechanical behaviour of the spinal cord and the fluid exchange between the spinal SAS and the spinal cord.

The Table 2 depicted an overview of all the simulation that has been carried out to face this purpose.

	Technique	*Domain*	*Geometry*	*Proprieties*
Simulation 1	CFD	FULL GEOMETRY	Healthy Condition	Without PIA
Simulation 2	CFD	Section of full geometry	Healthy Condition	Without PIA
Simulation 3	CFD	Section of full geometry	CM1	Without PIA
Simulation 4	FSI	Section of full geometry	Healthy Condition	Without PIA
Simulation 5	FSI	Section of full geometry	Healthy Condition	With PIA
Simulation 6	FSI	Section of full geometry	CM1	With PIA

Table 2: Simulations that have been carried out in the thesis, highlight the techniques, the domains, the geometry and the proprieties that have been used.

Chapter 5

5 STUDY OF FULL CSF CIRCULATION

5.1 Introduction

The purpose of this chapter is to evaluate whether it is feasible to simulate CSF flow in the complex cranial and upper spinal CSF compartments using the numerical software COMSOL Multiphysics (COMSOL Inc). The presented 3D in silico model takes into account the continuous production of CSF from the lateral ventricles, as well as the drainage pathways involving the arachnoid villi and the lymphatic system. Additionally, the model incorporates pulsations caused by respiratory and cardiac cycles.

5.2 Material and Methods

A CFD model of the CSF was created using the software COMSOL MULTYPHYSICS 6.1 and was based on the CFD model that was previously developed in Fluent (Ansys Inc.) at the research group BioMMedA. The following steps were followed: 1) Importing the geometry, 2) Generating the mesh, 3) Implementing the boundary conditions and physics, and 4) Setting up the numerical solver.

5.2.1 Geometry

The 3D geometry used in this study, Figure 22, is the same as the one employed by Vandenbulcke et al. (35), which was derived from a T2 MRI image of a patient with CM1 malformation using Mimics 21.0 (Materialise, Leuven). The image data were obtained from Ghent University Hospital using a 3T Prima system (Siemens, München). In this geometry, a uniform thickness was assigned to the cranial SAS and the original blockage of CSF flow associated with Chiari type 1 malformation was resolved (minimum SAS thickness of 4 mm at the level of the foramen magnum).

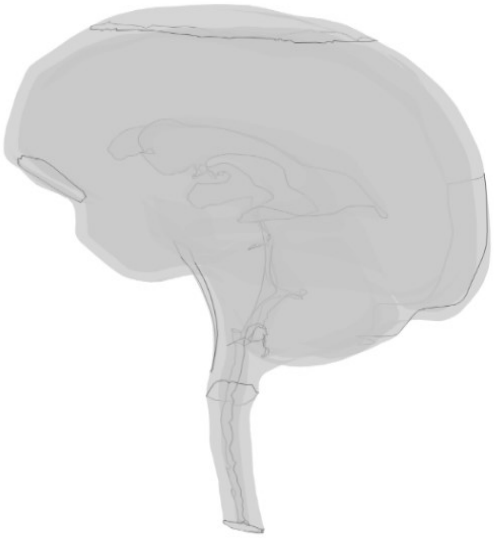

Figure 22: Geometry of the full SAS space that has been used for the simulation. Internally, the pia mater and externally the Dura Mater

5.2.2 Generation of the mesh

The mesh construction was carried out using the built-in automated tool provided in COMSOL Multiphysics (COMSOL Inc.), which involved selecting different element sizes such as "Coarser," "Coarse," "Normal," and "Fine." This tool automatically generated the mesh based on the geometry and the physics relevant to the simulation, which in this case is 'Laminar flow'. The statistics of the four meshes are presented in Table 3.

	COASER MESH	COARSE MESH	NORMAL MESH	FINE MESH
Number of elements	29.952	50.109	107.686	318.186
Minimum quality	0.008021	0.01979	0.01862	0.09192
Average quality	0.5766	0.6135	0.6472	0.675

Table 3:Statistic of the four meshes. Has been evaluated the number of elements, the minimum quality and the average quality. The average quality represents the skewness rated from 0 to 1 where 1 represent the best possible element.

To obtain accurate results while minimizing computational costs, a mesh sensitivity analysis was conducted by comparing the maximum velocities within the CSF domain for four different meshes, using the boundary condition described in the next section. Figure 23 represents the maximal velocities obtained with the different meshes over one cardiac cycle.

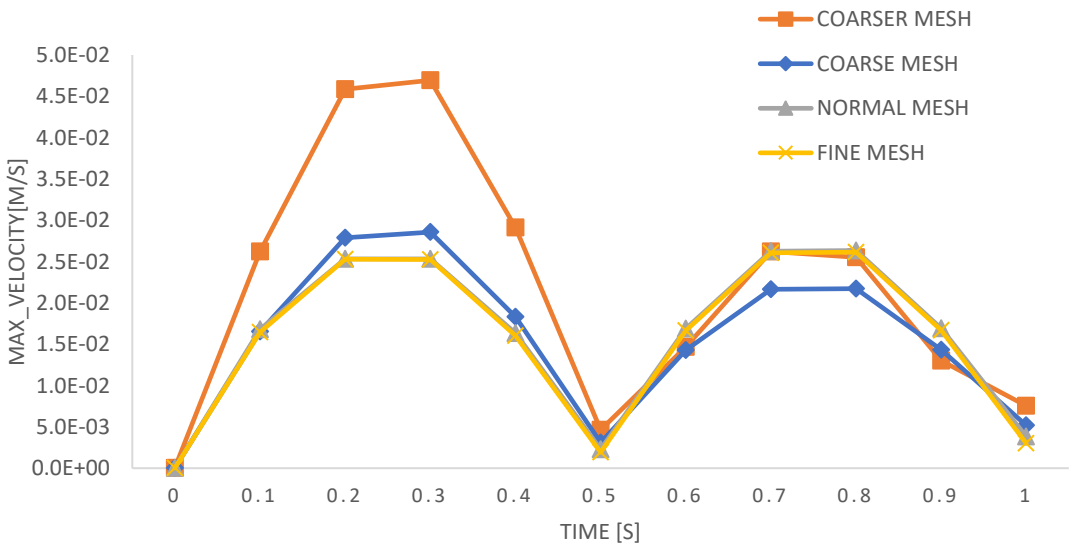

Figure 23: Mesh sensitive analysis conducted on the maximal velocities using the 4 meshes before described.

To compare the different meshes, the percentual difference of the maximum velocity values at each time step was calculated using equation 5.1:

$$Pd_n = \frac{v_{max,n-1} - v_{max,n}}{v_{max,n-1}} \qquad (5.1)$$

Here, Pd_n is the percentual difference, $v_{max,n}$ the parameter value in the nth mesh, and $v_{max,n-1}$the same parameter evaluated in less fine mesh n-1. The results, as depicted in Figure 24, indicate that the percentual variation between the Normal and Fine mesh during the simulation exhibits a maximum deviation of 1.2% and an average deviation over time of 0.32%. As a result, the "Normal" mesh was selected to conduct the simulation in order to reduce computational time.

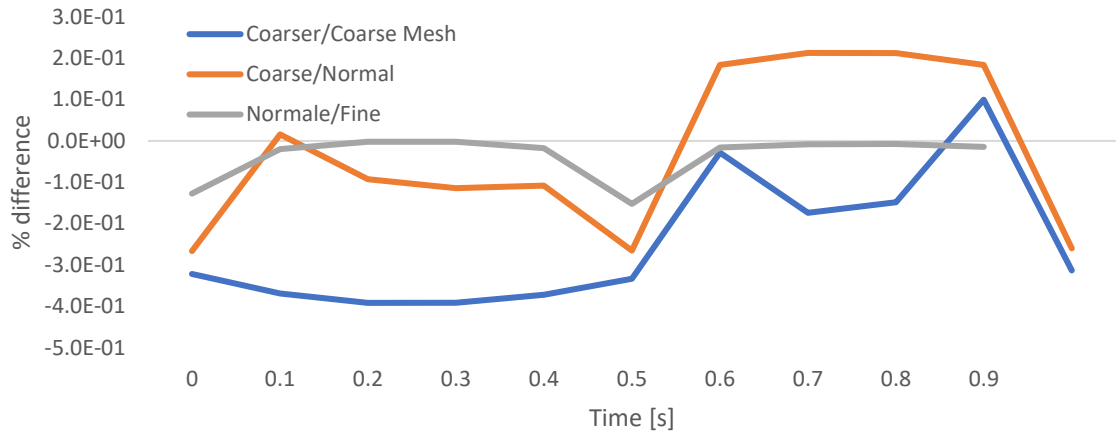

Figure 24: Velocities percentual variation due to the changes in mesh over time

5.2.3 Boundary conditions

The boundary conditions utilized in the study were based on those presented in Vandenbulcke et al. (35) which align with the current understanding of physiological processes influencing CSF flow.

Inlet boundary conditions:

- A constant CSF production rate of 6.67E-03 ml/s was considered at the lateral ventricles.
- The pulsation of the brain tissue caused by the cardiac cycle was taken into account. To simulate this, a sinusoidal velocity waveform was incorporated with a frequency of 1Hz and an amplitude of 0.11 ml/s at the lateral ventricles. The net flow over each cardiac cycle was set to zero.
- To account for the volume changes in large arteries, including the basilar arteries, another sinusoidal velocity waveform with a frequency of 1Hz and an amplitude of 5.05 ml/s was added in the region of the basilar artery. The net flow over a cardiac cycle was maintained at zero.
- The respiratory pulsations were considered as venous volume changes. The venous volume changes were included as a pulsating source term with a frequency of 0.2Hz, an amplitude of 1.01 ml/s, and a zero net flow over a cardiac cycle.

Figure 25 and Table 4 provide an overview of the boundary conditions.

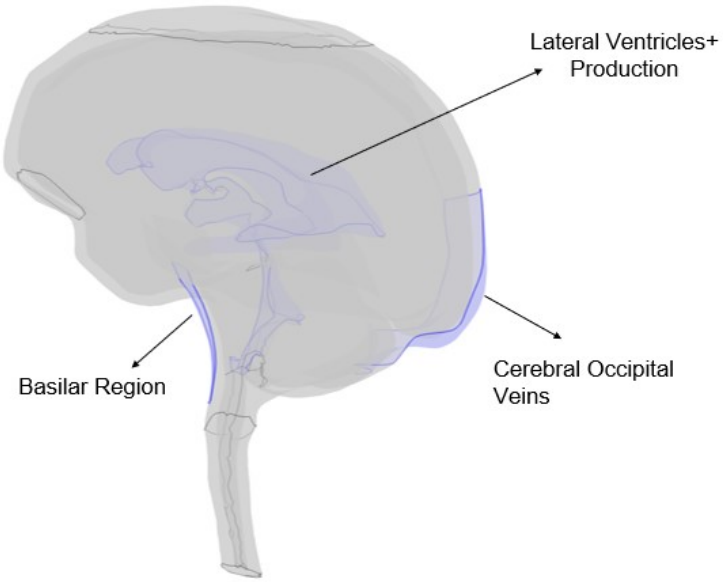

Figure 25: Visualization *of the locations of the inlet boundary conditions*

AREA	TYPE	AVERAGE (ml/s)	AMPLITUDE (ml/s)
Lateral Ventricles	Constant	6.67E-3	/
Lateral Ventricles	Sine wave 1Hz	/	0.11
Basilar Region	Sine wave 1Hz	/	5.05
Occipitals Veins	Sine wave 0.2 Hz	/	1.01

Table 4: Overview of average values (avg.) and amplitudes (amp.) of all the inlet boundary conditions

Outlet boundary conditions:

The model incorporates four outlets, which are depicted in figure 26, to account for various drainage pathways into the venous and lymphatic systems: the arachnoid villi, interstitial space, spinal pathway, and lymphatic system. Table 5 provides an overview of the outlet boundary conditions. A zero-pressure condition is set for the outlet corresponding with the arachnoid villi. For the other outlets, volumetric flow is imposed, which is calculated by summing all the inlet boundary conditions and then multiplying these with the net outflow percentage specific to each outlet. The outlet percentages for the spinal drainage pathway, lymphatic system, and interstitial space are set at 20%, 30%, and 20% respectively. An overview of the different outlet conditions is presented in Figure 26 and Table 5.

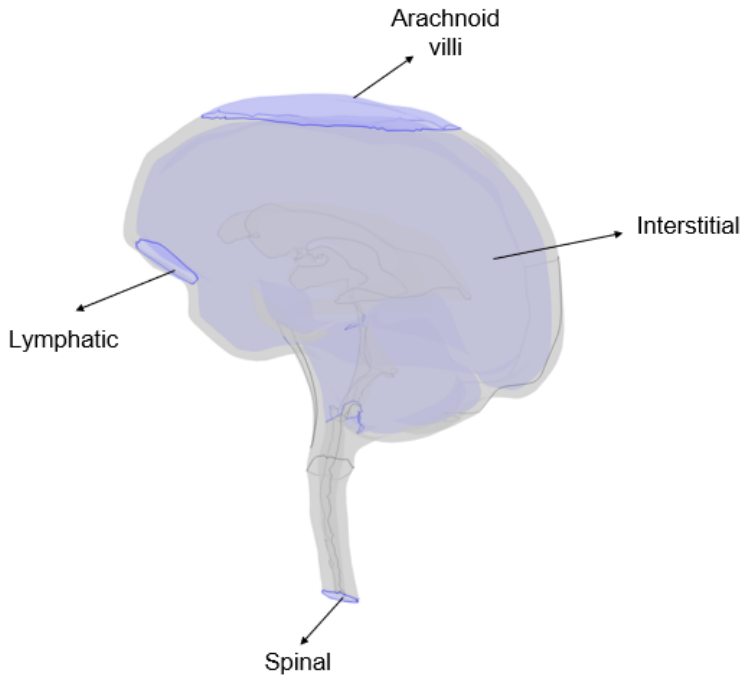

Figure 26: Region in which inlet boundary condition has been applied

	Spinal	Lymphatic	Interstitial
% of total inflow	20	30	20

Table 5: Overview of outlet boundary condition

AREA	Type	Average (Pa)	Amplitude
Arachnoid villi	Constant	0	/

Table 5

5.2.4 Solver setting

The CSF has been model with the same proprieties of water density 998.2 $\frac{kg}{m^3}$ and a dynamic viscosity of 0.001003 $\frac{kg}{ms}$. The CSF has been considered as incompressible. The CFS flow is driven by the Navier-Stokes equations, equation 5.2, neglecting the effect of the gravity.

$$\rho \frac{\partial \vec{v}}{\partial t} + \rho(\vec{v} \cdot \nabla)\vec{v} = -\nabla \vec{p} + \mu \nabla^2 \vec{v} \qquad (5.2)$$

With the ρ the fluid density (SI unit $\frac{kg}{m^3}$), $\vec{v}$ the velocity vector (SI units $\frac{m}{s}$), μ the viscosity (SI units $\frac{Kg}{ms}$) and $\vec{p}$ the pressure field (SI units Pa). The equation 5.2 represent the momentum balance for a Newtonian fluid in which the left side the momentum convection and the right side represent the viscous force and the pressure gradient. Additionally, due to the incompressibility assumption, the conservation of mass can be written as the divergence of the velocity vector, which is zero.

$$\nabla \cdot \vec{v} = 0 \qquad (5.3)$$

In the simulation, the model was run using COMSOL Multiphysics (COMSOL inc.) with the package laminar flow for a duration of 5 cardiac cycles. The time step for the simulation was determined using the default time-dependent solver in COMSOL Multiphysics, which automatically adjusts the time step size to maintain the desired relative tolerance which is maximum amount of error set as 0.01. The maximum time step used in the simulation was set to 0.05s.

5.3 Result

In this chapter section the results of the previous setup is presented. This result serves to give an insight of the full circulation of the CSF in a healthy condition. Figure 25 presents a comprehensive view of CSF velocity's magnitude direction during the third cardiac cycle at the sagittal plane. The analysis encompasses six-time steps: (A) at 3.05s, (B) at 3.25s, (C)3.45s(D)3.55s, (E) at 3.75s and (F)at 4s. The flow patterns are examined through streamlines. At the beginning of the systolic phase (A), CSF flows from the ventricles, coursing through the spinal SAS and into the cranial SAS. As the systolic phase reaches its apex (B), the flow retains its direction but experiences an increase in velocities, especially within the lateral ventricles. Towards the end of systole (C), the flow changes direction due to cardiac pulsations, transitioning from the spinal SAS to the cranial SAS, while remaining consistent in the lateral ventricles. During the initial phase of diastole(D), the flow maintains its direction, but the flow in the lateral ventricles undergoes a reversal. Similar to the systolic phase, the flow attains peak velocities during mid-diastole (E). In the final phase of diastole, the flow slow down. (F)

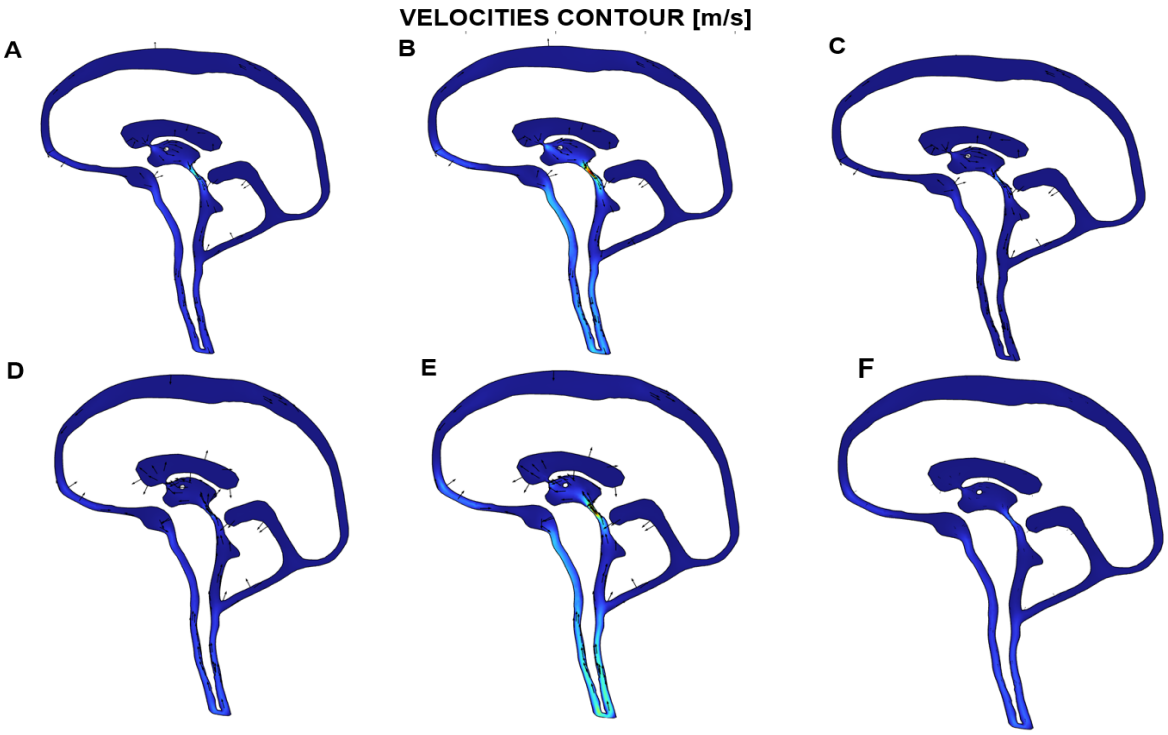

Figure 27: Contour velocities transversal section and 3d velocities arrow during 6 phases of the third cardiac cycle.

The flow in the spinal SAS through a cross section has been analysed as depicted in Figure 28. The pulsation of the amplitude in the spinal SAS c2 range 1.5 to -2 $\frac{m^3}{s}$.

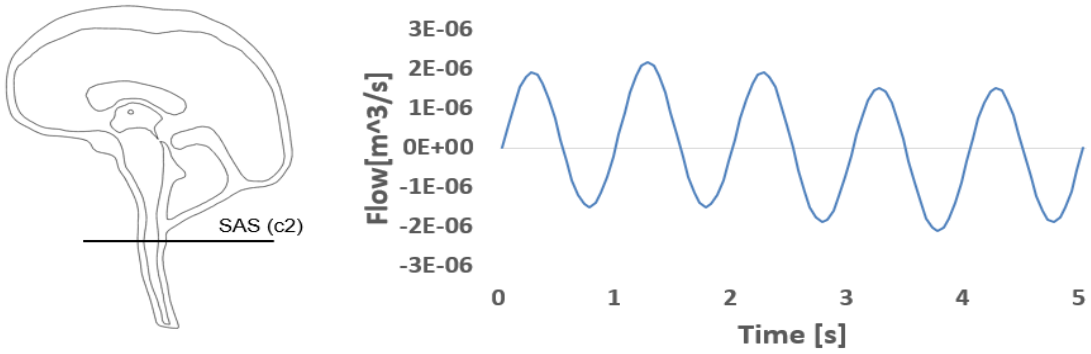

Figure 28: Flow evaluated in the section of SAS at the level of second vertebrae C2 during the 5 cardiac cycles

Figure 29 represents the velocities contour taken at the lower part of the cerebral aqueduct. The maximal velocities happen at the 3rd cardiac cycle at 3.25s with a value of 23.26 $\frac{mm}{s}$

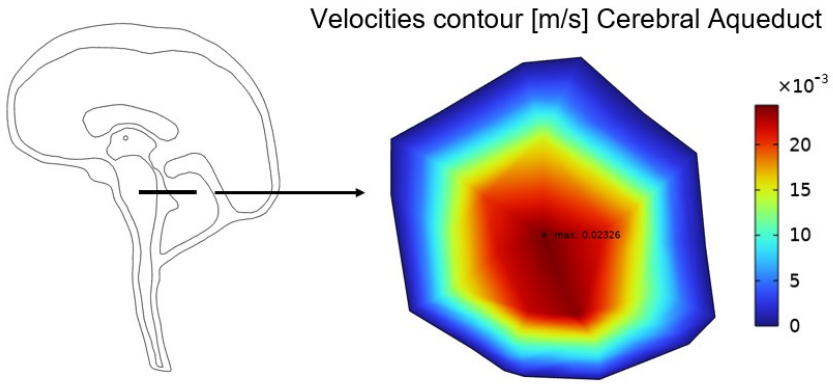

Figure 29: Velocities contour and maximal velocities at the cerebral aqueduct

Figure 30 represents the spatial pressure difference between a point in the lateral ventricles and the average pressure in the SAS c2 where the maximal value of the pressure difference has an amplitude of 0.0093 *mmHg*.

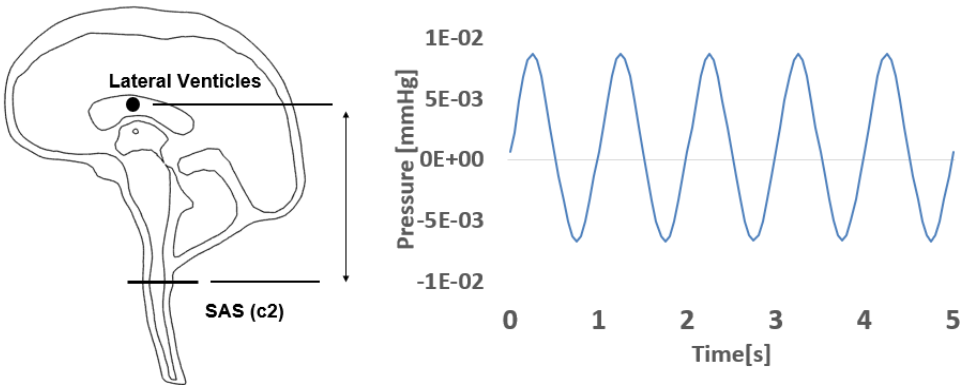

Figure 30: Pressure difference between the upper part of the lateral ventricles and the spinal SAS c2. On the left the sagittal plane of the geometry with the representation of the two planes in which the pressure has been evaluated

In Figure 31 the intracranial pressure has been depicted; the intracranial pressure corresponds to the average pressure at the interstitial outlet.

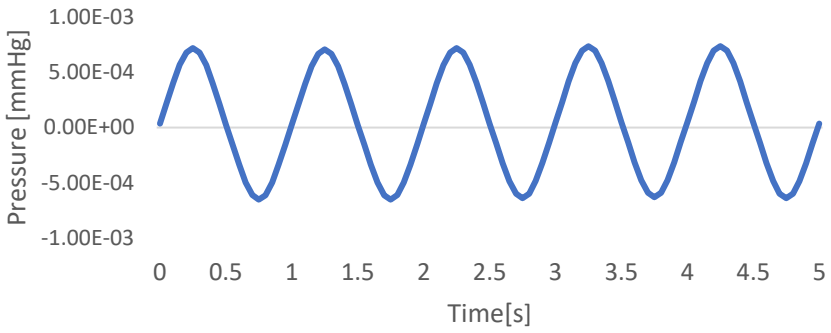

Figure 31: Intracranial pressure evaluated at the int surface during the 5 cardiac cycles

5.4 Discussion

In this section, 3D in silico model of the cranial SAS and the cervical part of the spinal SAS has been built in order to have a comprehensive understanding of the dynamics of the CSF flow. The full 3D transient simulation considers not only the arachnoid villi drainage path but also focused on the lymphatic and spinal absorption pathway including the pulsatile motion due to both cardiac and respiratory cycles.

The Table 6 represents the values obtain in the literature of different studies focusing on the maximal flow across the spinal SAS at the level of the second vertebrae and the maximal velocities evaluated at the cerebral aqueduct. Both of the values are in a good agreement with the one obtained in these studies with 2.3276 $\frac{cm}{s}$ as maximal velocities at the cerebral aqueduct and a value of 2.2 $\frac{ml}{s}$ flow at the spinal SAS.

Max Velocities cerebral aqueduct	Max flow during systolic phase	Reference
1.2 $\frac{cm}{s}$	3.4 $\frac{ml}{s}$,	Vandebulcke et al. (35)
14.6 $\frac{cm}{s}$	1.815 $\frac{ml}{s}$,	Gupta et al. (37)
/	2.1 $\frac{ml}{s}$,	Bennihause et al. (42)
1.23 $\frac{cm}{s}$,	4.3 $\frac{ml}{s}$,	Tangen et al. (60)
2 $\frac{cm}{s}$	/	Filllingham et al. (41)

Table 6: *Max velocities at the cerebral aqueduct and maximal flow during the systolic phase reported in scientific literature*

On the other hand, the pressure values obtained in this study were compared to those reported in the literature were found to be an order of magnitude lower. The maximal amplitude of the pressure drops between the lateral ventricles and the spinal SAS seems to be underestimated in this model compared to the study by Vandenbulcke et al. (35) and Fillingham et al. (41) that obtain values in the range of 0.015

mmHg while this study a value of 0.0093 mmHg. In vivo pressure drops suggest a value of 0.1 mmHg (69). Further investigation is needed to understand the reason of this pressure underestimation

In terms of intracranial pressure, the expected range based on physiological data is typically between 7 mmHg and 15 mmHg (68). However, in this study, the pressure obtained exhibited a sinusoidal behaviour with an average of zero pressure, which does not align with the expected physiological data. This is probably due to the zero pressure apply at the arachnoid villi outlet.

5.5 Limitations

It's important to note that the model used in this study only allows the acquisition of relative pressure and does not have the capability to simultaneously obtain pressure and velocities. Furthermore, the model does not account for the compliance of the cerebral brain tissue, whether by using a windkessel model (as done in Vandenbulcke's study (35) or employing a FSI approach. Due to these limitations, it is only possible to obtain relative pressure values in this study.

Despite considering both the pulsations of respiration and the cardiac cycle, as well as accounting for both the spinal lymphatic drainage pathway and the arachnoid villi, this study only achieved a match with physiological flow data but not a perfect match with the pressure.

The method, of introducing a percentage of the total inflow to outlets spinal, lymphatic, and interstitium by creating a variable inflow, which is the sum of all inlet boundary conditions, and then multiplying this variable by a percentage for each outlet, imposes a constant absorbing during the cardiac cycle which does not reflect the physiological condition.

Furthermore, the positioning of arteries and veins is confined to two approximate locations and does not perfectly align with the actual physiological areas. Additionally, the inlet boundary conditions are based on approximate sinusoidal values and lack patient-specific data

6 CFD STUDY OF THE EFFECT O THE OBSTRUCTION

6.1 Introduction

The principal objective of this chapter involves investigating the effects stemming from a three-dimensional obstruction occurring at the foramen magnum (CM1). Within this chapters a CFD analysis has been executed, encompassing varying degrees of obstructions, specifically at rates of 40%, 60%, and 100%. The creation of a three-dimensional artificial herniation has been realized through the implementation of an ellipsoidal volume. Notably, the deployment of this geometric configuration offers a distinct advantage, as its uniformity is upheld across all simulations. This strategy mitigates the influence of individual-specific anatomical variations between scenarios featuring healthy and obstructed conditions, a factor that might otherwise overshadow the isolated impact of the obstruction itself.

The aim is to underscore the impact of the different degrees of obstructions on CSF circulation. This is achieved through an assessment of the difference in pressure attributed to the herniation, followed by a study of velocity at the level of the herniation and in regions situated below it.

6.2 Material and methods

Given the significant computational resources required and considering that the main focus of the thesis is on the 3D effects of the obstruction at the foramen magnum, the CFD investigations of the obstruction's effects were conducted on a specific section of the complete geometry used in the Chapter 5. To reduce computational costs, the full geometry was cropped 6 cm above and 14.8 cm the plane with z zero coordinat3 as presented in Figure 32

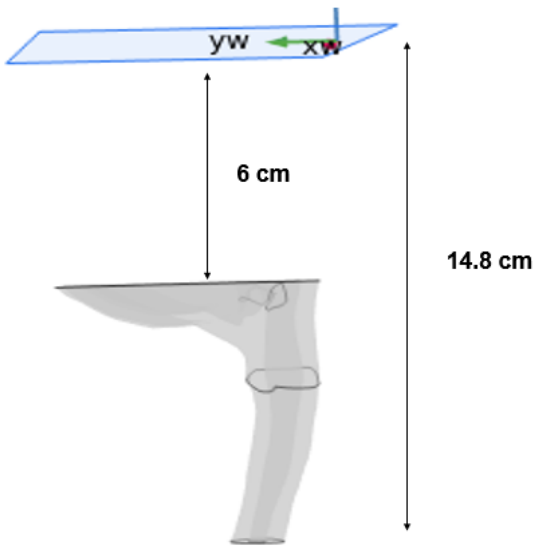

Figure 32: Crop representation of the full geometry

In order to create and simulate different level of obstruction, an idealized 3d model of the obstruction has been created using an ellipsoid. Moving the ellipsoid more or less inside the cranial SAS allows increasing or decreasing the level of obstruction.

To have a quantification of the level of the obstruction, the geometry has been intersected with a plane 25mm under the top of the geometry. Then, the equation below is used to have quantify the % obstruction:

$$\%Obstruction = \frac{AreaFM - AreaHerniation}{AreaFM} \quad (6.1)$$

It's important to note that the plane is at arbitrary height and location. Also, the % obstruction only accounts for the back side of spinal SAS.

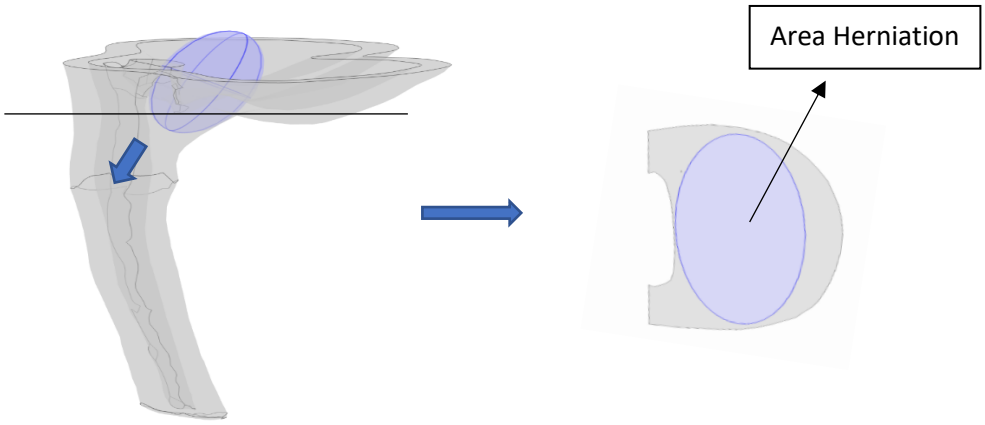

Figure 33: Representation of the left of the 3D geometry of the ellipsoid simulating the herniation and on the right the cross section of the SAS in order to quantify the level of the obstruction

Using the equation 6.1, 4 levels of obstruction have been created: a healthy condition, 40% of obstruction, 60% of obstruction and 100% of obstruction as summarized in Table 7.

CASE	% OBSTRUCTION
1	Healthy Condition 0%
2	CM1 40%
3	CM1 60%
4	CM1 100%

Table 7: Different level of the herniation that has been considered in this study

6.2.3 Generation of the mesh

The computational mesh was constructed using the user-controlled mesh tool provided in COMSOL Multiphysics (COMSOL Inc.). This tool can be used to manually build and edit the meshing sequence for

creating 2D and 3D meshes. To obtain a better convergence as reported in (61), a boundary layer composed of prismatic elements surrounding the surface of the spinal cord has been added as depicted in figure 33. The rest of geometry is meshed using free tetrahedral elements.

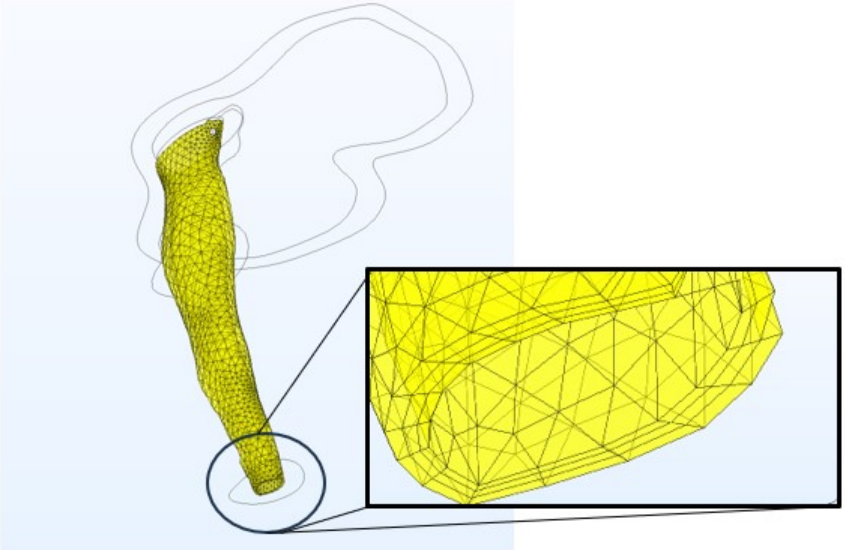

Figure 34: Representation of prismatic element around the spinal cord

Three different mesh has been generating using different size of the free tetrahedral element as represent I in Table 8.

	Mesh 1	Mesh 2	Mesh 3
Elements	50.304	86.456	180.623
Minimum quality	0.0086	0.057	0.069
Average quality	0.5727	0.605	0.6446

Table 8: Three different mesh that has been used in the mesh sensitive study

Figure 35 shows the maximal velocities in the geometry for the different meshes that have been used.

The meshes are compared using the equation 5.1 as used in chapter 5.

Since the % difference, reported in the figure 35, between case3 and case2 present an percentage average error over time of 0.22 and a maximal error percentage of 1.2, the mesh in the CASE 2 has been used to reduce the computation time.

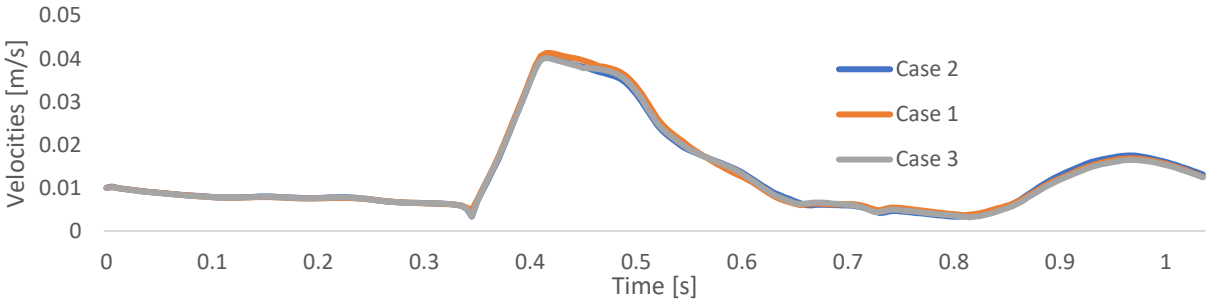

Figure 35: Plot of the maximal velocities in the all geometry along the cardiac cycle using the different meshes

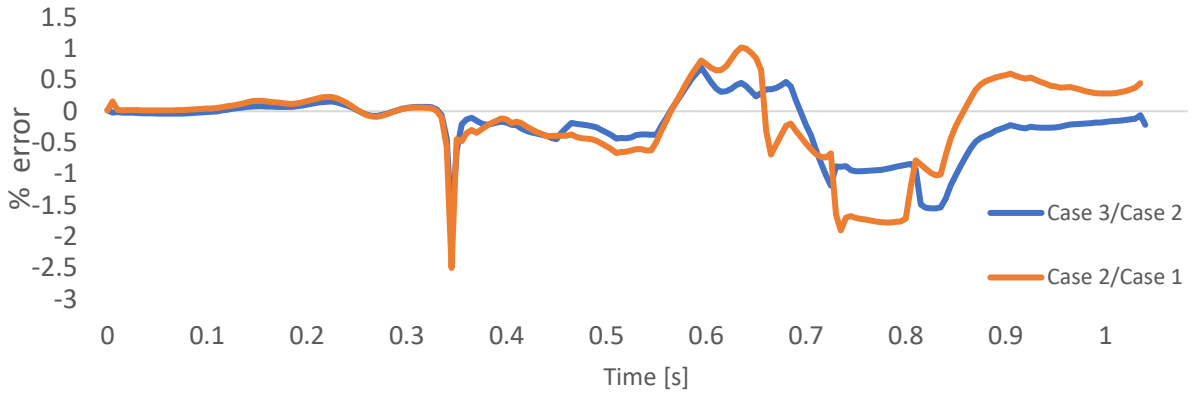

Figure 36: % error between the different meshes

6.2.4 Boundary Conditions

The inlet boundary conditions are determined based on PC-MRI flow data obtained from a healthy individual at the medical research institute Mātai (Gisborne, New Zealand) using a SIGNA Premier scanner. Flow was specifically measured in vivo in the spinal SAS at the C2 level and in the cerebral aqueduct showed in Figure 37, and extracted using the software CVI42 (Circle Inc.).

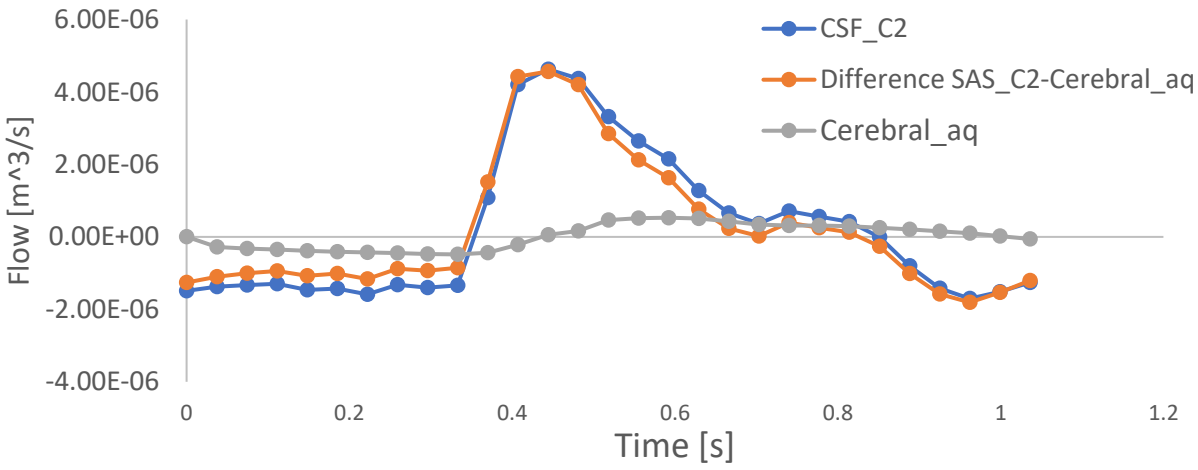

Figure 37: PC-MRI results obtained from measurements at both the cerebral aqueduct and the spinal subarachnoid space (SAS) at the level of the second cervical vertebra, along with the contrast between these two sets of data

To implement these measurements, the flow rate from the cerebral aqueduct is directly applied to the corresponding area representing the end of the cerebral aqueduct (INLET1), while the difference between the flow rate from the SAS at the C2 level and the cerebral aqueduct is applied to the designated region (INLET 2), as shown in Figure 38. This application maintains the conservation of mass.

As for the outlet boundary conditions, a pressure of 1333.2 Pa or 10 mmHg has been selected, lying in the physiological range of 7-15 mmHg of intracranial pressure. (62)

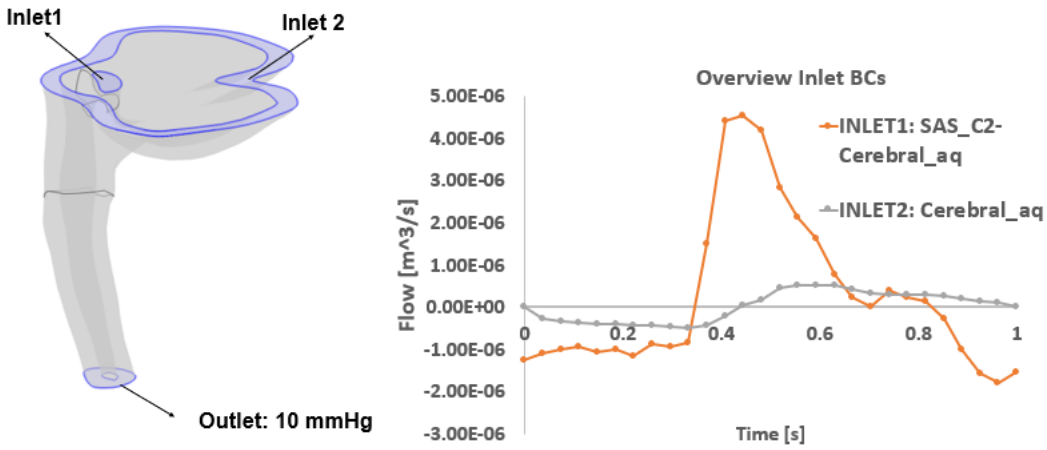

Figure 38: Overview of boundary condition on CFD study

6.2.5 Solver setting

Four simulations were conducted by solving the Navier-Stokes equation, assuming the CSF to be incompressible and possessing the same properties as water (viscosity = 0.001003 $\frac{Kg}{ms}$, density =998$\frac{kg}{m^3}$). These simulations were performed using the 'Laminar Flow' module in the COMSOL Multiphysics software package. The choice of the 'Laminar flow' it's because of the low Reynold numbers (maximal value of 34 in the set up with 100% herniation). The simulations covered one complete cardiac cycle, ranging from 0 to 1.035 seconds, which aligns with the duration of the provided PC-MRI input. The time step for the simulations was determined using the default time-dependent solving scheme in COMSOL Multiphysics. In order to have a good resolution in the obtained result a maximum constant time step has been imposed of 0.01s.

6.3 Result:

The objective of this chapter is to use the CFD approach to assess the impact of obstructions with varying degrees on the flow. The evaluation of the velocities has been made at the flow peaks of the CSF inlet measure at the SAS (c2) at 0.44s and when the flow is 0 at 0.85s as represented in Figure 39.

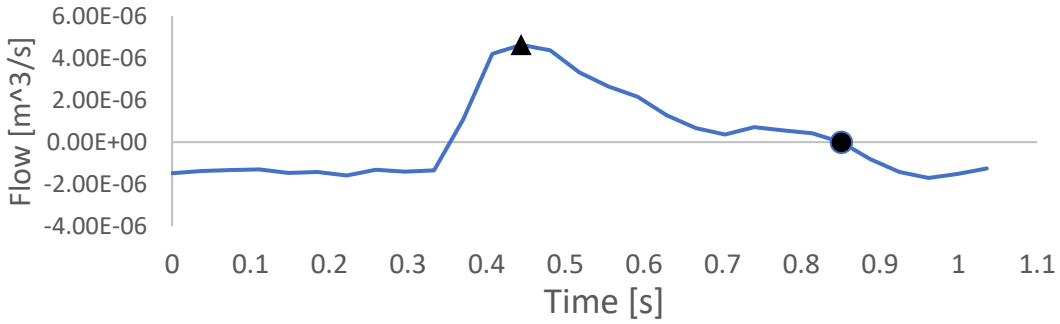

Figure 39: Representation of the time instant use to evaluate the CSF flow parameters at the PC-MRI in vivo measure used as input at the 'INLET 2'

The Figure 40 presents the velocity contours on the sagittal plane, comparing different cases of obstruction at 0.44 seconds, indicating the maximal velocity's location and values.

The image demonstrates that an increased level of obstruction creates resistance in the flow, leading to a slight increase in maximal velocities from 53 to 63 $\frac{mm}{s}$. However, at 0.44 s, there are no changes in maximal velocities in both 40% and 60% obstruction cases with a value of 58 $\frac{mm}{s}$. Velocities at t=0.85, plotted in Figure 41 show a significant slowdown in comparison to the one at 0.44s, with maximal velocities of 10 mm/s in the healthy condition and 7.8 mm/s in the presence of the obstruction at the level corresponding to the cerebral aqueduct.

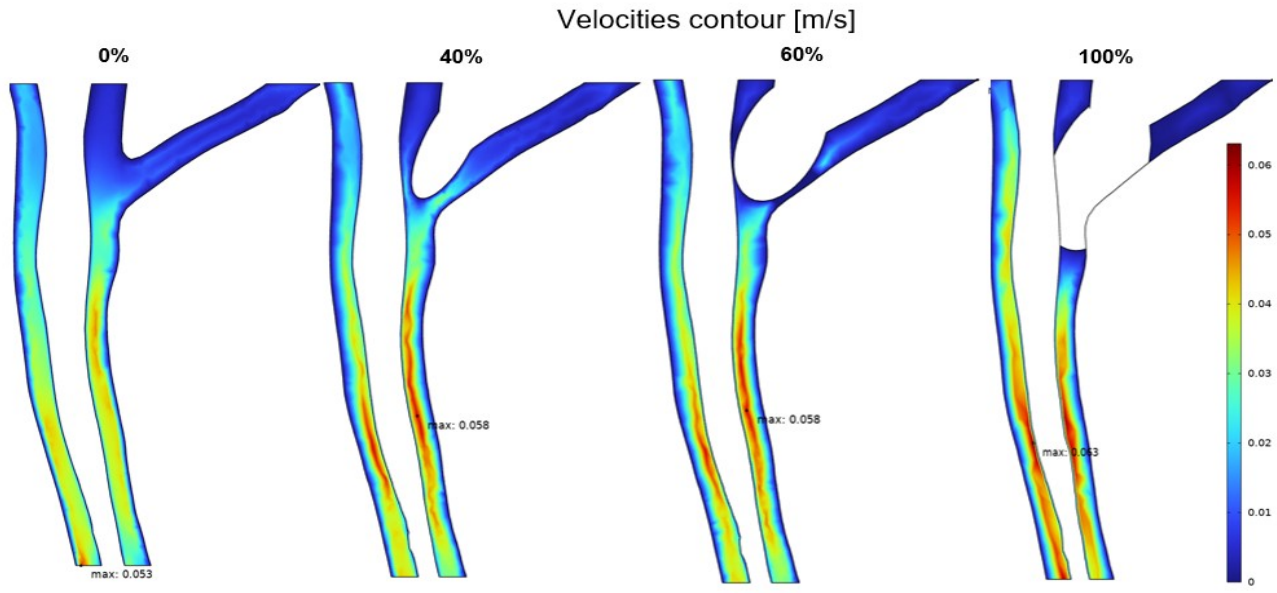

Figure 40: Velocities contour in m/s at the sagittal plane during the systolic peak at 0.44s

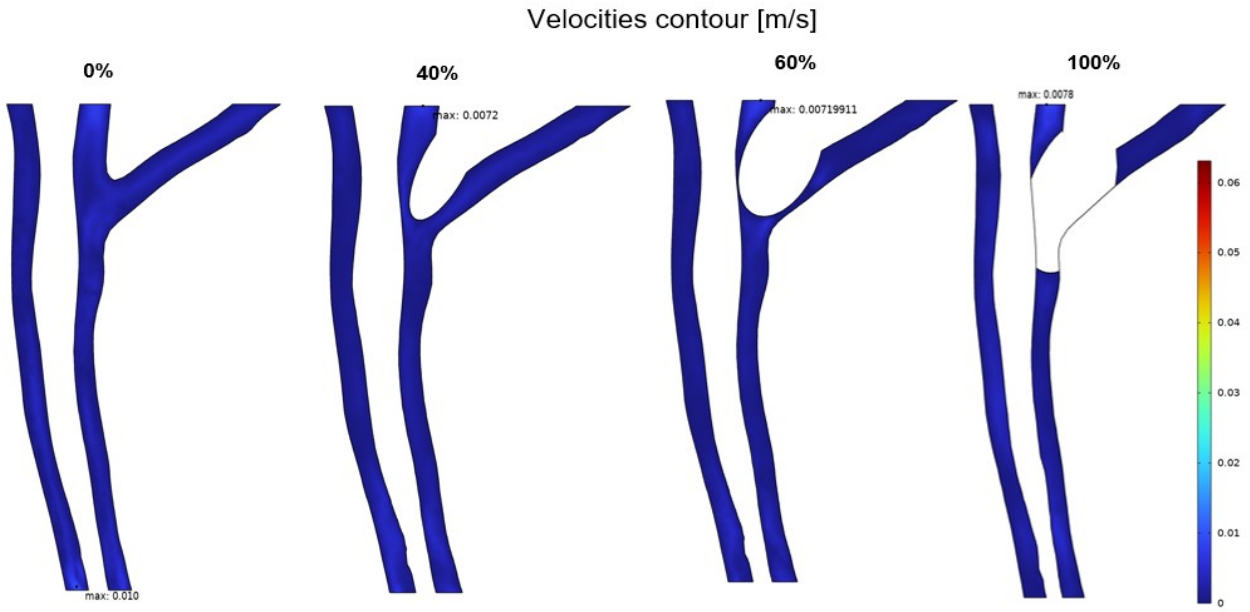

Figure 41: Velocities contour in m/s at the sagittal plane during the systolic peak at 0.85s

To investigate the obstruction's effect further, two slices are created at the herniation level (z =-0.023m) and the level of the spinal SAS below the obstruction (z =-0.036m), as depicted in the Figure 42.

.

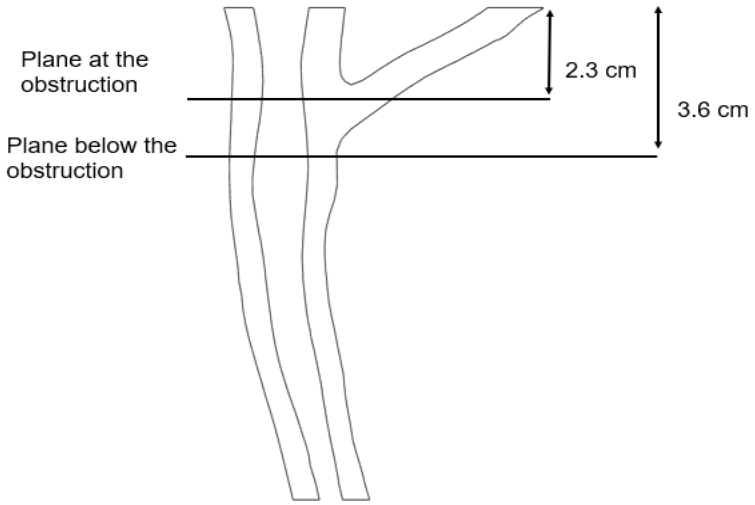

Figure 42: Representation of the two level that has been considered to study the effect of the herniation

Figure 43 presents the maximal velocities in the plane before the obstruction over the cardiac cycle for the different degrees of herniation. This is to demonstrate the downstream effect of the obstruction.

In the absence of obstruction, the velocity peak reaches a value of 39 mm/s. With a 40% obstruction, the velocity peak increase to 47.7 mm/s and it remains roughly steady for both 60% and 100 obstructions with a value of 48.2 mm/s. It appears that an increase in degree of the obstruction doesn’t necessary lead to an increase in velocities below the obstruction and that these velocities only indicate the presence of the obstruction.

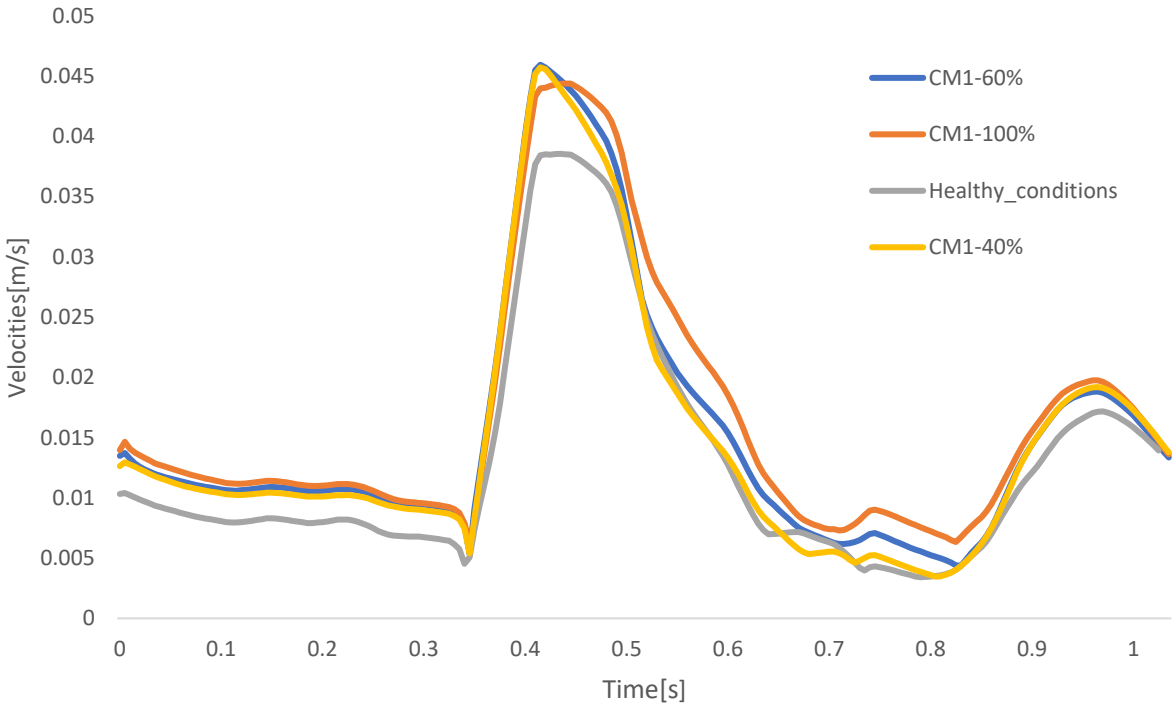

Figure 43 Maximal velocities along the cardiac cycle with the different levels of obstruction below it

Figure 44 shows the velocities contours for an axial plane corresponding with the plane below at 0.44s. No significant increase in maximal velocities is observed, but with increasing obstruction percentage the distribution of velocities changes and consists of larger areas of high velocities. For the 100% of the obstruction, the contours clearly demonstrate that the CSF circulates only in the pontomedullary cistern, the frontal side of the spinal subarachnoid space, here the obstruction is not present.

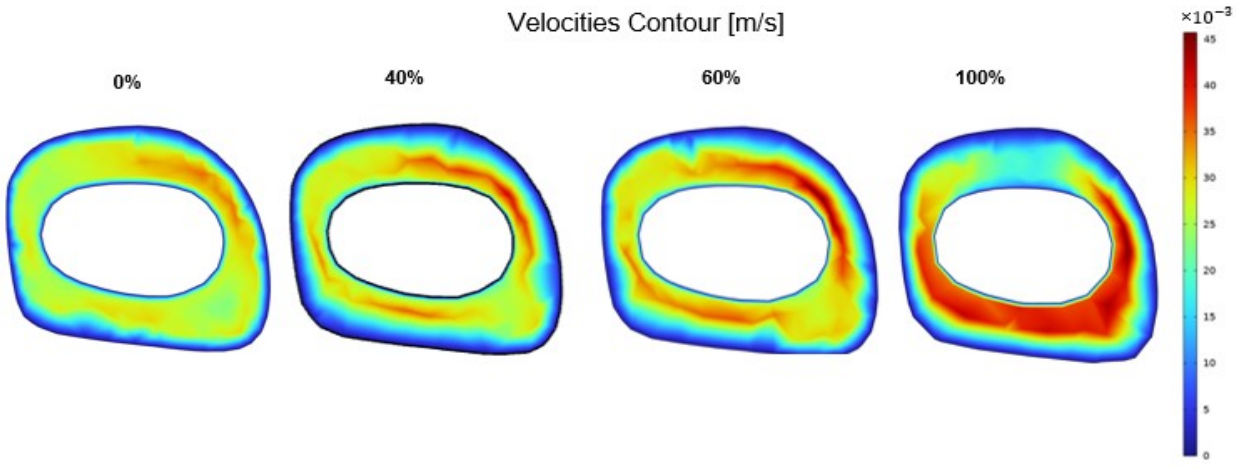

Figure 44: Velocities contour in plane bellow the obstruction at 0.44s, the upper part of the figure represents the back side of the spinal SAS

To understand what happens in the region of the obstruction, both maximal velocities over the cardiac cycle and velocities contours at 0.44 s are plotted respectively in Figure 45 and Figure 46 at the level of the herniation. From the figure 45, it appears that at the level of the obstruction the effect of the degree of

obstruction becomes evident with an increasing maximal velocity due to an increasing percentage of obstruction.

The distribution of velocities indicates almost zero flow passing through the back side of the spinal SAS and all flow passing through the front side of the spinal SAS with 60% and 100% obstruction. Meanwhile, in the 40% case, there is flow at both sides.

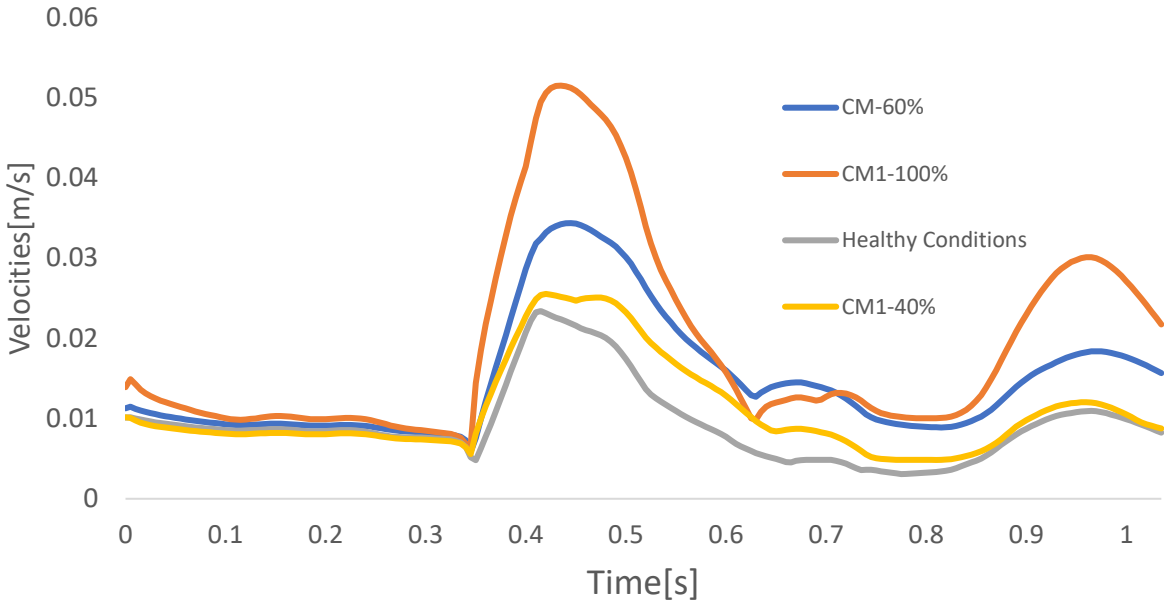

Figure 45: Maximal velocities along the cardiac cycle with the different level of obstruction at the level of the herniation

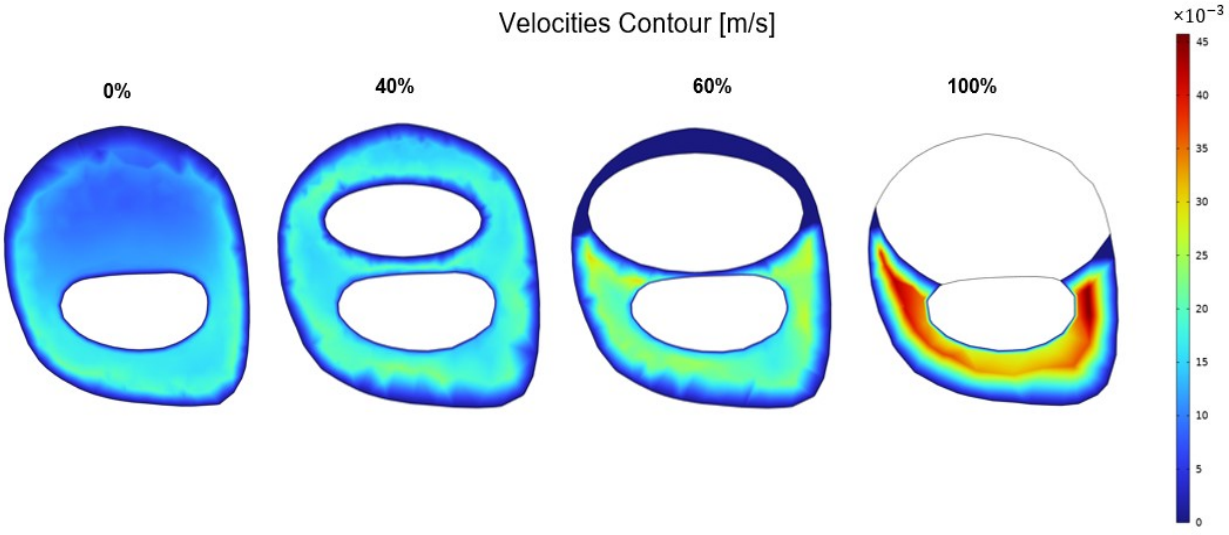

Figure 46: Velocities contour [m/s] in the level of the herniating during at t=0.44s

In the Figure 47 a diagram representing the maximal velocities in the spinal SAS and at the herniation level are showed. From the image the effect of increasing maximal velocities at the level of the herniation appears clearly, while the max velocities at the plane below the obstruction (SAS c2) remain almost steady in the presence of the obstruction.

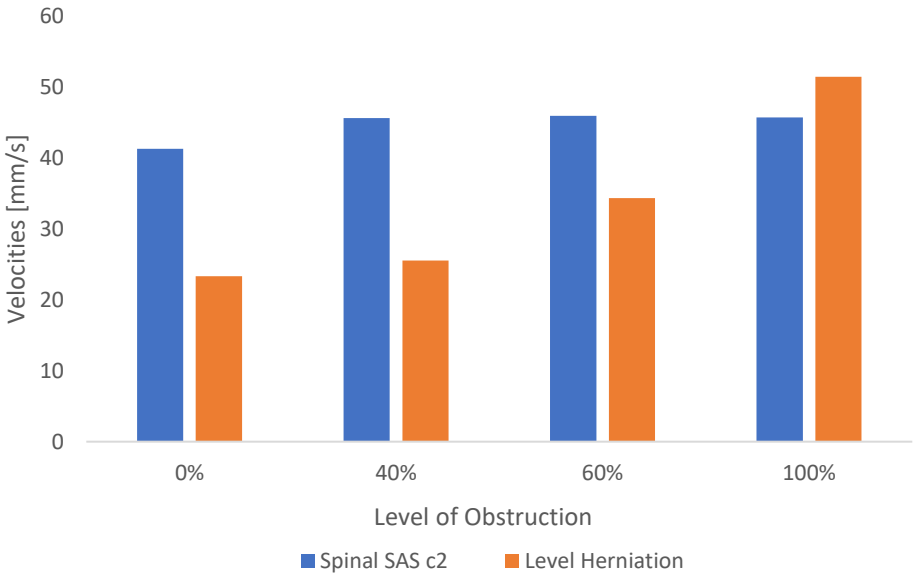

Figure 47: Diagram representing the maximal velocities in the spinal SAS and at the level of the herniation during the systolic peak

To evaluate the effect of the obstruction on the pressure, the pressure contour at 0.44s is plotted in figure Figure 48. From the figure an increase in pressure as a result of the obstruction is noticed. Increasing the obstruction reveals that the area most affected by the pressure increase is the region corresponding to the cisterna magna, while there is lower pressure on the other side of the SAS where the obstruction is not present.

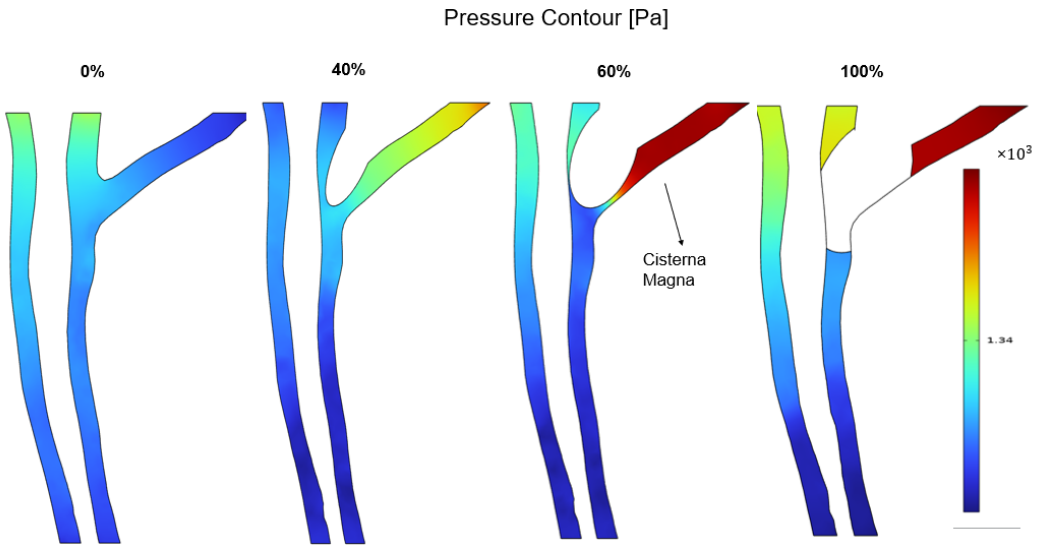

Figure 48: Pressure contour at the sagittal plane at 0.44s

The pressure drops between the cerebral aqueduct and the plane below the obstruction is displayed in Figure 49. It is clear that there is an increase in absolute pressure drop throughout the cardiac cycle when increasing the level of obstruction, with a peak of 12.4 Pa with 100% obstruction compared to 5.3 Pa in the healthy condition.

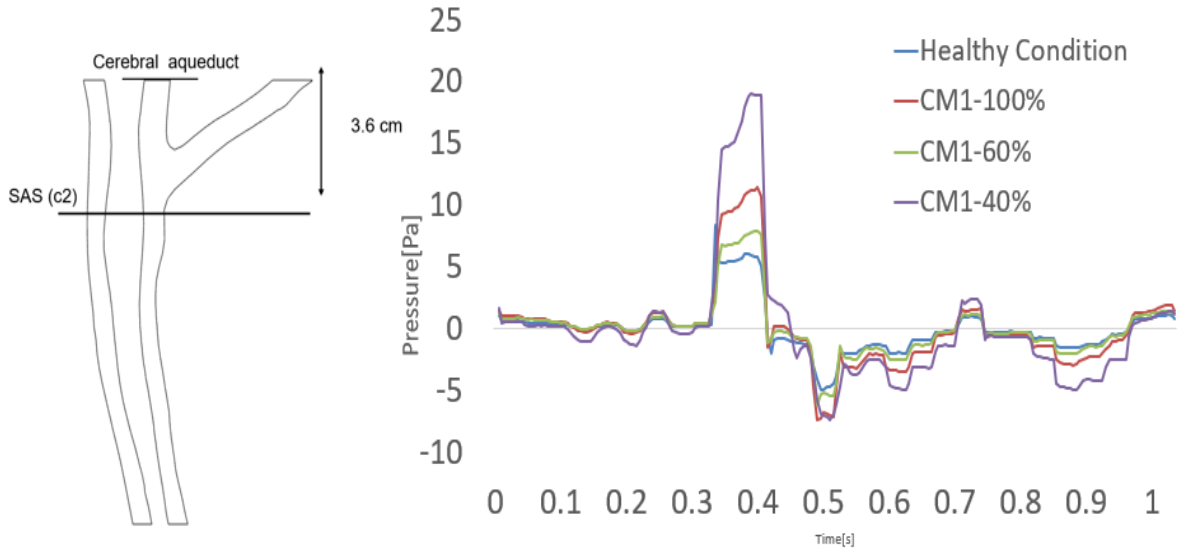

Figure 49: Pressure drops between the cerebral aqueduct and the plane below the obstruction along the cardiac cycle

The pressure drops between the cranial SAS excluding the area corresponding to the cerebral aqueduct has been evaluated in Figure 50. The pressure is more than 4 times higher in the case of 100% of the obstruction reaching a peak of 48 Pa in comparison to the healthy condition. An increase is noticed also for 60%herniation. On the other hand, the pressure in the healthy condition and in 40% as roughly the same pressure drop.

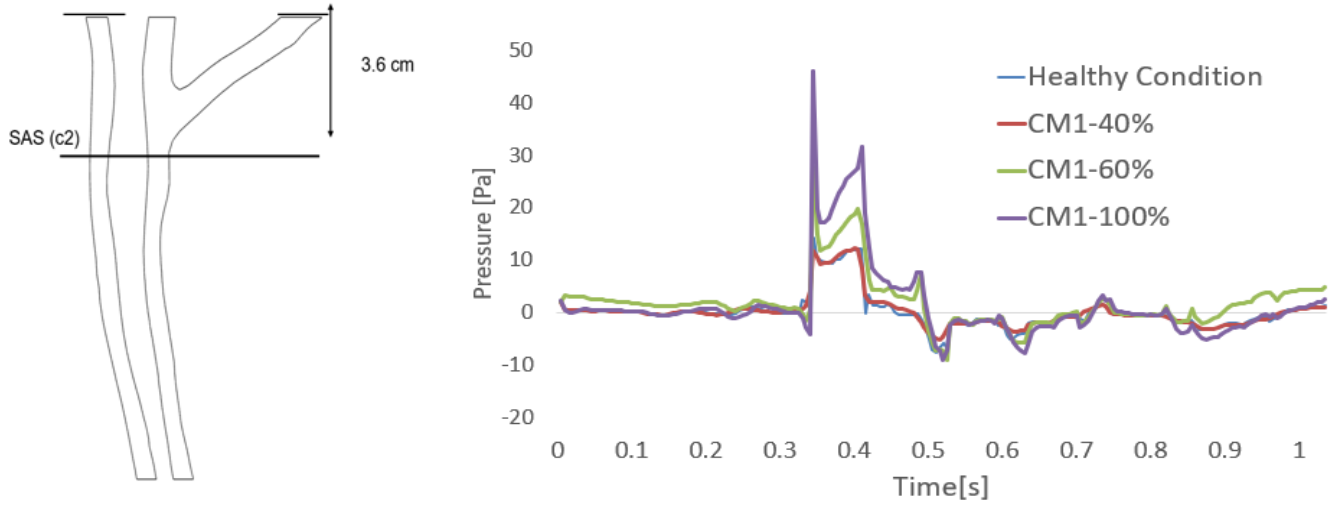

Figure 50: Pressure drops between the cranial spinal SAS and the plane below the obstruction along the cardiac cycle

The Reynolds number is assessed to determine the consistency of the laminar flow hypothesis, and it is found that the maximum value in the all geometry under 100% obstruction is 34. These results indicate that the assumption of laminar flow remains valid even in the presence of obstruction.

6.4 DISCUSSION

The purpose of this chapter is to assess the impact of an obstruction in the cranial SAS on local CSF pressures and velocities for different obstruction levels.

Peak velocities of 45.72 mm/s in the spinal SAS with 100% obstruction and values up to 40.3 mm/s in the healthy condition were observed. An in vivo study by Bunck et al. (69) using a 4D PC-MRI on 10 healthy individuals reported velocities of 40±10 mm/s at the spinal SAS C2 level and maximal velocities of 84±69 mm/s with CM1. At the level of the foramen magnum, the same study found velocities of 32±10 mm/s in healthy conditions and velocities of 76±5.0 mm/s with CM1. The values obtained in this study seem to align with in vivo data, although there might be an underestimation of maximal velocities in case of obstruction.

From the sagittal plane figure, it is evident that the maximal velocities occur on the middle part of the cervical spinal SAS which is consistent with findings from the study conducted by Linge et al. (70). This study also reported that the pressure difference between conditions without obstruction and with CM1 is 2-3 times higher, which is roughly similar to the observations in my study. Additionally, the maximal velocities occur at time points 0.42s, 0.44s, and 0.43s for 40%, 60%, and 100% obstructions, respectively, following the highest-pressure peaks where the pressure drop reaches its minimum.

From Figure 47 appears that an increase in degree of the obstruction doesn’t necessary lead to an increase in velocities below the obstruction and that these velocities only indicate the presence of the obstruction. On the other hand, a non-linear relation between the level of the obstruction and the maximal velocities at the level of the obstruction was observed. This suggest that the effect of the degree of the obstruction act only locally at the level of the herniation

The pressure drops across the area corresponding to the cerebral aqueduct and the plane below the obstruction is more than double between the healthy condition and 100% obstruction. Analysing of the velocities in the spinal SAS and the aforementioned pressure drops leads to the same conclusion as stated in Støverud et al.'s (54) paper, which is that solely looking at velocities can indicate the presence of herniation, but evaluating pressure provides insight into the degree of obstruction, as also mentioned in chapter three.

6.5 LIMITATION

The study's first major limitation is the use only of a part of the full SAS. Additionally, the study fails to account for structures like dental ligaments and nerves, which could influence the flow and increase the Reynolds number. The CFD approach assumes a no-slip condition, neglecting the impact of cerebral tissue on the spinal cord and the effect of the herniation.

To the latter limitation, the next chapter presents a FSI study, assuming the neurological tissues as poroelastic materials. The effects of cerebral tissue and poroelasticity are incorporated allowing for the consideration of the wall as permeable to CSF rather than impermeable. This modification aims to gain insight into the accumulation of fluid in the spinal cord.

7 FSI STUDY OF EFFECT OF THE OBSTRUCTION

7.1 Introduction

The mechanical behaviour of the spinal cord has been described as non-linear viscoelastic, while the flow of CSF inside the SAS can be modelled as a water-like fluid by solving the Navier-stokes equations. However, the mechanical assumption made for the spinal cord as a viscoelastic material does not consider the fluid exchange between the SAS and the spinal cord. Therefore, the spinal cord is modelled as a poroelastic material, which considers the spinal cord tissue as comprising of two compartments: the solid phase, which includes neurons and spinal cord cells, and the liquid phase, which represents the CSF.

In this chapter, I will explain the concept of poroelasticity as a mathematical model and describe its implementation using the COMSOL Multiphysics (COMSOL Inc.) software. After explaining the theory of poroelastic coupling, two studies were conducted. :(1) the FSI poroelastic study without the obstruction to study the effect of the PIA mater and (2) the FSI poroelastic study with different levels of obstruction.

7.1. Poroelastic theory

The theory of poroelasticity considers a porous medium composed of an elastic matrix within which a fluid-filled pore exists. Biot initially introduced the implementation of poroelasticity theory (65). The porous material is modeled as a linear elastic substance using Hooke's law, while the fluid behaviour is described by Darcy's law.

Biot's theory is based on the following three equations (65)

- Hooke's law
- Darcy's law
- Mass conservation

The Biot's theory is formulated based on the following hypothesis: isotropy of the material, reversibility of stress strain relation, small strain, the fluid inside the pores is incompressible, linearity of the stress-strain and the flow through the porous matrix flow according to the Darcy law. (66)

However, Darcy's law fails to account for viscous stresses at the interface between the solid and liquid phases, which is crucial for studying the CSF and spinal cord interaction in the context of CM1. While Darcy's law is suitable for applications involving only a porous region, its mathematical assumptions become invalid when a fluid domain is connected to it since it cannot consider viscous stresses accurately. Additionally, it does not provide a good approximation at the fluid/solid interface. (66)

On the other hand, Brinkman's equations are an extension of the Navier-Stokes equations and Darcy's law, allowing for a continuous velocity and pressure field at the interface of the two domains. (67)

7.1.2 Equation for fluid description

Fluid flow is described using the Navier-Stokes equation. Given the low Reynolds numbers involved, the convective term can be neglected, resulting in the following simplified equation:

$$\rho \frac{\partial \vec{v}}{\partial t} = \nabla \cdot \left[-\vec{P}I + \mu(\nabla \vec{v} + (\nabla \vec{v})^T)\right] + \vec{F} \qquad (7.1)$$

By employing the theory of hydrodynamics and considering the impact of porous material permeability on fluid flow and pressure, Darcy's law can be derived from the Navier-Stokes equation. The formulation of Darcy's law is as follows

$$\overrightarrow{v_d} = -\frac{k}{\mu} \nabla \cdot \vec{P} \qquad (7.2)$$

In this equation, $\overrightarrow{v_d}$ is the Darcy velocities (SI unit:$\frac{m}{s}$), k is the permeability of the porous medium (SI unit: m^2); μ is the fluid's dynamic viscosity (SI unit: *Pa s*); p is the pore pressure (SI unit: *Pa*) and ρ is the density of the fluid (SI unit: $\frac{Kg}{m^3}$).

However, as before mentioned, this formulation is valid only when there is no fluid domain connected to the porous zone. Hence, for the purposes of this thesis, introducing Brinkman's equation becomes necessary.

To include the effect of viscous shear stress, porosity factor, and neglect inertial terms in the Navier-Stokes equations, the following formulation of Brinkman's equation is used in COMSOL Multiphysics® (59):

$$\frac{\rho}{\epsilon_p}\frac{\partial \overrightarrow{v_d}}{\partial t} = \nabla \cdot \left[-\vec{P}I + \frac{\mu}{\epsilon_p}(\nabla \overrightarrow{v_d} + (\nabla \overrightarrow{v_d})^T) - \frac{2\mu}{3\epsilon_p}(\nabla \cdot \overrightarrow{v_d})I\right] +$$
$$-\left(\frac{\mu}{k} + \beta_f|\overrightarrow{v_d}| + \frac{Q_m}{\epsilon_p^2}\right)\overrightarrow{v_d} + \vec{F} \qquad (7.3)$$

In the equation the terms Q_m (SI unit $\frac{kg}{m^3 s}$) is a mass source added to the Darcy's equation to account for mass deposit in the porous domain. The β_f is the Forcheimer Drag coefficient (SI unit $\frac{kg}{m^4}$), and ϵ_p and k are respectively the porosity and the permeability which are derived from the coefficient used in the Darcy law. Since, in this thesis the CSF is modelled as an incompressible fluid the viscous term present in the equation:

$$-\frac{2\mu}{3\epsilon_p}(\nabla \cdot \overrightarrow{v_d})I \qquad (7.4)$$

Can be neglected leading to the following reduced formulation of the equation *(7.3):*

$$\frac{\rho}{\epsilon_p}\frac{\partial \overrightarrow{v_d}}{\partial t} = \nabla \cdot \left[-\vec{P}I + \frac{\mu}{\epsilon_p}(\nabla \overrightarrow{v_d} + (\nabla \overrightarrow{v_d})^T)\right] - \left(\frac{\mu}{k} + \beta_f|\overrightarrow{v_d}| + \frac{Q_m}{\epsilon_p^2}\right)\overrightarrow{v_d} + \vec{F} \quad (7.5)$$

7.1.3 Equation for solid description:

When examining the solid material model, we can envision a cube made of porous material filled with fluid in a Cartesian coordinate system (x, y, z).

This element is assumed to be large enough compared to the size of the pores, allowing us to treat it as a homogeneous entity. At the same time, it is small enough compared to the macroscopic phenomena we are interested in, enabling us to consider it infinitesimal in mathematical analysis.

This cube can experience both normal and tangential stresses, as depicted Figure 51. In the case of a linear elastic and isotropic material, the relationship between stresses and deformations is described by Hooke's law.

Figure 51: Stresses in a cubic solid element in a 3D Cartesian system

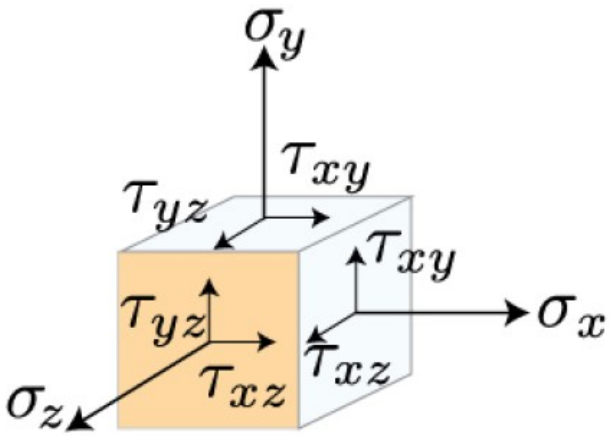

In his theory, Biot added a term which accounts for the contribution of the fluid pressure. Hence, the deformations in the solid element are expressed by the following equations: (65)

$$e_x = \frac{1}{E}\left(\sigma_x - v\left(\sigma_y + \sigma_z\right)\right) + \frac{P_x}{3H} \quad (7.6)$$

$$e_y = \frac{1}{E}\left(\sigma_y - v(\sigma_x + \sigma_z)\right) + \frac{P_y}{3H} \quad (7.7)$$

$$e_z = \frac{1}{E}\left(\sigma_z - v\left(\sigma_y + \sigma_x\right)\right) + \frac{P_z}{3H} \quad (7.8)$$

$$\gamma_{xy} = \frac{\tau_{xy}}{G};\ \gamma_{yz} = \frac{\tau_{yz}}{G};\ \gamma_{xz} = \frac{\tau_{xz}}{G} \qquad (7.9)$$

Where E, v , and G are respectively Young's modulus, the Poisson ratio, and the shear modulus. P is the fluid pressure, H is a physical constant that measures the compressibility of the block related to the change in water pressure. σ_i and τ_{ij} are the normal and shear stresses in the three orthogonal directions. Meanwhile, e_i and γ_{ij} are the components of the strain field. The displacement field and strains are related by the following equations:

$$e_x = \frac{\partial u}{\partial x};\ e_y = \frac{\partial v}{\partial y};\ e_z = \frac{\partial w}{\partial z} \qquad (7.10)$$

In previous equations, there are four unknown parameters: the fluid pressure P, and the displacement components along the three directions (*u, v, w*). Therefore, another equation must be considered in order to solve the poroelastic problem. Assuming the incompressibility of the fluid, the volume of water entering per second of unit area must be equal to the volume of water entering per second through the surface of the element:

$$\frac{\partial \Theta}{\partial t} = -(\frac{\partial v_x}{\partial x} + \frac{\partial v_y}{\partial y} + \frac{\partial v_z}{\partial z}) \qquad (7.11)$$

In the equation above is Θ the increment in time of the water content. From equations *7.4, 7.6, 7.7, 7.8* and *7.11,* the following four equations describing poroelasticity behaviour can be derived. (68)

$$k\nabla^2 P = \alpha \frac{\partial \vec{\varepsilon}}{\partial t} + \frac{1}{Q}\frac{\partial \vec{P}}{\partial t} \qquad (7.12)$$

$$G\nabla^2 u + \frac{G}{1-2v}\frac{\partial \vec{\varepsilon}}{\partial x} - \frac{\partial \vec{P}}{\partial x} = 0 \qquad (7.13)$$

$$G\nabla^2 v + \frac{G}{1-2v}\frac{\partial \vec{\varepsilon}}{\partial y} - \frac{\partial \vec{P}}{\partial y} = 0 \qquad (7.14)$$

$$G\nabla^2 w + \frac{G}{1-2v}\frac{\partial \vec{\varepsilon}}{\partial z} - \frac{\partial \vec{P}}{\partial z} = 0 \qquad (7.15)$$

Q is the quantity of fluid that can be forced into the porous material while the porous medium volume is constant and the Biot coefficient α is defined as:

$$\alpha = \frac{2(1+v)G}{3(1-2v)H} \tag{7.16}$$

In the studied situation, it is possible to assume that no air is present inside the fluid phase. This assumption led to consider $Q = \infty$ and $\alpha = 1$. Therefore, the equation 6.12 can be reduced and expressed as a function of the velocity field leading to:

$$\rho \nabla \overrightarrow{v_d} = \rho \frac{\partial \vec{\varepsilon}}{\partial t} \tag{7.17}$$

The conservation of the fluid mass is affected by its interaction with the solid. Effects on the fluid pressure can be produced by the deformation of the solid. To couple the solid and the fluid physics a two-way coupling system is necessary. The effect of the solid deformation on the fluid mass conservation is expressed in equation 7.17. Vice-versa the influence of the fluid pressure gradient on the solid is present in the equations governing the mechanical movement of the solid (eq. 7.13, 7.14, 7.15).

In order to recreate the theory of poroelasticity in COMSOL Multiphysics, two couplings' terms are added to Brinkman's equation, Darcy's law and structural mechanics equation. A source mass term Q_m condition is added to the spinal cord region in order to link the contribution of the solid in the Brinkman's equation and Darcy's equation. The source mass term accounts for the time rate of expansion of the solid matrix. This term is defined by the following equation

$$Q_m = -\rho \cdot \frac{\partial \vec{\varepsilon}}{\partial t} = -\rho \cdot \frac{\partial}{\partial t}\left(\frac{\partial u}{\partial x} + \frac{\partial v}{\partial y} + \frac{\partial w}{\partial z}\right) \tag{7.18}$$

When there is an expansion of the porous matrix, the volume fraction available for liquid will increase and thereby give rise to liquid inflow, which is why the sign is reversed in the source term. While a body force is integrated in the structural mechanics physics expressed in three volume forces acting in the three directions to take into account the effect of the fluid over the solid.

$$F_{vx} = -\frac{\partial \vec{P}}{\partial x};\ F_{vy} = -\frac{\partial \vec{P}}{\partial y};\ F_{vz} = -\frac{\partial \vec{P}}{\partial z}; \tag{7.19}$$

7.2 FSI STUDY HEALTHY CONDITIONS

The objective of this simulation is to conduct a FSI simulation without the presence of an obstruction. Two simulations were performed:

- One simulation without the inclusion of the Pia Mater.

- One simulation with the presence of the Pia Mater.

The primary focus of these simulations was to examine the differences between the two types of approach: FSI and CFD simulation and assessed difference in the result with and without the Pia mater.

7.2.1 Geometry and Material

The geometry that has been used for the FSI coupling, is the same cropped geometry that has been used for the CFD study in the chapter 6. In this case a new domain has been added to take into account the spinal cord region. In the setup with the presence of Pia Mater a 'Thin Elastic Layer' has been added around the spinal cord domain. The pia mater can be defined as a linear elastic material and a thickness between 8µm and 15µm (55). A mean value of 11.5 µm has been considered for the pia mater. The geometry of the spinal cord is represented in Figure 48cord is represented in Figure 48.

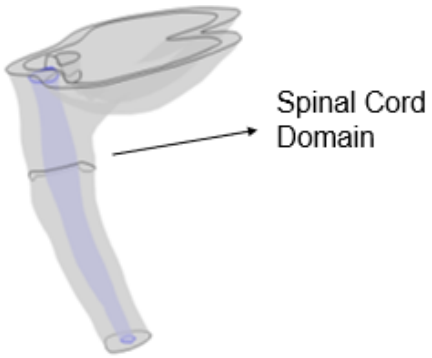

Figure 52: Introduction in the geometry of the spinal cord domain

Further, the material proprieties are based on the studies carried out by Bertram et al. (53) which consider the matrix of the poroelastic material as linearly elastic with isotropic mechanical proprieties. Moreover, no pre-stresses have been taking into account. The material proprieties are summarized in Table 9.

MATERIAL	Density [kg/m^3]	Dynamic Viscosity [Pa*s]	Porosity (-)	Permeability [m^2]	Poisson Ratio [-]	Elastic Modulus [Pa]
Cord	1000	7e-4	0.3	1E-13	0.35	5000
Water	1000	1e-3	/	/	/	/
PIA mater	1000	/	/	/	0.49	1250000

Table 9: Material properties used in setup 1, derived from Bertram et al. (53)

7.2.2 Generation of the mesh

The mesh has been built using the COMSOL Multiphysics tools user-controlled mesh using the type of element described in the CFD simulation:

- A boundary layer around the spinal cord surface containing prismatic elements
- Tetrahedral elements for the remain volumes

	MESH 1	MESH 2	MESH 3
Elements	15035	58204	108123
Minimum quality	0.0086	0.01302	0.02504
Average quality	0.5361	0.605	0.6415

Table 10: Different meshed used for the mesh sensitive analysis

The three different cases have been evaluated using equation 1 (section 5.2.2), calculating the % error between the different meshes. From Figure 53, we can observe that the % difference between meshes 1 and 2 is large (4.23%), the % difference between mesh 2 and 3 significantly reduced (0.89%). To reduce the computational burden, the mesh 2 has been chose.

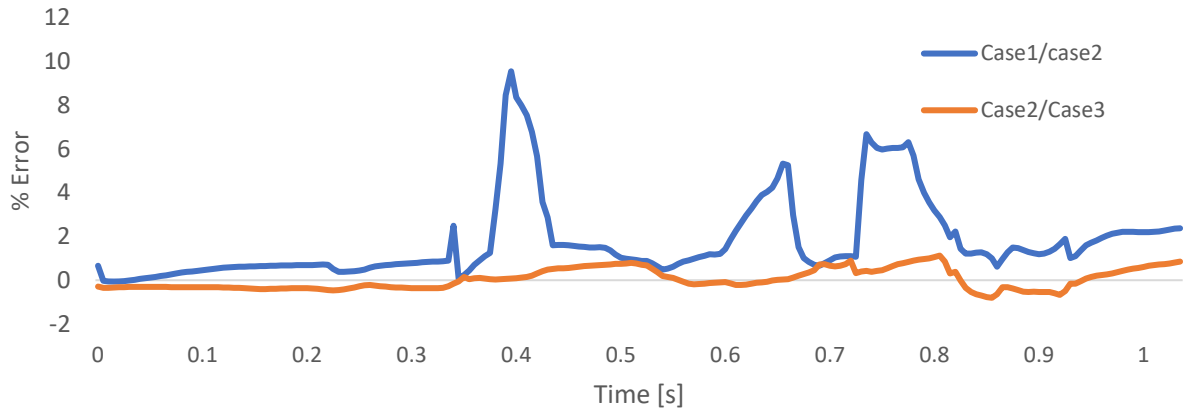

Figure 53: % error between the different mesh used for the mesh sensitive analysis

7.2.3 Boundary conditions

The inlet boundary conditions are the same as those that have been utilized in the CFD simulations, as shown in Figure 54. The outlet pressure has been chosen to be 10 mmHg, which is in the line of the average intracranial pressures. An average pressure of 0 mmHg would lead to the pressure value crossing and dropping below zero during the simulation, which would cause suction in an FSI simulation which is not physiological. Mechanically, the spinal cord is to fixed both at the bottom and upper end. The surface between the spinal cord and SAS acts as a fluid-structure interface, and the deformations of the solid material are fully coupled with the pressures in the fluid domain.

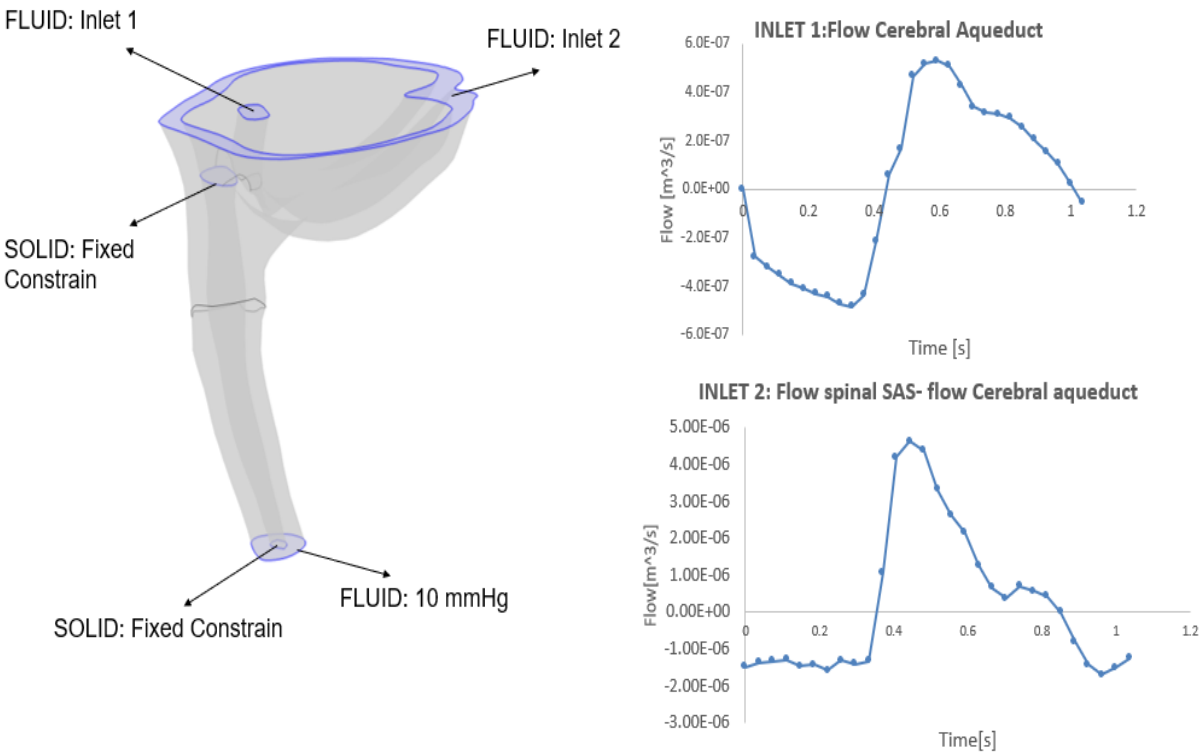

Figure 54 Overview of solid mechanics boundary condition and fluid boundary condition

7.2.4 Solver Setting

The 3D model consists in two domains: the fluid and the poroelastic domain, which are modelled with the following COMSOL Multiphysics settings:

- Free and Porous Media Flow
- Solid Mechanics

As mentioned in the formulation of the poroelasticity, within the poroelastic domain free and porous media flow and solid mechanics are coupled with a body force term acting on the solid and the mass source term acting on the fluid.

As in the CFD simulation 1 cardiac cycle has been considered and an adaptative time-stepping has been used with the minimum timestep size of 0.005. In order to improve the convergence of the simulation a moving mesh is used for the CSF domain. This COMSOL Multiphysics (COMSOL Inc.) tool is generally used when the geometry changes its shape due to dynamics problem, in this case due to the deformation of the spinal cord To solve the simulation the 'Fully Coupled' approach has been used. This approach considers a large system of equations of the different physical phenomena involved which are solved within a single iteration take into account their mutual influence on each other. The algorithm that has been used to solve the linear system of equation is the PARDISO algorithm.

7.2.5 Results

The purpose of this section is to assess the impact of including the PIA mater in the model and understand its effects. Similar to the approach in the previous chapter, the maximum velocities within the spinal SAS were evaluated.

Figure 55 displays the maximum velocities within the spinal SAS. From the illustration, it's evident that there are no significant differences in the magnitude of the two simulations. The conclusion drawn is that the simulated velocities of the model without the PIA mater exhibits a delay compared to the velocity waveform corresponding to the model with the PIA included. This delay is approximately 0.017 seconds, calculated by measuring the time difference between the two peaks during systolic pressure and the minimum values before the systolic peak, and then averaging these two values.

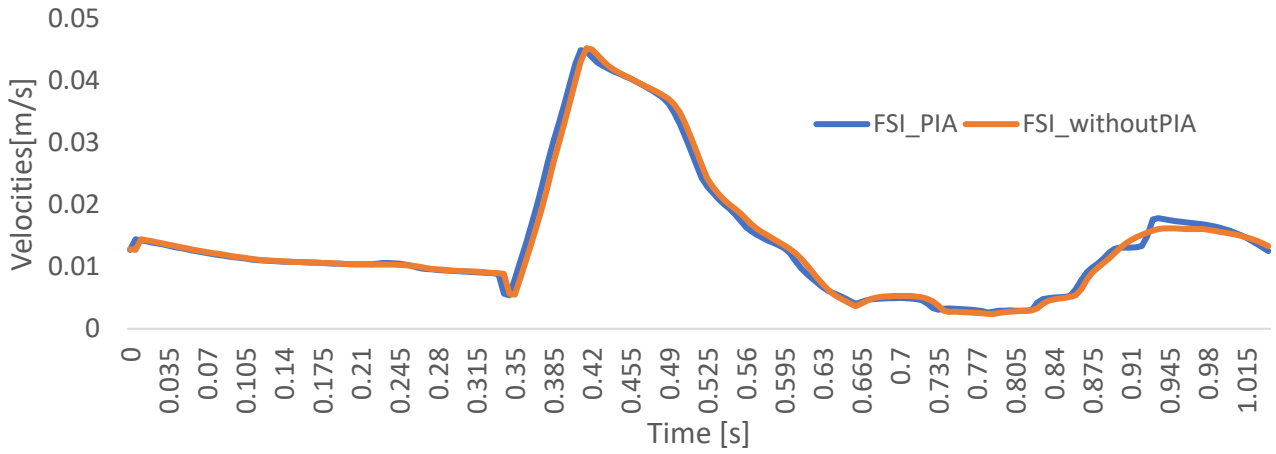

Figure 55: Maximal velocities evaluated at the plane of obstruction considering the effect of the PIA mater

Figure 52 depicted the pressure drops between the cerebral aqueduct and the plane below the obstruction in the simulation with the PIA and the one without. As shown in figure 52, there are minimal alterations in pressure between the simulations with and without the PIA.

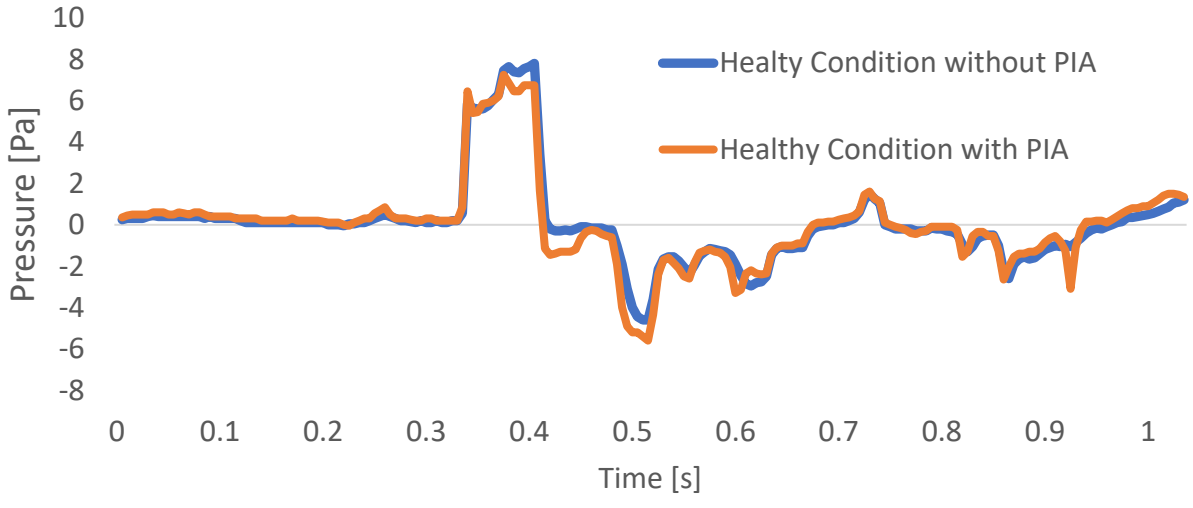

*Figure 56:*Pressure drops between the cerebral aqueduct and the average of two point in the plane at the below the obstruction

Finally, the volume change over time of the spinal cord has been evaluated. The volume change is difference between the instantaneous volume and the initial volume of one compartment domain. This is to evaluate see if the presence of the pia mater induce change in the fluid entering or leaving in the spinal cord. The formula to calculate the spinal cord volume difference is depicted below

$$Volume\ diff = Volume(t) - Volumet_0$$

The volume exchange in the spinal cord is at the order of millimetres. It appears that, during the period in which there is the peak in flow imposed by the boundary condition, there is an increase in the volume exchange. From the Figure 57, it's difficult to draw conclusions since the plot has a high variance probably due to the limited resolution of the simulation.

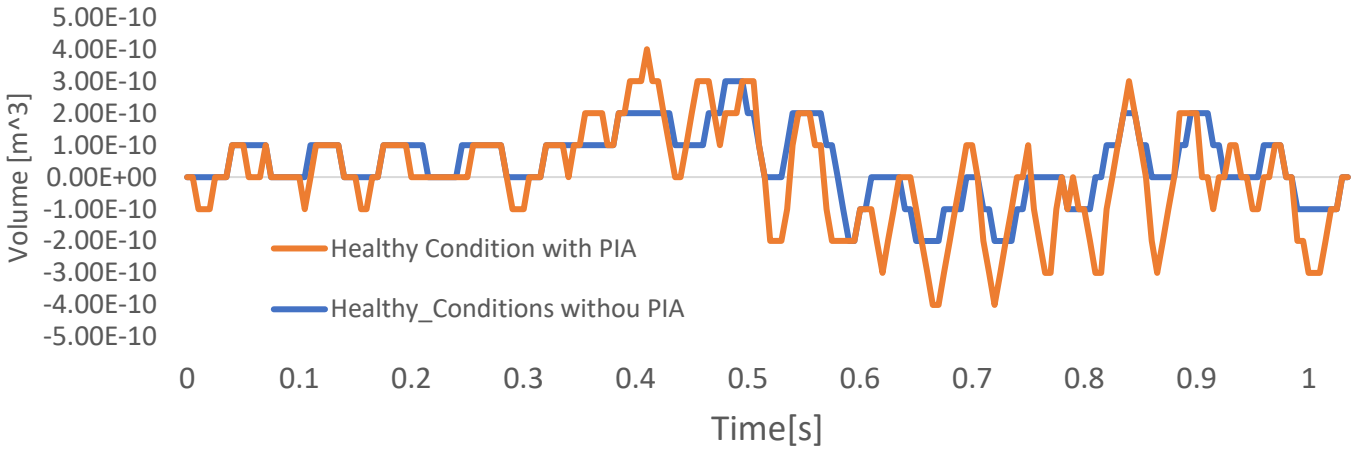

*Figure 57:*Spinal cord volume difference during the cardiac cycle

7.2.6 Discussion

The objective of this section was to present the FSI poroelastic method within the context of a healthy condition arrangement and to assess how the presence of the PIA mater impacts the simulation. The findings indicate that the presence of the PIA mater doesn't influence the magnitude of velocities and pressure. However, it does seem to cause a delay in the waveform of velocity. This delay is likely attributed to the thin layer simulating the PIA mater, which have a Young's modulus of 1250000. This layer appears to render the spinal cord more rigid, thereby enhancing the velocity propagation.

7.3 FSI STUDY WITH THE OBSTRUCTION CONDITIONS

The aim of this chapter is to gain more insight into the effect of the presence of the obstruction by considering the mechanical response of the spinal cord in an FSI simulation and then comparing the results obtained assuming rigid walls in the CFD simulation.

As done in the previous chapter for the CFD simulation three degrees of obstruction have been considered:

- An obstruction of 40% with the same ellipsoid used in the CFD simulation. The obstruction domain is considered as a porous domain.
- An obstruction of 60% with the same ellipsoid used in the CFD simulation. The obstruction domain is considered as a porous domain.
- An obstruction of 100% with the same ellipsoid used in the CFD simulation. The obstruction domain is considered as a porous domain.

7.3.1 Geometry and Material

The setup described in section 7.2 is used as a baseline for the three simulations with the obstruction using the same geometry and the same materials. As depicted in Figure 58, the same two obstructions used for the CFD model are added.

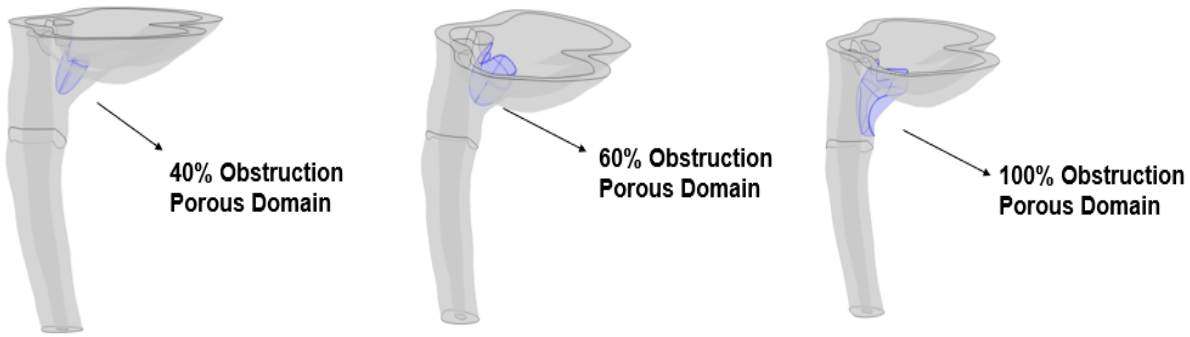

*Figure 58:*Representation of the porous domain corresponding to the CM1 herniation

Regarding the material used to simulate the herniation porous domain presents the same permeability and porosity used for the spinal cord. Respectively, 1E-13 m^2 and 0.3.

7.3.2 Generation of the mesh

Due to the hight computational cost to run a sensitive analysis of all the simulations, the mesh sensitivity analysis has been carried out only in the case without the obstruction. Thus, based on mesh sensitive analysis carried out in section 7.2.2 only the 40% and 60% level of obstruction has been carried out with the finer mesh (mesh 3) while the 100% of obstruction with the less fine mesh (mesh 2) due to the hight computational demand of the poroelastic FSI approach.

7.3.3 Boundary conditions

The boundary condition that has been used for this simulation are the same that has been used in the chapter of FSI simulation without the obstruction:

- Fluid boundary condition: at the region corresponding to the cerebral aqueduct the PCMRI flow has been applied and the difference between the PCMRI flow evaluated at the spinal SAS c2 minus the

flow in the evaluated at the cerebral aqueduct has been applied at the other inlet condition. An outlet boundary condition of 1333.2 Pa has been applied. (Same as in the CFD model)

- Solid mechanics boundary condition: the upper and the lower part of the spinal cord has been fixed with a zero displacement. (Same as in the FSI without the obstruction)

In the simulation with 100% of obstruction there is an overlap between the porous zone simulating the herniation and the poroelastic domain of the spinal cord. In order to be able to run the simulation the interface between the two domains has been keep fixed has shown in Figure 59

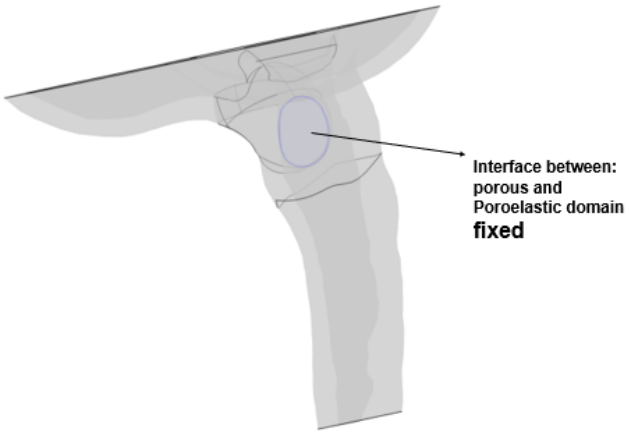

Figure 59 : Representation of the fixed region between the porous and the poroelastic domain

7.3.4 Result

The velocity contours shown in Figure 60 depicts the sagittal plane velocities at the systolic peak, occurring at 0.44 seconds for 40% 60% 100% of obstruction. In the absence of obstruction (healthy condition), the highest velocities are observed at the lower segment of the spinal SAS. However, when obstruction is considered in the simulation, the maximum velocities are concentrated around the middle part of the cervical spinal SAS as reported in the study conducted by Linge et al (LINGE) and how reported in the previous chapter (section 6.4). Under healthy conditions, these maximum velocities reach 47 mm/s. With the presence of obstruction, these velocities increase and remain relatively consistent even with greater levels of obstruction, reaching 64 mm/s.

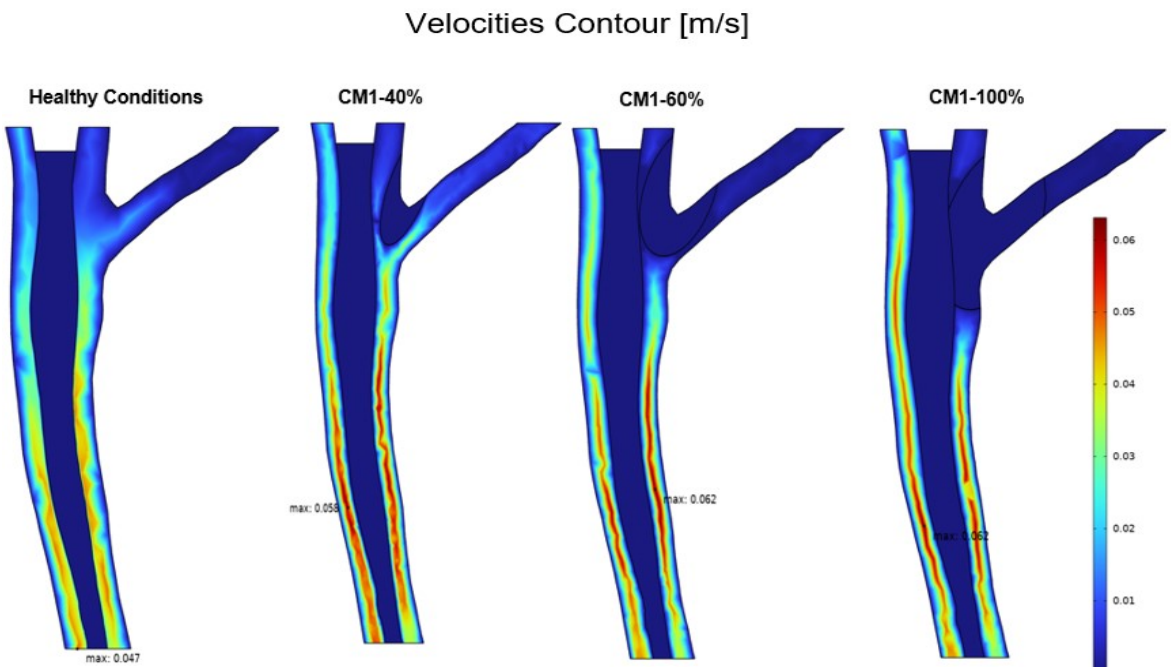

Figure 60:Velocities contour at the sagittal plane during the systolic peak at 0.44s

The Figure 61 illustrates the sagittal plane velocity contours at 0.85s. In cases where obstruction exists, there is a reduction in velocities, and the maximum velocity is situated in the upper region of the obstruction. Conversely, in the absence of obstruction, the maximum velocity is found in the lower region, measuring 10 mm/s. With obstruction, these maximum velocities decrease to 6.8 mm/s, 7.4 mm/s, and 8.9 mm/s for obstruction levels of 40%, 60%, and 100% respectively.

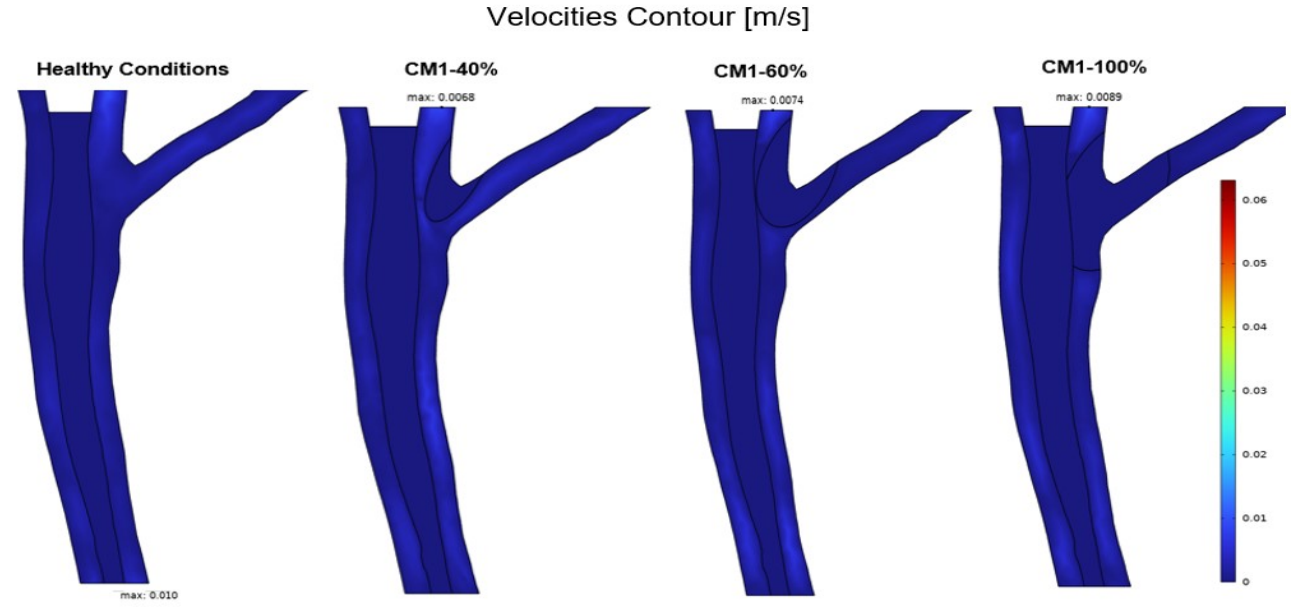

Figure 61: Velocities contour at the sagittal plane during the systolic peak at 0.85s

To further explore the impact of obstruction in the FSI simulation, the same transversal cross-section of the CFD analysis at the level below the obstruction was taken for evaluation of maximal velocities.Figure 59

illustrates the maximal velocities throughout the cardiac cycle, assessed in the plane below the obstructio Notably, at the level of the spinal SAS, the influence of herniation is evident, with velocities gradually increasing from the healthy condition (35 mm/s) to 100% obstruction (57 mm/s). It's challenging to distinguish significant velocity differences between 40% and 60% obstruction. In these cases, velocities roughly reach 48 mm/s.

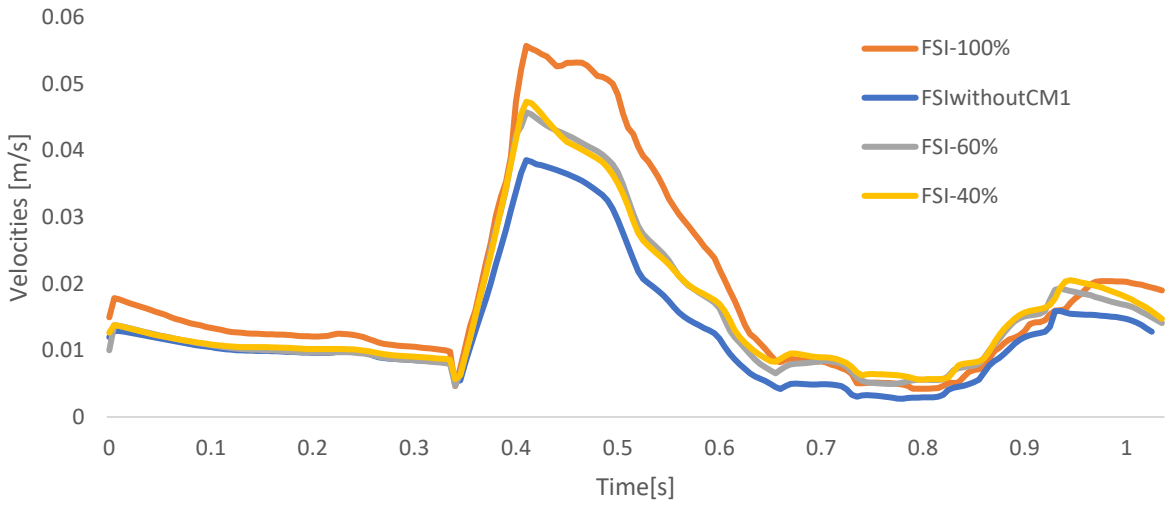

Figure 62: Maximal velocities along the cardiac cycle with the different level of obstruction in the spinal SAS c2

The Figure 63 illustrates velocity contours in the plane below the obstruction at 0.44s. In the healthy condition, velocities are uniformly distributed across the spinal SAS section. However, with increasing obstruction, the flow distribution becomes non-uniform. Notably, in the case of 100% obstruction, the high-velocity area is only present in the section without obstruction in the area corresponding to the Pontomedullary. Inside the spinal cord, velocities are approximately 10^-8 m/s, while in the SAS, they are around 10^-3 m/s, suggesting that a significant portion of the flow passes through the SAS rather than entering the spinal cord.

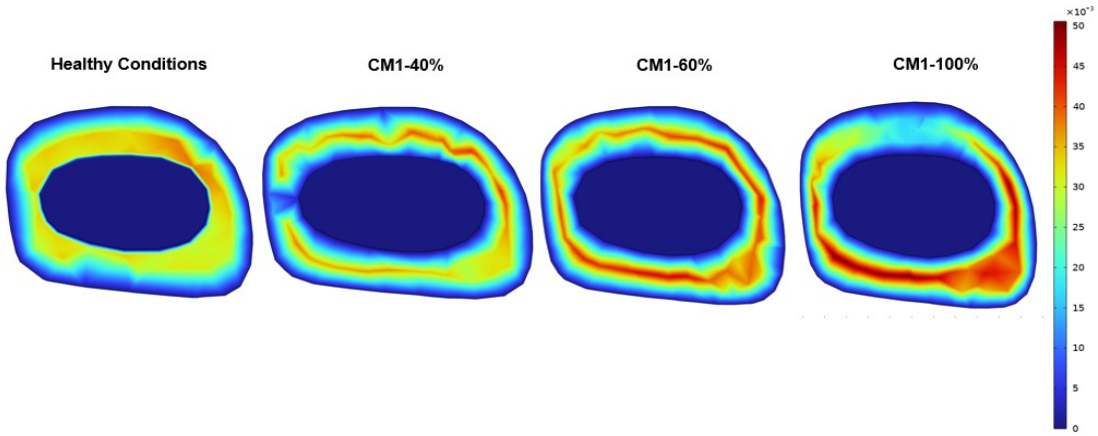

*Figure 63:*Contour velocities along the cardiac cycle with the different level of obstruction in the plane below the obstruction

The maximal velocities at the herniation level were evaluated. The Figure 64 indicates a clear effect of herniation, with velocities increasing as obstruction levels rise. At 100% obstruction, the maximal velocity reaches 52.12 mm/s, more than double that of the healthy condition. Obstructions of 40% and 60% seem to have a relatively minor impact on maximal flow velocities.

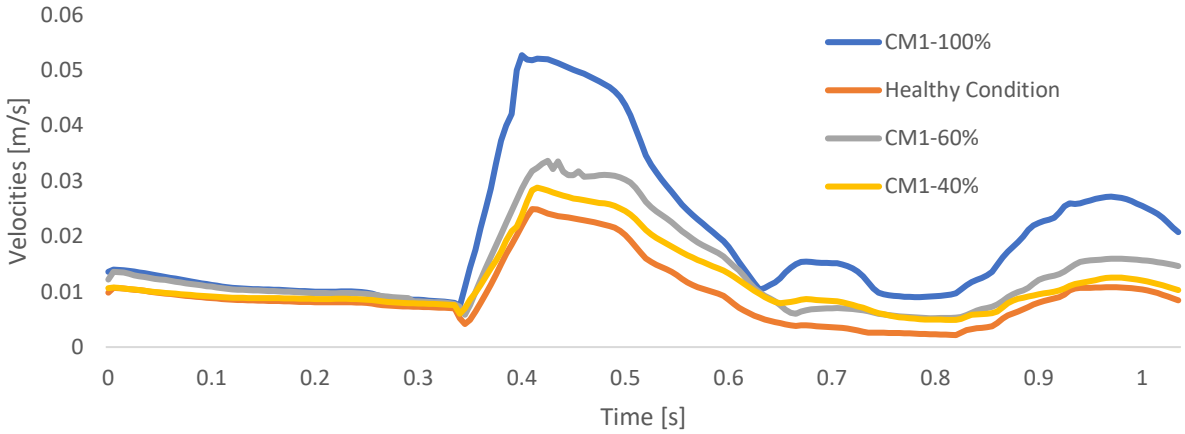

*Figure 64:*Maximal velocities along the cardiac cycle with the different level of obstruction at the level of the obstruction

Velocity contours at the herniation level are plotted in Figure 65. In the healthy condition, the flow is uniformly distributed in the geometric section, a trait that persists in the 40% obstruction scenario. However, there is a greater slowdown in the back part of the spinal cord with the 60% and the 100% of obstruction.

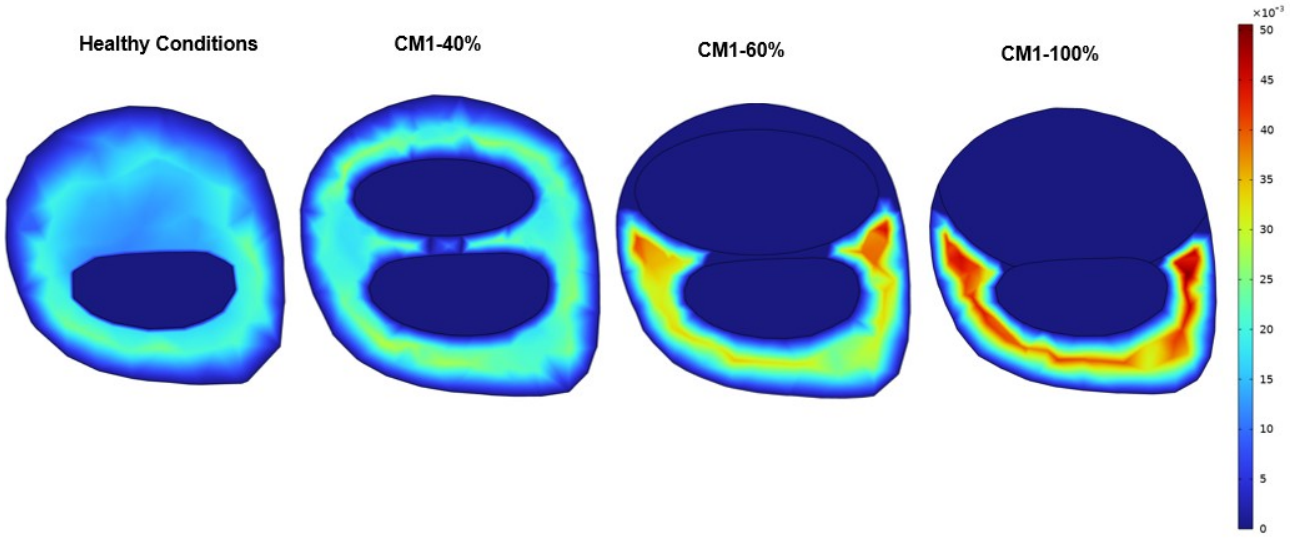

Figure 65 Contour velocities along the cardiac cycle with the different level of obstruction at the level of the obstruction

Figure 66 illustrates the maximal velocities at the plane below the obstruction and at the plane at the level of the herniation with the difference level of obstruction. Velocities are heightened in both cross sections, with a particularly noticeable rise evident in the simulation with 100% obstruction, specifically when observing the herniation level. What becomes apparent is that there is a nonlinear increase in velocities at

the level of the obstruction. However, when looking at the plane below the obstruction (spinal SAS c2), there is not a significant effect on velocities due to the increased level of obstruction

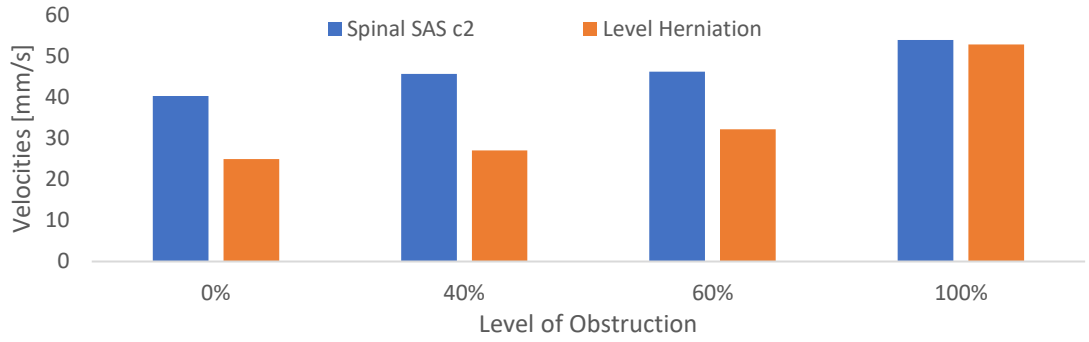

Figure 66: Diagram representing the maximal velocities in the spinal SAS and at the level of the herniation during the systolic peak

The pressure drop occurring between the cerebral aqueduct and the plane below the obstruction are plotted in Figure 67. The plotted data demonstrates that the pressure drop rises as the obstruction level increases passing from a maximum of 5.5 Pa peaks in the healthy condition to a 26.7 Pa for the 100% of obstruction.

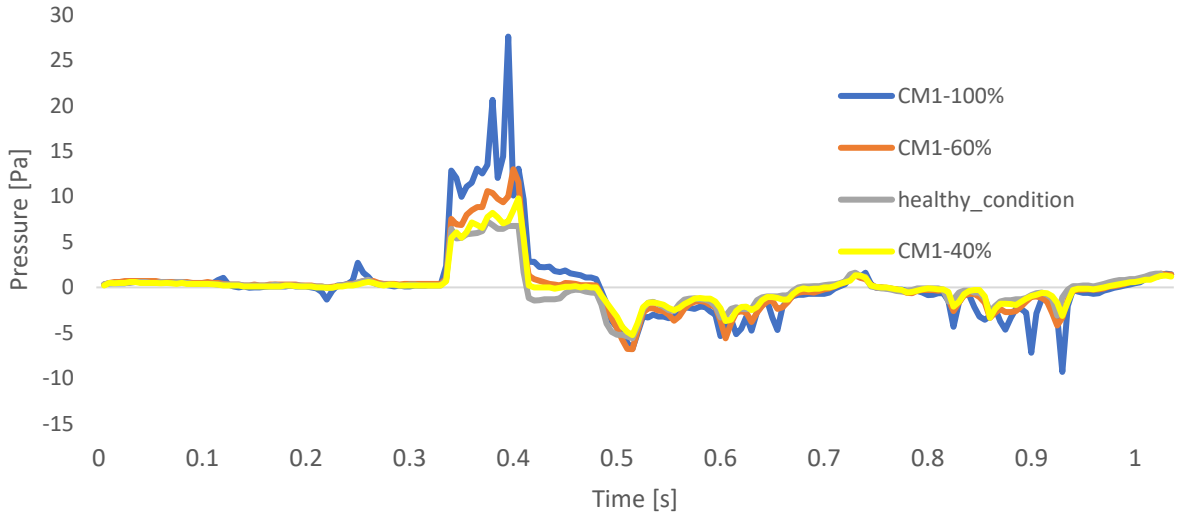

Figure 67:Pressure drops between the cerebral aqueduct and the plane below the obstruction across the cardiac cycle

For a more comprehensive exploration of the impact of herniation on pressure, the pressure distribution contours are depicted in the following Figure 68. Evidently, there is a rise in pressure as obstruction increases, with the highest-pressure levels aligning with the cisterna magna over the herniation. Notably, in the case of 100% herniation, elevated pressure concentrations are situated along the fixed boundary between the spinal cord and the herniation. This configuration represents a non-physiological scenario and poses significant limitation on the 100% setup.

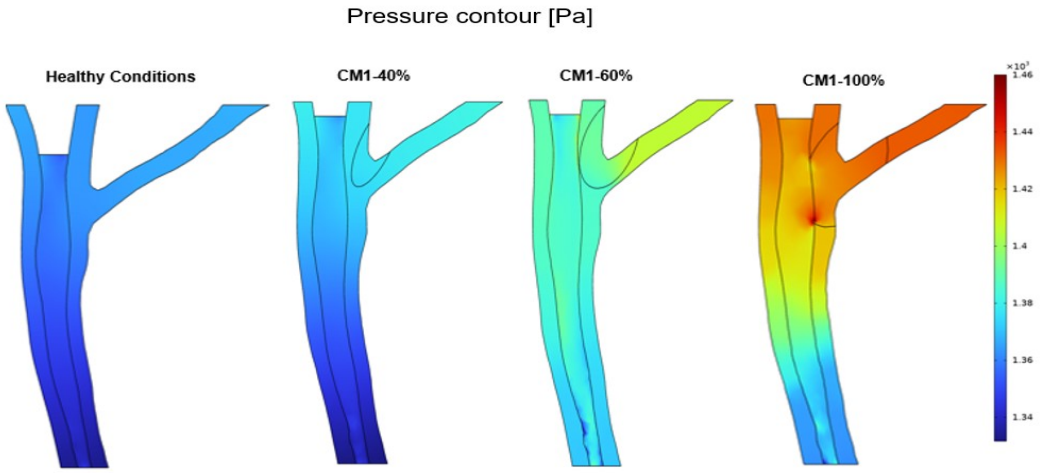

Figure 68: Pressure contour at the sagittal plane during the systolic peak

The aim of this section was to assess whether the heightened level of obstruction leads to altered flow pathways. The figure 65 displays the streamlines of velocities. Observing the Figure 69, it becomes apparent that in proximity to the obstruction, there are localized effects. Although there are minimal differences in the case of 40% obstruction, both 60% and 100% obstructions show an apparent increase in streamlines which suggest that the CM1 herniation can increase have an impact in the flow direction. The Figure 70 highlight the increase number of streamline between the healthy condition and the 60% of obstruction. Notably, the fluid velocity within the spinal cord is in the range of 1e-8 to 1e-7 m/s.

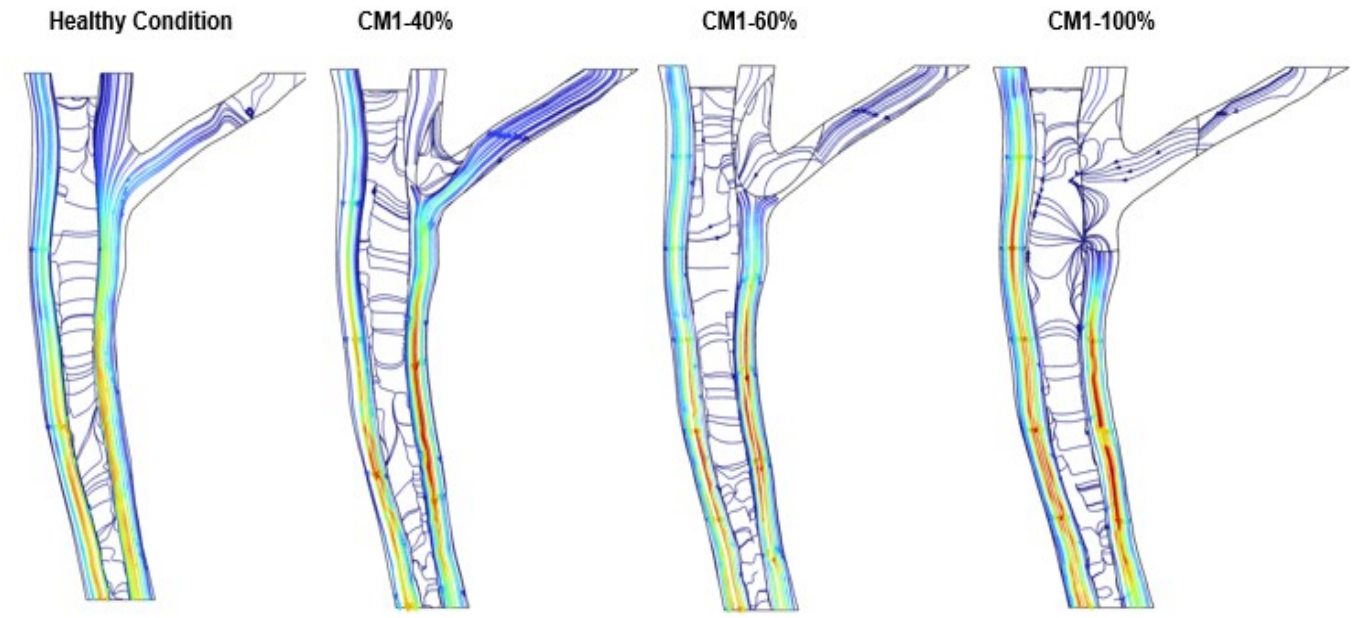

*Figure 69 :*Velocities streamline of the CSF

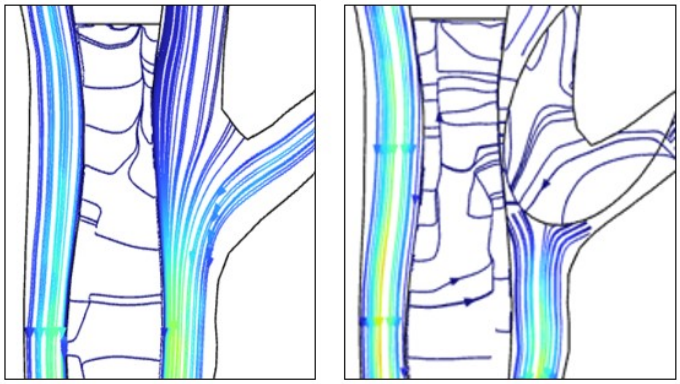

*Figure 70:*Left figure represent the local streamline in the healthy condition while the right figure the local stream line with 60% of obstruction

To further investigate whether the herniation has an impact in the flow inside the spinal cord the flow within the spinal cord is depicted in the Figure 71 and Figure 72. These figures represent the flow inside the spinal cord under the healthy conditions, the 40% of obstruction and the 60% of obstruction respectively at tie points 0.44s (Figure 71) and 0.85s (Figure 72). The 100% of obstruction due to the limitation of the fixed boundary between the spinal cord and herniation has been not consider. From the Figure 71 appears that during at 0.44s, when there is the peak in flow in the spinal SAS, in the healthy condition the velocities are more distribute. However, as obstruction increases, the distribution appears to become less homogeneous, with areas of no flow and areas with higher velocities. At 0.85s the velocities magnitude increases with the increase of the obstruction leading a reduction of the area with low velocities present in the healthy condition. As before underline the velocities inside the spinal cord are on the order of E-8 m/s, suggesting that there is not a proper fluid flow between the SAS and the spinal cord.

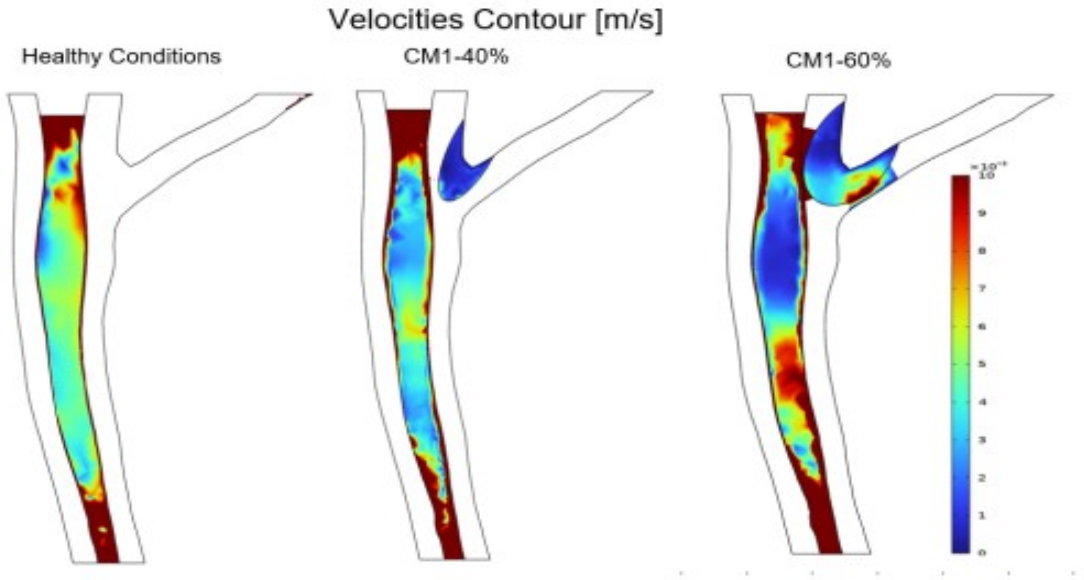

Figure 71: Velocities contour inside the spinal cord at t=0.44s

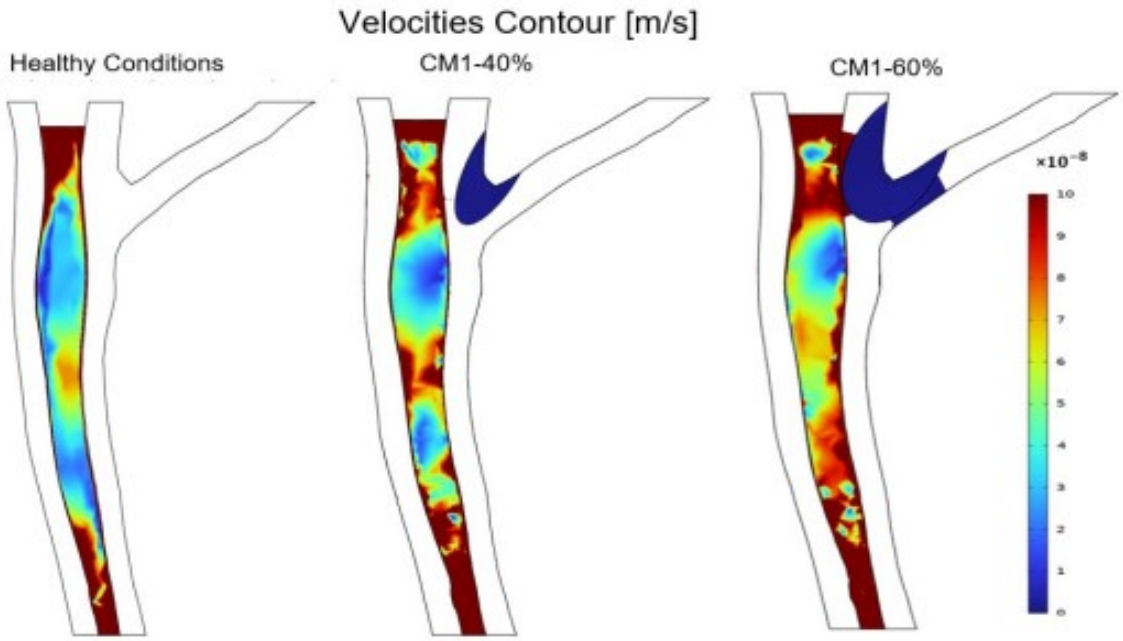

Figure 72: Velocities contour inside the spinal cord at t=0.85s

In order to gain an understanding of the potential for a more pronounced volume difference caused by herniation, the alteration in volume, calculated as the difference between the instantaneous volume and the initial volume, was examined within the spinal cord. The Figure 73 depicts this volume change; however, significant distinctions cannot be discerned due to the substantial variability in the curve. As a result, drawing conclusions from this data is challenging.

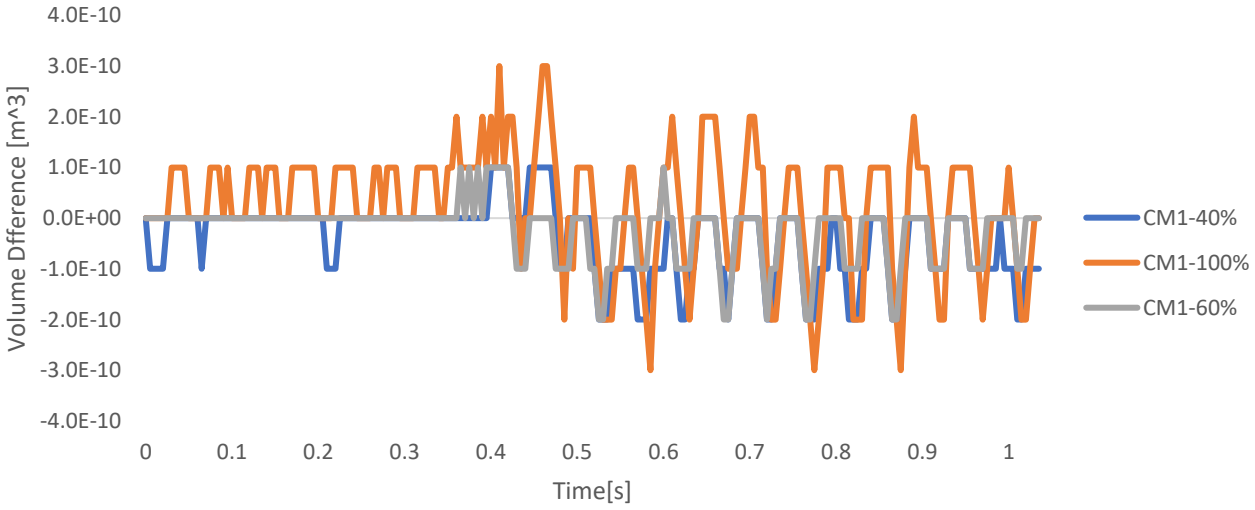

*Figure 73:*Spinal cord volume difference during the cardiac cycle

Concerning the poroelastic properties of the spinal cord, the impact of obstruction appears to alter the overall deformation of the spinal cord. The Figure 74 illustrates, in the first row, the deformation and Von

Mises stress during the systolic peak at 0.44 seconds, and in the second row, the same aspects during the midpoint of the diastolic phase at 0.85 seconds. Also in this case the 100% obstruction is omitted.

In the healthy condition and with 40% obstruction, the deformation seems to exhibit similar behaviour. However, this behaviour changes with 60% obstruction, as the spinal cord moving posterior instead of anterior. The different deformations behaviour in the setup with 60% obstruction is also evident during at 0.85 seconds

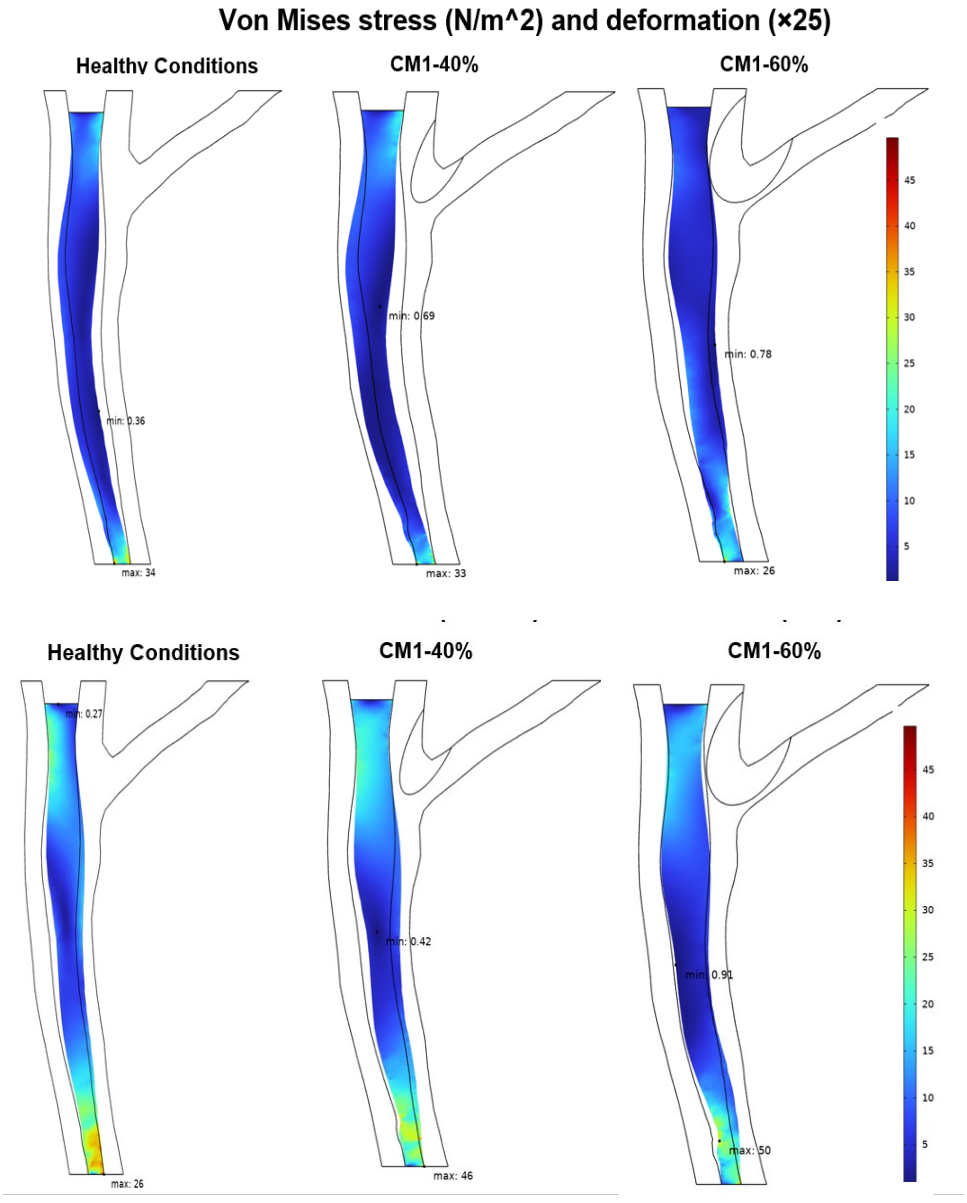

Figure 74: Von Mises stress and relative deformation at 0.44s (first row) at 0.85s (second row)

In order to understand whether the different deformation behaviour and the relative difference in stress distribution may have an impact in the region below the obstruction, the stress distribution has been evaluated in the Figure 75. The figure shows the different behaviour at the time of the at 0.44s for the healthy condition, the 40% of obstruction and 60% of the obstruction. What appear from the picture is that

at 0.44s the healthy condition has the region with the higher stress located on the frontal part of the spinal cord is present while the 60% has the maximal stress present on the back part of the spinal cord. This different behaviour may suggest that the present of the obstruction increase the stress on the spinal cord and this force more CSF through the PIA mater increasing the fluid flow inside the spinal cord

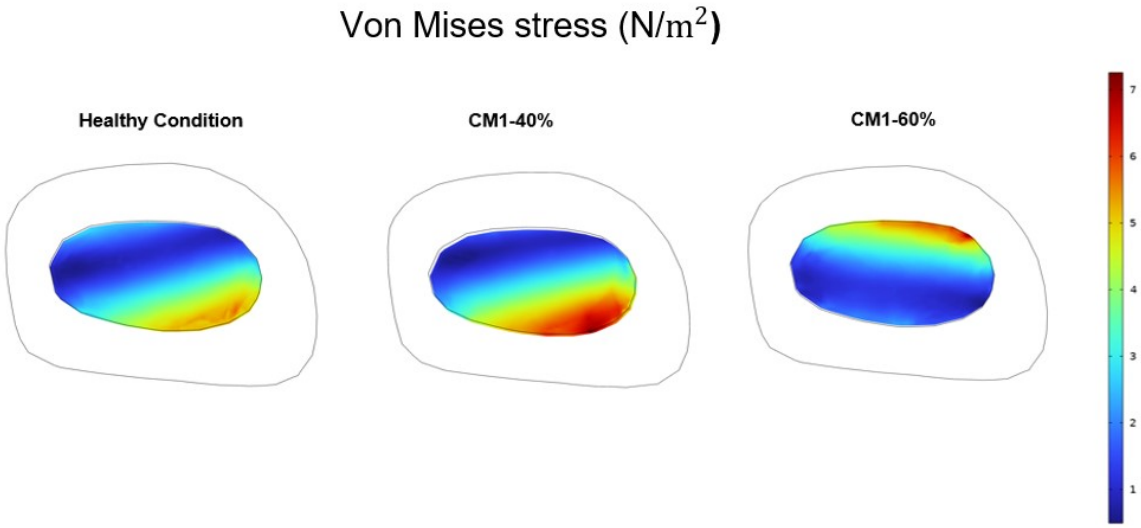

Figure 75: Stress contour at the level below the obstruction

7.3.5 Discussion

The objective of this section is to investigate further into the effects of obstruction within a 3D geometry. In order to enhance the CFD simulation, both the spinal cord and the herniation tissue have been considered, utilizing a Poroelastic formulation based on parameters outlined by Bertan et al. (30)

From the Figure 74, it appears that the presence of CM1 with the 60% obstruction alters the deformation behaviour of the spinal cord throughout the cardiac cycle (spinal cord moves posterior instead of anterior). This possibly influences the overall fluid exchange pattern due to the different stress distribution and might increase the amount of fluid forced through the pia into the spinal cord.

Moreover, Figure 71 and Figure 72 highlights the change in the distribution of the velocities inside the spinal cord showing that with increasing degree of obstruction larger areas with high velocities are noticed. Furthermore, different direction in the velocities streamline is noticed at the 60% of obstruction suggesting that the obstruction has an impact in the flow inside the spinal cord. These result, suggest that the herniation has impact on the flow inside the spinal cord and may enhance the fluid exchange between the spinal SAS and the spinal cord. Nevertheless, no volume difference has been highlighting.

The low velocity inside the spinal cord, underscores the absence of proper fluid flow between the SAS and the spinal cord. It's worth noting that the timescale of the models used in this study might be too short to capture these effects, as clinical cases involve syrinx reduction or growth over months. To observe such

evolution, simulating weeks or months of cardiac cycles would be necessary, as previously indicated by Bertram et al. (53) for the same problem.

The aim of this thesis was also to compare the different CFD and the poroelastic FSI approach

The FSI formulation granted to both consider the interaction between the CSF flow and the deformable wall due to the soft material of the cerebral tissue. Although the added value of considering the brain tissue, due to the high computational burden the FSI approach is not always necessary. The figure 76 represents the maximal velocities of the healthy condition and the 60% of obstruction. The 100% has been omitted to the limitation before described of the fixed boundary between the spinal cord and the herniation and also for the less fine mesh. From Figure 76 we can state that not big difference is present using the CFD approach with rigid wall and the deformable wall using the FSI.

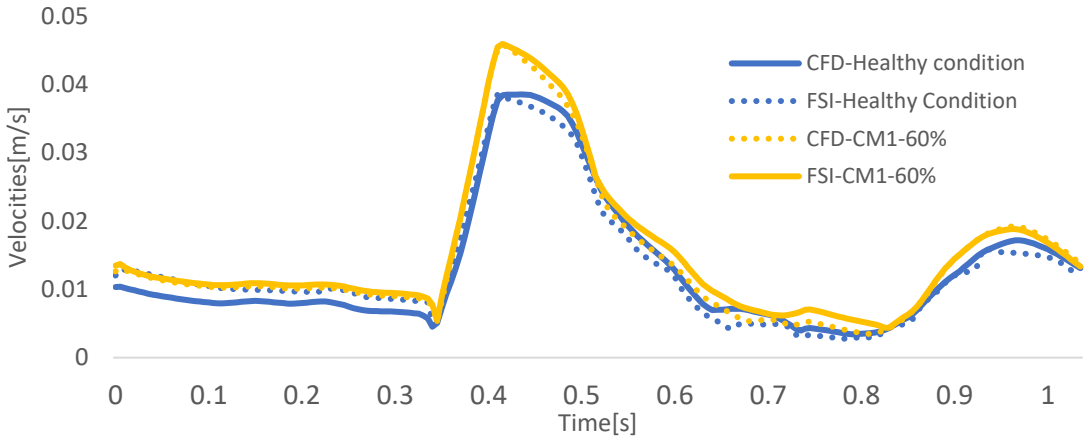

Figure 76:Comparison between FSI and CFD approach, max velocities below the obstruction

Moreover, the maximal velocities obtained in the FSI approach align with those from the previous CFD model, indicating a maximum velocity of 47 mm/s for the healthy condition and 62 mm/s for obstructions of 60% and 40%. These peak velocities are situated in the region in the middle of the cervical spinal cord, consistent with the CFD findings. Looking the velocities at the level of obstruction both in the FSI and CFD approach the influence of obstruction is evident as velocities increase due to obstruction. At the level below the obstruction in the FSI simulation the 40% and 60% obstructions yield equivalent maximal velocities, while a notable increase is observed in the case of 100% obstruction, reaching 52 mm/s. This is in contrast of the result obtained in the CFD simulation where all the level of obstruction has more or less the same velocities waveform. The higher values obtained in the 100% of obstruction can be conducted to the less fine mesh in comparison to the other simulation.

The manifestations of FSI may not be immediately discernible solely by observing velocity patterns, but they become evident upon examining the pressure distribution. The pressure variations between the cerebral aqueduct and the spinal SAS have been graphed in Figure 77 for both the healthy state and the condition with 60% obstruction. In this simulation, it's apparent that the brain tissue does not damp out the pressure

pulse. Consequently, there is no observed reduction in the pressure drop between the cerebral aqueduct and the plane below the obstruction. Overall, the rigid wall CFD approach seems to predict accurately the CFS flow field and the FSI approach does not add value in this study.

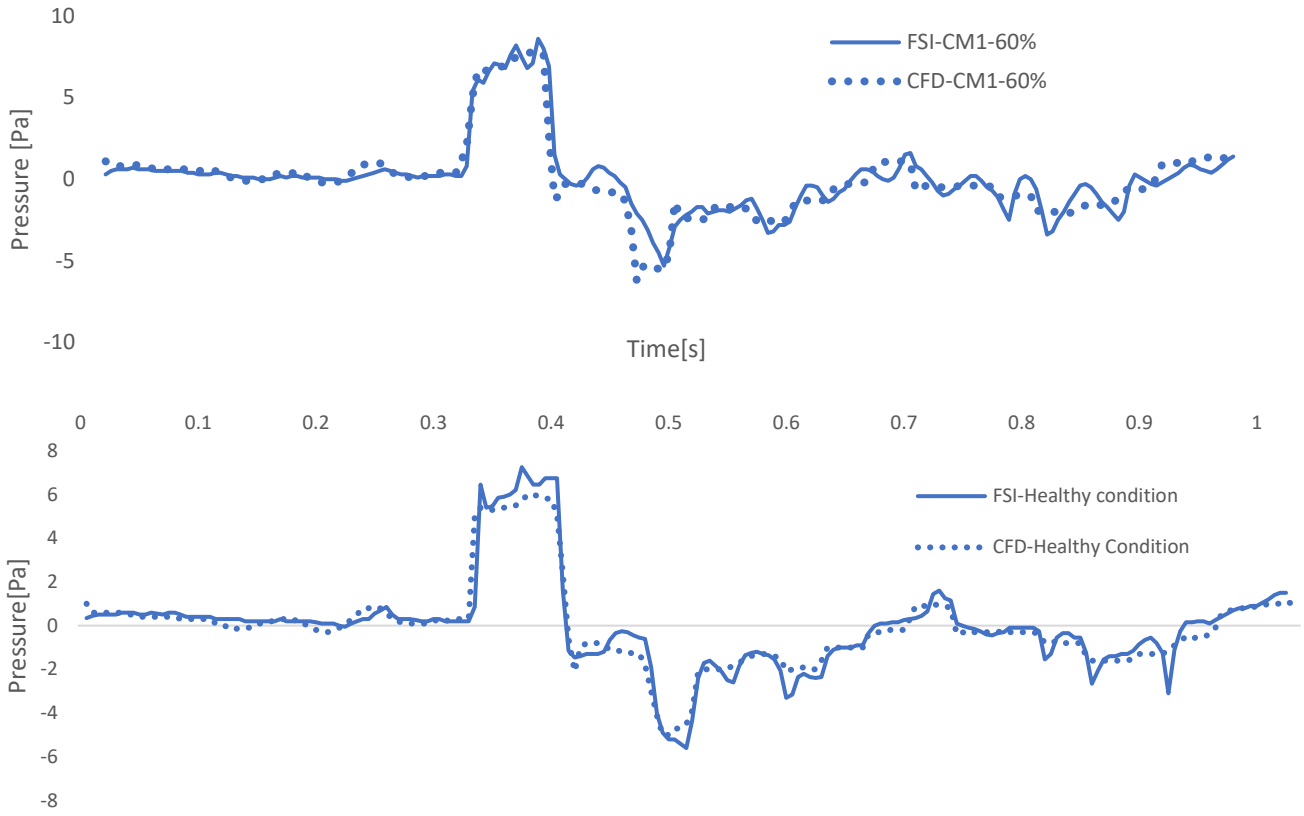

Figure 77: Comparison between FSI and CFD, pressure drop between cerebral aqueduct and spinal SAS c2. First row depicted the healthy condition while the second and the CM1 with the 60%

On the other hand, the utilization of the poroelasticity approach captures insights into the flow dynamics within the spinal cord and proves valuable in comprehending the origins of syrinx development.

In conclusion, the difference in velocities and pressure between the CFD and FSI approach appear to be limited suggesting that an FSI approach might not provide additional information on these parameters.

The outcomes of this study are influenced by several simplifications made during the model development.

The patient specific geometry it's only a part of the full geometry. Moreover, important structures like trabeculae, the denticulate ligament, and nerves present in the SAS have been disregarded. Additionally, all materials are considered isotropic for all their properties, even though this does not hold true for spinal cord permeability. The matrix of the spinal cord is considered linear elastic while scientific literature described the spinal cord as a non-linear viscoelastic. No prestresses, has been taken into account.

8 Conclusion

In summary, this investigation has provided enhanced insights into the implications of an artificial three-dimensional obstruction by employing two distinct FEA techniques: CFD and the poroelastic FSI.

The findings of this study reveal that the introduction of the FSI approach did not notably contribute to enhancing the comprehension CSF flow within the spinal SAS, but does provides additional information concerning fluid exchange and stresses within the spinal cord. Hence, depending on the area of interest, these findings might facilitate the selection of the most suitable approach for subsequent simulations.

Moreover, particularly the substantial obstruction appears to alter the spinal cord's deformation behaviours and seems to enhance fluid exchange between the spinal SAS and the spinal cord. However, the precise mechanisms driving this relationship remain unclear, warranting further investigation.

Future endeavours could involve incorporating material property anisotropy and accounting for anatomical structures within the SAS. Furthermore, refining the modeling approach for the 100% obstruction of the back portion of the spinal SAS remains an avenue for improvement. Finally, a full 3D model of the SAS can help to underline phenomena difficult to observe in the cropped geometry.

References

(1) Libretexts. (2023, February 3). 8.2: Review of Basic Concepts of the Central Nervous System. MedicineLibreTexts

(2) Scanlon, Valerie ‘’C.,Essentials of anatomy and physiology: Chapter 8: The Nervous System’’ in C.,Essentials of anatomy and physiology, 5th ed Pearson Education, 2007.

(3) Carter, Rita, et al. The Human Brain Book. 1st American ed. London [England], New York, N.Y., 2009

(4) Ghannam JY, Al Kharazi KA. Neuroanatomy, Cranial Meninges. [Updated 2022 Jul 25]. In: StatPearls [Internet]. Treasure Island (FL): StatPearls Publishing; 2022 Jan-. Available from: https://www.ncbi.nlm.nih.gov/books/NBK539882/

(5) Khani M, Sass LR, Sharp MK, McCabe AR, Zitella Verbick LM, Lad SP, Martin BA. In vitro and numerical simulation of blood removal from cerebrospinal fluid: comparison of lumbar drain to Neurapheresis therapy. Fluids Barriers CNS. 2020 Mar 16;17(1):23. doi: 10.1186/s12987-020-00185-5. PMID: 32178689; PMCID: PMC7077023.

(6) Brinker T, Stopa E, Morrison J, Klinge P. A new look at cerebrospinal fluid circulation. Fluids Barriers CNS. 2014;11:10

(7) Bothwell, S.W., Janigro, D. & Patabendige, A. Cerebrospinal fluid dynamics and intracranial pressure elevation in neurological diseases. Fluids Barriers CNS 16, 9 (2019). https://doi.org/10.1186/s12987-019-0129-6

(8) Wichmann Thea Overgaard, Damkier Helle Hasager, Pedersen Michael, A Brief Overview of the Cerebrospinal Fluid System and Its Implications for Brain and Spinal Cord Diseases ,Frontiers in Human Neuroscience,15,2022,DOI=10.3389/fnhum.2021.737217

(9) Mestre H, Tithof J, Du T, Song W, Peng W, Sweeney AM, Olveda G, Thomas JH, Nedergaard M, Kelley DH. Flow of cerebrospinal fluid is driven by arterial pulsations and is reduced in hypertension. Nat Commun. 2018 Nov 19;9(1):4878. doi: 10.1038/s41467-018-07318-3. PMID: 30451853; PMCID: PMC6242982

(10) Kiviniemi, Vesa et al. “Ultra-fast magnetic resonance encephalography of physiological brain activity - Glymphatic pulsation mechanisms?.” Journal of cerebral blood flow and metabolism : official journal of the International Society of Cerebral Blood Flow and Metabolism vol. 36,6 (2016): 1033-45. doi:10.1177/0271678X15622047

(11) W. Kalata, B. A. Martin, J. N. Oshinski, M. Jerosch-Herold, T. J. Royston and F. Loth*, "MR Measurement of Cerebrospinal Fluid Velocity Wave Speed in the Spinal Canal," in IEEE Transactions on Biomedical Engineering, vol. 56, no. 6, pp. 1765-1768, June 2009, doi: 10.1109/TBME.2008.2011647.

(12) Friese, Sigrid et al. “The influence of pulse and respiration on spinal cerebrospinal fluid pulsation.” Investigative radiology vol. 39,2 (2004): 120-30. doi:10.1097/01.rli.0000112089.66448.bd

(13) Chiari Malformation – Symptoms, Diagnosis and Treatments. (n.d.). https://www.aans.org/en/Patients/Neurosurgical-Conditions-and-Treatments/Chiari-Malformation

(14) Chiari Malformations. (n.d.). National Institute of Neurological Disorders and Stroke. https://www.ninds.nih.gov/health-information/disorders/chiari-malformations (15) Kiviniemi, Vesa et al. “Ultra-fast magnetic resonance encephalography of physiological brain activity - Glymphatic pulsation

mechanisms?." Journal of cerebral blood flow and metabolism : official journal of the 85 International Society of Cerebral Blood Flow and Metabolism vol. 36,6 (2016): 1033-45. doi:10.1177/0271678X15622047

(16) S.B. Hiremath, A. Fitsiori, J. Boto, C. Torres, N. Zakhari, J.-L. Dietemann, T.R. Meling and M.I. VargasAmerican Journal of Neuroradiology November 2020, 41 (11) 1975-1981; DOI: https://doi.org/10.3174/ajnr.A6743

(17) Mesin, L.; Ponzio, F.;Carlino, C.F.; Lenge, M.; Noris, A.;Leo, M.C.; Sica, M.; McGreevy, K.; Anghar Fabrik, E.L.; Giordano, F. A Machine Learning Approach to Support Treatment Identification for Chiari I Malformation. Appl. Sci. 2022, 12, 9039. https://doi.org/10.3390/app12189039

(18) Langridge B, Phillips E, Choi D. Chiari Malformation Type 1: A Systematic Review of Natural History and Conservative Management. World Neurosurg. 2017 Aug;104:213-219.

(19) Pascual J, Oterino A, Bercaino J. Headache in type I Chiari malformation. Neurology. 1992;42:1519–21. Friese, Sigrid et al. "The influence of pulse and respiration on spinal cerebrospinal fluid pulsation." Investigative radiology vol. 39,2 (2004): 120-30. doi:10.1097/01.rli.0000112089.66448.bd

(20) N. Aghakhani et al., "Long-term follow-up of chiari-related syringomyelia in adults: Analysis of 157 surgically treated cases," Neurosurgery, vol. 64, no. 2, 2009, doi: 10.1227/01.NEU.0000336768.95044.80

(21) K Sivaramakrishna and K Sathyavaraprasad, "Study on Syringomyelia," International Journal of Contemporary Medical Research , vol. 4, no. 10, pp. 2211–2214, Oct. 2017

(22) Jacobson, E E et al. "Fluid dynamics of the cerebral aqueduct." Pediatric neurosurgery vol. 24,5 (1996): 229-36. doi:10.1159/000121044

(23) Eldaya, R.W., Strahle, J.M., Goyal, M.S. (2020). Advanced Imaging of Chiari I Malformations. In: Tubbs, R., Turgut, M., Oakes, W. (eds) The Chiari Malformations. Springer, Cham. https://doi.org/10.1007/978-3-030-44862-2_28).

(24) Akbar Fakhri, Manish N. Shah, Manu S. Goyal,Advanced Imaging of Chiari 1 Malformations, Neurosurgery Clinics of North America,Volume 26, Issue 4, 2015,Pages 519-526, https://doi.org/10.1016/j.nec.2015.06.012

(25) C. Ramón, A. Gonzáles-Mandly, J. Pascual What differences exist in the appropriate treatment of congenital versus acquired adult Chiari type I malformation? Curr Pain Headache Rep, 15 (2011), pp. 157-163').

(26) Chavez, Alexis et al. "Comparison of operative and non-operative outcomes based on surgical selection criteria for patients with Chiari I malformations." Journal of clinical neuroscience : official journal of the Neurosurgical Society of Australasia vol. 21,12 (2014): 2201-6. doi:10.1016/j.jocn.2014.06.009

(27) Maia Osborne-Grinter, Mohit Arora, Chandrasekaran Kaliaperumal, Pasquale Gallo, Posterior Fossa Decompression and Duraplasty with and without Arachnoid Preservation for the Treatment of Adult Chiari Malformation Type 1: A Systematic Review and Meta-Analysis, World Neurosurgery, Volume 151, 2021, Pages e579-e598, https://doi.org/10.1016/j.wneu.2021.04.082

(28) N. Aghakhani et al., "Long-term follow-up of chiari-related syringomyelia in adults: Analysis of 157 surgically treated cases," Neurosurgery, vol. 64, no. 2, 2009, doi: 10.1227/01.NEU.0000336768.95044.80

(29) Ken Sakushima, Satoshi Tsuboi, Ichiro Yabe, Kazutoshi Hida, Satoshi Terae, Ritei Uehara, Imaharu Nakano, Hidenao Sasaki, Nationwide survey on the epidemiology of syringomyelia in Japan, Journal of the Neurological Sciences, Volume 313, Issues 1–2, 2012, Pages 147-152, https://doi.org/10.1016/j.jns.2011.08.045.]. 86

(30) Choi HY, Jeong JE, Lee JS, et al. A case of Syringomyelia with back and shoulder pain. J Acupunct Res. 2019;36(1):45e49

(31) N.S.J. Elliott, C.D. Bertram, B.A. Martin, A.R. Brodbelt, Syringomyelia: A review of the biomechanics,Journal of Fluids and Structures,Volume 40,2013,Pages 1-24,ISSN 08899746,https://doi.org/10.1016/j.jfluidstructs.2013.01.010

(32) Jacobson, E E et al. “Fluid dynamics of the cerebral aqueduct.” Pediatric neurosurgery vol. 24,5 (1996): 229-36. doi:10.1159/000121044

(33) Heidari Pahlavian S, Bunck AC, Thyagaraj S, Giese D, Loth F, Hedderich DM, Kröger JR, Martin BA. Accuracy of 4D Flow Measurement of Cerebrospinal Fluid Dynamics in the Cervical Spine: An In Vitro Verification Against Numerical Simulation. Ann Biomed Eng. 2016 Nov;44(11):3202-3214. doi: 10.1007/s10439-016-1602-x. Epub 2016 Apr 4. PMID: 27043214; PMCID: PMC5050060

(34) Miller, K. (2019). Biomechanics of the Brain. Springer.

(35) Vandenbulcke, Sarah et al. “Computational fluid dynamics model to predict the dynamical behavior of the cerebrospinal fluid through implementation of physiological boundary conditions.” Frontiers in bioengineering and biotechnology vol. 10 1040517. 22 Nov. 2022, doi:10.3389/fbioe.2022.1040517

(36) Wichmann Thea Overgaard, Damkier Helle Hasager, Pedersen Michael, A Brief Overview of the Cerebrospinal Fluid System and Its Implications for Brain and Spinal Cord Diseases ,Frontiers in Human Neuroscience,15,2022,DOI=10.3389/fnhum.2021.737217

(37) Gupta, S., Soellinger, M., Boesiger, P., Poulikakos, D., and Kurtcuoglu, V. (December 10, 2008). "ThreeDimensional Computational Modeling of Subject-Specific Cerebrospinal Fluid Flow in the Subarachnoid Space." ASME. J Biomech Eng. February 2009; 131(2): 021010. https://doi.org/10.1115/1.3005171

(38) Elizabeth C. Clarke, David F. Fletcher, Marcus A. Stoodley, Lynne E. Bilston, Computational fluid dynamics modelling of cerebrospinal fluid pressure in Chiari malformation and syringomyelia,Journal of Biomechanics, Volume 46, Issue 11, 2013, Pages 1801-1809, ISSN 0021-9290, https://doi.org/10.1016/j.jbiomech.2013.05.013.

(39) Gupta, Sumeet et al. “Cerebrospinal fluid dynamics in the human cranial subarachnoid space: an overlooked mediator of cerebral disease. I. Computational model.” Journal of the Royal Society, Interface vol. 7,49 (2010): 1195-204. doi:10.1098/rsif.2010.003

(40) Sweetman, B., Linninger, A.A. Cerebrospinal Fluid Flow Dynamics in the Central Nervous System. Ann Biomed Eng 39, 484–496 (2011). https://doi.org/10.1007/s10439-010-0141-0

(41) Patrick Fillingham, Swati Rane Levendovszky, Jalal Andre, Carolyn Parsey, Michael Bindschadler, Seth Friedman, Mehmet Kurt, Alberto Aliseda, Michael R. Levitt,Patient-specific computational fluid dynamic simulation of cerebrospinal fluid flow in the intracranial space, Brain Research,Volume 1790,2022,147962, ISSN 0006-8993,https://doi.org/10.1016/j.brainres.2022.147962.]

(42) Benninghaus, A., Balédent, O., Lokossou, A. et al. Enhanced in vitro model of the CSF dynamics. Fluids Barriers CNS 16, 11 (2019). https://doi.org/10.1186/s12987-019-0131-z

(43) Khani, M., Burla, G.K.R., Sass, L.R. et al. Human in silico trials for parametric computational fluid dynamics investigation of cerebrospinal fluid drug delivery: impact of injection location, injection protocol, and physiology. Fluids Barriers CNS 19, 8 (2022). https://doi.org/10.1186/s12987-022-00304-4 87

(44) Khani, M., Sass, L.R., Sharp, M.K. et al. In vitro and numerical simulation of blood removal from cerebrospinal fluid: comparison of lumbar drain to Neurapheresis therapy. Fluids Barriers CNS 17, 23 (2020). https://doi.org/10.1186/s12987-020-00185-5

(45) Martin, Bryn A et al. “Spinal subarachnoid space pressure measurements in an in vitro spinal stenosis model: implications on syringomyelia theories.” Journal of biomechanical engineering vol. 132,11 (2010): 111007. doi:10.1115/1.4000089

(46) Støverud, K H et al. “CSF pressure and velocity in obstructions of the subarachnoid spaces.” The neuroradiology journal vol. 26,2 (2013): 218-26. doi:10.1177/197140091302600213

(47) E. C. Clarke, D. F. Fletcher, M. A. Stoodley, and L. E. Bilston, “Computational fluid dynamics modelling of cerebrospinal fluid pressure in Chiari malformation and syringomyelia,” Journal of Biomechanics, vol. 46, no. 11, 2013, doi: 10.1016/j.jbiomech.2013.05.013.

(48) Støverud K-H, Langtangen HP, Ringstad GA, Eide PK, Mardal K-A (2016) Computational Investigation of Cerebrospinal Fluid Dynamics in the Posterior Cranial Fossa and Cervical Subarachnoid Space in Patients with Chiari I Malformation. PLoS ONE 11(10): e0162938. https://doi.org/10.1371/journal.pone.0162938

(49) Bertram, C D et al. “The origins of syringomyelia: numerical models of fluid/structure interactions in the spinal cord.” Journal of biomechanical engineering vol. 127,7 (2005): 1099-109. doi:10.1115/1.2073607

(50) C. D. Bertram. A numerical investigation of waves propagating in the spinal cord and subarachnoid space in the presence of a syrinx. Journal of Fluids and Structures, 25(7):1189–1205, 2009. ISSN 08899746. doi: 10.1016/j.jfluidstructs.2009.06.008.

(51) C. Nicholson. Diffusion and related transport mechanisms in brain tissue. Reports on Progress in Physics, 64(7):815–884, July 2001. ISSN 0034-4885. doi: 10.1088/0034-4885/64/7/202.

(52) Støverud K-H, Mardal K-A, Haughton V, Langtangen HP. CSF Flow in Chiari I and Syringomyelia from the Perspective of Computational Fluid Dynamics. The Neuroradiology Journal. 2011;24(1):20-23. doi:10.1177/197140091102400106

(53) Bertram, C. D., and Heil, M. (November 4, 2016). "A Poroelastic Fluid/Structure-Interaction Model of Cerebrospinal Fluid Dynamics in the Cord With Syringomyelia and Adjacent Subarachnoid-Space Stenosis." ASME. J Biomech Eng. January 2017; 139(1): 011001. https://doi.org/10.1115/1.4034657

(54) C. D. Bertram, “Evaluation by fluid/structure-interaction spinal-cord simulation of the effects of subarachnoid-space stenosis on an adjacent syrinx,” Journal of Biomechanical Engineering, vol. 132, no. 6, 2010, doi: 10.1115/1.4001165.

(55) K. Shahim, J.-M. Drezet, J.-F. Molinari, R. Sinkus, and S. Momjian. Finite element analysis of normal pressure hydrocephalus: Influence of CSF content and anisotropy in permeability. Applied Bionics and Biomechanics, 7(3):187– 197, 2010

(56) Alireza Karimi, Ahmad Shojaei, Pedram Tehrani, Mechanical properties of the human spinal cord under the compressive loading, Journal of Chemical Neuroanatomy, Volume 86, 2017, Pages 15-18, ISSN 0891-0618, https://doi.org/10.1016/j.jchemneu.2017.07.004

(57) S. Cheng, E. C. Clarke, and L. E. Bilston. Rheological properties of the tissues of the central nervous system: A review. Medical Engineering & Physics, 30 (10):1318{1337, 2008.

(58) Ozawa, H., Matsumoto, T., Ohashi, T., Sato, M., & Kokubun, S. (2004). Mechanical properties and function of the spinal pia mater, Journal of Neurosurgery: Spine, 1(1), 122-127. Retrieved May 4, 2023, from https://doi.org/10.3171/spi.2004.1.1.0122 88

(59) Karen H. Støverud, Martin Alnæs, Hans Petter Langtangen, Victor Haughton & Kent-André Mardal (2016) Poro-elastic modeling of Syringomyelia – a systematic study of the effects of pia mater, central canal, median fissure, white and gray matter on pressure wave propagation and fluid movement within the cervical spinal cord, Computer Methods in Biomechanics and Biomedical Engineering, 19:6, 686-698, DOI: 10.1080/10255842.2015.1058927

(60) Elizabeth C. Clarke, David F. Fletcher, Marcus A. Stoodley, Lynne E. Bilston,Computational fluid dynamics modelling of cerebrospinal fluid pressure in Chiari malformation and syringomyelia,Journal of Biomechanics,Volume 46, Issue 11,2013,Pages 1801-1809,https://doi.org/10.1016/j.jbiomech.2013.05.013.

(61) Pietro Matchovich, '' Study of spinal cord poroelastic behaviours under Chiari Malformation conditions: A computational dynamics study," Ghent, 2021

(62) Vineeta Singh, Roger Cheng, Chapter 5 - Neurovascular physiology and neurocritical care, Editor(s): Steven W. Hetts, Daniel L. Cooke, Handbook of Clinical Neurology, Elsevier, Volume 176, 2021, Pages 71-80, ISSN 0072-9752, https://doi.org/10.1016/B978-0-444-64034-5.00014-6.

(63) Bunck, Alexander C et al. "Magnetic resonance 4D flow characteristics of cerebrospinal fluid at the craniocervical junction and the cervical spinal canal." European radiology vol. 21,8 (2011): 1788-96. doi:10.1007/s00330-011-2105-7

(64) Linge, S., Mardal, K., Haughton, V. & Helgeland, A. Simulating CSF flow dynamics in the normal and the Chiari I subarachnoid space during rest and exertion. Am. J. Neuroradio. 34, 41–45 (2012).

(65) C. A. Silvera Delgado, "Modelling the lymphatic system: Computational model of lymphatic capillariesinterstitium interaction in normal physiological and pathological conditions.," Torino, 201

7 (66) M. A. Biot, "General theory of three-dimensional consolidation," Journal of Applied Physics, vol. 12, no. 2, 1941, doi: 10.1063/1.1712886.

(67) Z. Shi and X. Wang, "Comparison of Darcy's Law, the Brinkman Equation, the Modified N-S Equation and the Pure Diffusion Equation in PEM Fuel Cell Modeling," COMSOL Conference, 2007.

(68) "Porous Media Flow Module User's Guide COMSOL 6.1," 202q. https://doc.comsol.com/5.6/doc/com.comsol.help.porous/PorousMediaFlowModuleUsersGuide.pdf (69) P. Rea, "Chapter 7: Essential anatomy and function of the spinal cord," in Essential Clinical Anatomy of the Nervous System. Elsevier Inc., 2015, ch. 7, pp. 121-131. [Online] Available: https://www.sciencedirect.com/book/9780128020302/essential-clinical-anatomy-of-the-nervous-system